# University of Southampton

Faculty of Physical Sciences and Engineering

Zepler Institute for Photonics and Nanoelectronics

Optoelectronics Research Centre


**Single-Fibre Power-Scaling & Pulsed Phase Characterization and Optimization for Coherent Beam Combination**

by


**Huaiqin Lin**

ORCID ID 0000-0002-9805-4570


Thesis for the degree of Doctor of Philosophy

September 2019

# University of Southampton

## Abstract

Faculty of Physical Sciences and Engineering
Zepler Institute for Photonics and Nanoelectronics
Optoelectronics Research Centre

Thesis for the degree of Doctor of Philosophy

Single-Fibre Power-Scaling & Pulsed Phase Characterization and Optimization for Coherent Beam Combination

by

Huaiqin Lin

Pulsed fibre-based lasers are already proven and widely used in low-energy regimes. In addition, they are increasingly considered for new applications requiring high peak power, high average power, as well as high energy. However, the pulse energy is limited by e.g., optical damage, nonlinearities in a single-fibre laser. A promising approach is coherent beam combination which has been proposed for scaling the average and peak power of ultrafast pulsed lasers using an array of matched fibre amplifiers or a sequence of pulses in an amplifier.

This thesis describes a narrow-linewidth linearly-polarised nanosecond pulse-burst Yb-doped fibre amplifier system built to explore the phase distortions within the pulses in the highly nonlinear regime. The phase distortions are mainly induced by self-phase modulation (SPM) and are further complicated with the emergence of gain-saturation-induced sub-pulse reshaping and variations, when the extracted energy is comparable to, or larger than the saturation energy. Large phase distortion (up to a *B*-integral of 21 rad) was successfully characterized through a single-shot homodyne phase measurement scheme based on a 90° optical hybrid technique, and the phase fluctuations were also analysed. On the basis of this phase diagnosis technique, I developed a method to equalise the inter- and intra-phase differences between pulses and realized a theoretical 90% coherent combination with a *B*-integral of >10 rad. This method is based on fast amplitude and phase electro-optic modulators (EOMs) which are controlled by proportional integral derivative (PID) algorithms.

Furthermore, taking advantage of the merits of multi-core fibre and parabolic-pulse amplification for ultrafast pulse combination, I experimentally demonstrated 90% passive coherent combination of an ultrafast twin-core fibre amplifier at a *B*-integral of 29 rad. In addition to the beam combination, I also advanced the power scaling and high beam quality

operating in terms of a single fibre. The power and efficiency of erbium fibre lasers are limited by a small absorption cross-section and concentration quenching. Firstly, using an in-house fabricated large-core Er-doped Yb-free fibre which is cladding-pumped by 0.98-μm diode lasers, I demonstrated a 656-W record output power from any Er-doped fibre source. Then, via a high-concentration nanoparticle doping technique, a high Er-concentration ($4\times10^{25}$ ions/$m^3$) Yb-free fibre was fabricated. An experimentally achieved laser slope efficiency as high as ~41% confirms that the concentration quenching effect is well suppressed.

Last but not least, a large effective area of the fundamental mode and quasi-single-mode operation is desirable for overcoming nonlinear limits in high power fibre amplifiers and lasers. Here, a bendable non-circular core large mode area Yb-doped fibre has been designed and fabricated to avoid bending distortions and mode degeneracy. The ability of the fibre to mitigate bend induced mode-distortions was also experimentally demonstrated.

# Table of Contents

# Table of Figures

# Research Thesis: Declaration of Authorship

| | |
|---|---|
| Print name: | Huaiqin Lin |
| Title of thesis: | Single-Fibre Power-Scaling & Pulsed Phase Characterization and Optimization for Coherent Beam Combination |

I declare that this thesis and the work presented in it are my own and has been generated by me as the result of my own original research.

I confirm that:

1. This work was done wholly or mainly while in candidature for a research degree at this University;
2. Where any part of this thesis has previously been submitted for a degree or any other qualification at this University or any other institution, this has been clearly stated;
3. Where I have consulted the published work of others, this is always clearly attributed;
4. Where I have quoted from the work of others, the source is always given. With the exception of such quotations, this thesis is entirely my own work;
5. I have acknowledged all main sources of help;
6. Where the thesis is based on work done by myself jointly with others, I have made clear exactly what was done by others and what I have contributed myself;
7. Parts of this work have been published as the journal and conference publications listed in Appendix A.

Signature: Date:

# Acknowledgements

First of all, I would like to express enormous gratitude to my supervisor Prof. Johan Nilsson, for welcoming me into the High Power Fibre Lasers (HPFL) group in 2015. His guidance, motivation and patience continuously gave me freedom to pursuit the research. I would never have been able to complete my thesis without his continuous support, immense knowledge and enthusiasm.

I am also very grateful to my co-supervisor Dr. Jonathan H. V. Price. I am impressed by his rigorous scientific attitude and also greatly benefited from his pertinent ideas and supports. Special thanks go to Dr. Ping Hua, I won't be a member of Optoelectronic Research Centre (ORC) without her helps.

The wonderful HPFL group members enriched my research life here. A special thank you to Dr. Yujun Feng who assisted me to finish the main research tasks and Dr. Yutong Feng for endless discussions and supports. I also thank the other group members: Dr. Harish Achar Vasant, Dr. Meng Betty Zhang, Dr. Junqing Zhao, Dr. Po-Tse Tai, Dr. Pengling Yang, Dr. Zhimeng Huang, Dr. Shankar Pidishety, Dr. Zhichao Wu, Dr. Guozheng Wang, Dr. Nan Zhao, Mr. Sheng Zhu, Mr. Pablo G. Rojas Hernández, Mr. Soonki Hong, and Ms. Dan Cheng. Your companies and supports made my time at ORC enjoyable and exciting.

I want to thank Prof. Jayanta Sahu, Prof. Andy Clarkson, Prof. Radan Slavik, Prof. Periklis Petropoulos, Dr. Bill Brocklesby, Dr. Shaif-ul Alam, Dr. Pranabesh Barua, Dr. Yongmin Jung, Dr. Christophe A. Codemard, Dr. Jaclyn Chan, Dr. Lin Xu, Dr. Li Shen, Dr. Di Lin, Dr. Jing He, Dr. Sijing Liang, Mr. Haonan Ren, Mr. Qiang Fu, Mr. Zhengqi Ren, Mr. Ding Meng who continuously helped and supported me through my education.

I would like to acknowledge ORC and China Scholarship Council for providing me the studentship. I also sincerely appreciate Prof. Johan Nilsson to sponsor me over the last year of my stay.

Last but not least, I sincerely appreciate all the endless love and supports from my parents and my elder brother. As confucius said, while one's parents are alive, one should not travel to distant places. If it is necessary to travel, there should be a definite direction. I now know for sure that where you are, where would be my next direction.

# Abbreviations

| | |
|---|---|
| AOM | Acousto-optic modulator |
| AR | Aspect ratio |
| ASE | Amplified spontaneous emission |
| AWG | Arbitrary waveform generator |
| BL | Beat length |
| CBC | Coherent beam combining |
| CCC | Chirally-coupled core |
| CDPA | Chirped- and divided-pulse amplification |
| CLS | Cladding light stripper |
| CNC | Computer numerical control |
| CPS | Coherent pulse stacking |
| CPSA | Coherent pulse stacking amplification |
| CPA | Chirped-pulse amplification |
| CW | Continuous-wave |
| DC | Direct current |
| DCF | Double-clad fibre |
| DFB | Distributed-feedback |
| DM | Dichroic mirror |
| DOE | Diffractive-optical elements |
| DPA | Divided-pulse amplification |
| EDFL | Erbium-doped fibre laser |
| EOAM | Electro-optic amplitude modulator |
| EOM | Electro-optic modulator |
| EOPM | Electro-Optic Phase Modulator |
| ER | Extinction ratio |
| EYDFL | Er:Yb co-doped fibre laser |
| FM | Fundamental mode |
| FUT | Fibre under test |
| FWHM | Full width at half maximum |
| GPIB | General purpose interface bus |
| GTI | Gires-Tournois interferometer |
| GUI | Graphical user interface |

| | |
|---|---|
| GVD | Group-velocity dispersion |
| HOM | High-order-mode |
| HP | High-power |
| HWP | Half-wave plate |
| K-K | Kramers-Kronig |
| LCF | Leakage channel fibre |
| LMA | Large mode area |
| LP | Low-power |
| LPF | Large-pitch photonic-crystal fibre |
| MCVD | Modified chemical-vapor deposition |
| MFD | Mode field diameter |
| MI | Modulation instability |
| MOPA | Master oscillator power amplifier |
| MTF | Multi-trench fibre |
| NA | Numerical aperture |
| NP | Nanoparticle |
| OPLD | Optical-path-length difference |
| OSA | Optical spectrum analyser |
| PBS | Polarisation beam splitter |
| PD | Photo-darkening |
| PER | Polarisation extinction ratio |
| PID | Proportional integral derivative |
| RIP | Refractive index profile |
| PM | Polarisation-maintaining |
| QD | Quantum-defect |
| QWP | Quarter-wave plate |
| RF | Radio frequency |
| SBS | Stimulated Brillouin scattering |
| SHARC | Semi-guiding high-aspect-ratio core |
| SLM | Spatial light modulator |
| SMSR | Side mode suppression ratio |
| SPM | Self-phase modulation |
| SRS | Stimulated Raman scattering |
| TFB | Taper fibre bundle |
| TMI | Thermal mode instabilities |

| | |
|---|---|
| XPM | Cross-phase modulation |
| YDFA | Yb-doped fibre amplifier |
| YDFL | Yb-doped fibre laser |

# Nomenclature

| | |
|---|---|
| $\alpha$ | Absorption coefficient [Np/m] |
| $\beta_2$ | Group-velocity dispersion parameter [$s^2$/m] |
| $\gamma$ | Effective nonlinear coefficient [1/(W·m)] |
| $n_2$ | Nonlinear-index coefficient [$m^2$/W] |
| $A_{eff}$ | Effective mode area [$\mu m^2$] |
| $v_g$ | Group velocity [m/s] |
| $g$ | Gain coefficient [Np/m] |
| $\lambda$ | Wavelength [μm] |
| $L_{eff}$ | Effective fibre length [m] |
| $L_D$ | Dispersion length [m] |
| $L_{NL}$ | Nonlinear length [m] |
| $\phi_{NL}$ | Nonlinear phase shift [rad] |
| $\omega_0$ | Angular optical frequency [rad] |
| $\sigma_{es}$ | Emission cross-section [$m^2$] |
| $\sigma_{as}$ | Absorption cross-section [$m^2$] |
| $\Gamma_s$ | Signal overlap with an active dopant |
| $v$ | Optical frequency [Hz] |
| $E_{sat}$ | Saturation energy [J] |

# Chapter 1
# Introduction

## 1.1 Motivation

Fibre lasers have achieved extraordinary success in a range of applications both in the defence and commercial arenas. Contributing factors to this success include simple and well controlled manufacturing, excellent reliability, robustness, high efficiency, outstanding power-scalability, and exquisite control over many aspects of the output light beam [1, 2]. While the merits of fibre lasers are well established in the continuous-wave (CW) regime, effects such as nonlinearities, phase distortions, and damage typically diminish the performance of current pulsed single-fibre lasers as well as combined arrays, especially at high pulse energies [3]. The primary motivation of my PhD project has been to develop pulsed fibre systems suitable for coherent combination, and fibres as well as new methods of characterization.

Here, a high-energy narrow-linewidth linearly-polarised pulse-burst Yb-doped fibre amplifier system was established for coherent combining. In the final amplifier, a low-NA large-mode-area (LMA) Yb-doped fibre (Clemson) which was polarisation-maintaining (PM) by virtue of a low birefringence was chosen for achieving a high-energy, linear polarisation, and single-mode output. To investigate the phase distortions, I developed a temporal technique for accurately characterizing nonlinear phases in the fibre amplifier system in the highly nonlinear regime, where phase distortions induced by SPM and even the gain-saturation-induced sub-pulse reshaping and variations require more accurate characterization and control. Typically, the pulses in the chirped-pulse amplification (CPA) system will be stretched to the ns regime, which is comparable to our 1-ns system. Thus, an understanding of phase distortions in the narrow-linewidth ns regime is beneficial to our further exploration in a CPA system. To get an efficient combination, then the pulse-burst inter- and intra-phase are actively controlled and compensated through fast phase and amplitude EOMs together with an optimized algorithm.

Besides, the multi-core fibre is a compact and promising way to realizing ultrafast pulse combination with reduced component count and suppression of common-mode phase perturbations thanks to proximity of the cores. A twin-core double-clad PM Yb-doped fibre was in-house designed and fabricated for coherent combining investigation. This had several distinctive features, notably small cores to facilitate high-nonlinearity investigations. Experimentally I demonstrated that efficient passive combination can be achieved with ultrafast pulses in a twin-core fibre amplifier in the highly nonlinear regime. An improved

understanding will allow us to predict the limits of the next generation fibre source in other regimes such as chirped pulses and broad bandwidth pulses. These effects depend also on the fibre parameters such as mode area as well as on the active dopant and wavelength of operation.

In addition to the beam combining, I also investigated the lasing performance of a non-circular core LMA ytterbium-fibre for suppressing mode bending distortions. Furthermore, my research has also extended to characterize the EDFLs in high-power CW regime and evaluated possible improvements in power and brightness, and potential for pulse amplification.

## 1.2 Thesis outline

The outline of this thesis is laid out as follows:

The primary motivation of my PhD project is given in the introductory Chapter 1.

Chapter 2 firstly reviews the development of power and energy scaling in YDFL systems, especially the progress of techniques utilized in the ultrafast pulse regime, mainly including the chirped-pulse amplification, coherent beam combination, divided pulse amplification and coherent pulse staking. Different phase detection and control techniques applied in ultrafast pulse coherent combining are also described. Last but not least, the basic concept of self-phase modulation is given.

Chapter 3 describes a high-energy narrow-linewidth linearly-polarised pulse-burst Yb-doped fibre amplifier system that I developed, which is employed for subsequent investigations described in Chapter 5 and 6. The characteristics of the seed source and pulse-burst generation, cascaded polarisation-maintaining fibre pre-amplifiers and a low-birefringence low-NA LMA fibre amplifier are all included.

Chapter 4 presents single-shot phase measurements based on homodyne detection with a 90° optical hybrid, to extract the temporal phases of narrow-line pulse-bursts in divided-pulse amplification systems. A nonlinear phase shift as high as 21-rad has been successfully measured and fluctuation analysis of the measurement results is also described.

Chapter 5 reports our investigation on the active control of pulse amplitudes and instantaneous-phases through fast EOMs to compensate the phase distortions, aiming to optimize the coherent combining efficiency when pulses within the burst are temporally stacked. The influence of amplitude difference, *B*-integral difference and input amplitude fluctuation between pulse-burst on the coherent combining efficiency was firstly studied. Based on the calculation results, an optimized inter-pulse amplitude compensation and intra-

pulse instantaneous-phase equalisation was applied and eventually a theoretically combined efficiency of 90% in a 1.15 mJ narrow-linewidth linearly-polarised divided-pulse amplification system with a *B*-integral of 16 rad was achieved.

Chapter 6 focuses on the experimental investigation of a passive coherent beam combination in an ultrafast parabolic-pulse twin-core Yb-doped fibre amplifier in the highly nonlinear regime. Eventually, I demonstrated that an 88.5% coherent combining efficiency can be achieved though the individual amplifier has a *B*-integral of 30.2 rad.

Chapter 7 reports a non-circular elongated-core large-mode-area Yb-doped fibre which is proposed to avoid bending distortions and mode degeneracy. Theoretical investigations and optimized confined doping were carried out in terms of the design and fabrication processes, respectively. Finally, high-power lasing based on a bendable non-circular core LMA fibre was demonstrated.

Chapter 8 presents our experimental investigations on the power scalability of continuous wave EDFLs, using two erbium fibres. In the first case, I built a large-core Er-doped Yb-free fibre laser cladding-pumped by 0.98-μm diode lasers to overcome the current average power limitations in EDFLs. In another case, I established a highly-efficient, high-power 0.98-μm cladding-pumped Er-doped fibre laser, based on a high-concentration Er-nanoparticle-doped Yb-free fibre. The results are analysed and the possibility of a kW-level Yb-free EDFL with high beam quality is also discussed.

Chapter 9 concludes all the work presented throughout this thesis and discusses future prospects.

## 1.3 Contributions and acknowledgements

The author is responsible for all the work presented in this thesis under the supervision of Prof. Johan Nilsson and Dr. Jonathan H. V. Price.

The low-birefringence LMA Yb-doped fibre (DB01216) in Chapter 3 was fabricated at ECE/COMSET, Clemson University by Dr. Thomas W. Hawkins and Prof. Liang Dong.

The twin-core double-clad PM Yb-doped phosphosilicate fibre (A1214-L10596-L10469) in Chapter 6 was fabricated by the Silica Fibre Fabrication Group, University of Southampton by Dr. Pranabesh Barua and Prof. Jayanta Sahu. The Dammann grating was provided by Dr. W. Minster Kunkel and Prof. James R. Leger, University of Minnesota.

Fabrication of the non-circular core large-mode-area Yb-doped fibre and the relevant theoretical calculations and simulations in Chapter 7 were done at Nanyang Technological University by Dr. Junhua Ji, Dr. Raghuraman Sidharthan, Dr. Daryl Ho, Dr. Yanyan Zhou and Asst. Prof. Seongwoo Yoo.

The large-core Er-doped Yb-free fibre (A1028-L10552) in Chapter 8 was fabricated by the Silica Fibre Fabrication Group, University of Southampton by Dr. Pranabesh Barua and Prof. Jayanta Sahu. The Er-nanoparticle-doped Yb-free fibre (NRL170525) in Chapter 8 was fabricated at Naval Research Laboratory and involved Dr. Colin Baker, Dr. E. Joseph Friebele, Dr. Ashley Burdett, Dr. Daniel Rhonehouse, Dr. L. Brandon Shaw and Dr. Jasbinder Sanghera.

The general MATLAB code structure and GUI designs for phase measurement and phase controls were developed with assistance from Dr. Yujun Feng.

## References

[1]. D. J. Richardson, J. Nilsson, and W. A. Clarkson, “High power fiber lasers: current status and future perspectives [Invited]”, J. Opt. Soc. Am. B **27**, B63 (2010).

[2]. M. N. Zervas and C. A. Codemard, “High power fiber lasers: a review”, IEEE J. Sel. Top. Quantum Electron. **20**, 0904123 (2014).

[3]. J. Limpert, F. Röser, T. Schreiber, and A. Tünnermann, “High-power ultrafast fiber laser systems”, IEEE J. Sel. Top. Quantum Electron. **12**, 233 (2006).

# Chapter 2
# Background

In this chapter, the progress made to date toward high-power CW and high-energy ultrafast pulse YDFLs is briefly reviewed. Particularly in ultrafast pulse amplification, typical techniques, e.g., CPA and parabolic-pulse amplification in single-fibre schemes, and ultrafast pulse coherent combining in spatial and temporal domains are highlighted. Then the active and passive phase stabilization, and optical phase detection and control techniques in ultrafast pulse coherent combination are presented. Finally, concept of self-phase modulation that is central to this thesis is also introduced.

## 2.1 Power and energy scaling in YDFL systems

In 1960, T. H. Maiman at Hughes Research Laboratories demonstrated the first laser at 694 nm, which was achieved by pumping a ruby crystal with a high-power flash lamp [1]. In the following year, the first fibre laser was demonstrated by Snitzer, operating at 1.06 μm with neodymium (Nd) dopant ions [2]. At that time, fibres were still very ‘lossy’ and the broadband flash-lamp with side-pumping in a pump cavity led to a low absorption of the pump. The situation lasted for years and only started to change when Keck *et al*. announced their 20 dB/km low-loss fibre breakthrough in 1970 [3]. Two years later, Stone and Burrus demonstrated the first diode laser end-pumped fibre laser, which greatly improved the laser efficiency [4]. In 1985, the interest in fibre lasers was rekindled by the fabrication of low-loss doped fibre which can provide high optical gain for potential applications in optical telecommunication amplifiers [5, 6]. Then in 1987, Payne and co-workers invented the profound erbium-doped fibre amplifier (EDFA) at 1.55 μm [7]. Together with the development of suitable diode lasers for pumping, the fibre fabrication technology invented at the ORC enabled the development of the Internet as we know it today. The same fibre fabrication technology also enabled the rapid development of high-power CW fibre lasers. In addition, this required, and only truly took off after, the invention of double-clad fibre (DCF) [8-10] and the development of high-power multimode diode lasers [11].

In terms of high-power CW operation, YDFLs have progressed furthest. The YDF can have a quantum defect of less than 10% with diode laser pumping at 9xx nm, can provide optical-to-optical efficiencies of over 80%, and, therefore, low thermal load. The large surface-to-active-volume ratio of the fibre helps to extract heat and further enable high average power operation. Besides, the absorption spectrum covers a wavelength range in which powerful diode lasers

are commercially available. Together with its broad gain bandwidth and operational wavelength around 1.06 μm, it has been a preferred gain medium since around the turn of the century. The descriptions of high-power YDFLs have been summarized in several publications [12-14]. There was an exponential-like growth in average output power of nearly diffraction-limited YDFLs from around 1990, for some 20 years. Here, I only point out some ground-breaking and profound results. In 1999, the first single-mode cladding-pumped YDFL with over 100-W of output power was demonstrated [15]. This important demonstration confirmed the advantages of the cladding-pumped fibre architecture in combination with the high-power and high-brightness 9xx-nm diode pump sources. It also revealed the remarkable scalability of DCF for achieving potential higher output power. Shortly thereafter, in 2004, a kilowatt level single-mode large-core cladding-pumped fibre laser was realized [16]. However, this used a free-space cavity, which is unsuitable for commercial kilowatt level fibre laser applications. Instead, researchers developed a compact configuration based on a single high-power fibre oscillator pumped by a taper fibre bundle (TFB) spliced to the end of the YDF [17]. Besides, an oscillator followed by one or more amplifiers, i.e., master oscillator power amplifier (MOPA), [18] were also widely adopted for power scaling. These alignment-free all-fibre laser systems rely on the successful fabrication of high-power fibre Bragg gratings [17, 19], the progress of high-brightness pump diodes [11] and the availability of all-fibre passive components with high-power handling capability [20]. Nowadays, through the TFB pumping scheme, an output power of 5 kW with near diffraction-limited beam quality at 1080 nm central wavelength can be successfully generated [21]. It is noted that tandem pumping [22] is another pumping scheme which uses one or more fibre lasers to pump another one. One of its advantages is that the pump wavelength can be quite close to the emission wavelength, which reduces the quantum defect heating and thus the fibre thermal load. Through tandem pumping, the company IPG has achieved 10-kW of output power at 1070 nm with pumping by 1018-nm YDFLs [23]. Moreover, all-fibre side-pumping with distributed pump coupling is also possible and the most typical representative is SPI Laser’s proprietary GT-Wave technology [24-26]. This technology has attracted great attention and currently 5-kW of output power can be achieved from a GT-Wave fibre amplifier [27]. In general, the power scaling of CW YDFLs has been very successful with the development of active fibre fabrication technologies, high-brightness pump diodes, thermal management and techniques for control of nonlinearities. Meanwhile, to pursue stable high-power output with high beam quality, efforts have expanded to solving issues such as mode degradation/distortions [28-30], transverse modal instabilities (TMI, a nonlinearity that can be thermally driven) [31-33], and photodarkening [34, 35].

YDFL systems are also interesting for high-power ultrafast pulse generation and amplification

due to several properties [12]. Firstly, a broad emission spectrum allows for short pulse amplification. Furthermore, the long fluorescence lifetime (~1 ms) benefits energy storage, although this is still limited due to the small mode-size and high amplified spontaneous emission (ASE). Concentration quenching can also be avoided due to a simple 4f electron configuration with only a single hole, and thus only two energy levels. These ultrafast lasers have pulse durations in the picosecond or femtosecond range, and are used in manufacturing, medicine, sensing and so on. These pulses are very short, thus less or no heating of the base material occurs, which allows them to precisely cut micro-material. Besides, these high-power and high-peak intensity laser beams also have several emerging applications such as particle acceleration, advanced attosecond science, X-ray and γ radiation generation, electron and proton beam generation resulting from laser-matter interactions in the relativistic regime [36].

In terms of power scaling of ultrafast pulses, the challenge is to preserve the output pulse characteristics in the presence of various deleterious effects such as fibre nonlinear effects, chromatic dispersion, thermal beam distortions, optical damage and even self-focusing. Thus, the peak power of the pulses that can be generated will be restricted and in practice, the limits on power and energy scaling are mainly imposed by the peak power rather than energy storage. Nevertheless, great progress toward high-peak-power ultrafast pulsed YDFLs has been achieved. For this, spatial as well as temporal scaling schemes can be used to overcome the impact of the deleterious effects.

### 2.1.1 Large-mode-area fibres

One spatial scaling option is to design special large-mode-area (LMA) fibres, which have enlarged single-transverse mode areas to increase the achievable peak power. LMA Yb-doped fibres have been commonly used in fibre amplifiers and lasers for generation of high power and high energy radiation [37, 38]. Thanks to the large effective area of the fundamental mode (FM), the onset of undesirable nonlinear effects and catastrophic optical damage can be avoided [39]. With the increase of the core size, the output beam is expected to become multi-moded with degraded beam quality. To maintain good beam quality at the output of a large-mode-area fibre that supports several modes, the high-order-modes (HOMs) are suppressed by both experimental techniques and specialty fibre designs. For example, in a conventionally-designed few-moded fibre, HOMs can be filtered out through bending [40] and the FM can be selectively excited at the launch [41]. For both cases, the effective area of the FM is limited to about 1000 $\mu m^2$ since the effective-index difference between the FM and HOMs becomes smaller as the mode area increases. This leads to mode mixing and nullifies the mode-selective bending loss scheme for single mode operation [40]. Various specialty LMA fibre designs are

reported to further extend the maximum core size while preventing unwanted HOMs by mode-selective gain, e.g., through selective doping [42], or mode-differentiated losses, e.g., chirally-coupled core fibres [43], leakage channel fibres (LCFs) [44], large-pitch photonic-crystal fibres (LPFs) [45], and multi-trench fibres (MTFs) [46]. With a LCF, direct amplification of 10 ps pulses with peak power in excess of 1 MW has been demonstrated [47]. Furthermore, to reach higher pulse energy levels in ultrafast MOPA schemes, two pulse amplification approaches have also been proposed for temporal scaling: CPA and parabolic-pulse amplification.

### 2.1.2 Fibre-based CPA and parabolic-pulse amplification

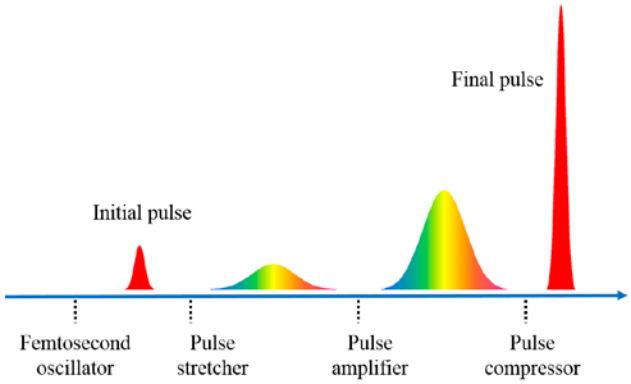


Figure 2.1: Schematic of a typical CPA system.

In 1985, Strickland and Mourou experimentally demonstrated that the CPA technique can be used to generate high-intensity, ultrafast optical pulses for the first time [48]. This ground-breaking invention received the 2018 Nobel Prize in Physics. Fibre-based CPA systems are currently one of the best technical solutions to generate ultrafast pulses at high average power. This CPA approach makes it possible to boost the pulse energies achievable from a simple femtosecond fibre oscillator by more than six orders of magnitude, from the nanojoule to the millijoule regime. A schematic of a CPA system is illustrated in Figure 2.1.

Generally, laser pulses are firstly generated in an optical resonator. Before amplification, a dispersive element introduces a large group delay dispersion to temporally stretch the pulses to a much longer duration (typically up to 1 ns). This also chirps the pulses. Generally, dispersive elements such as a length of dispersive fibre, bulk grating pairs or a chirped fibre Bragg grating are used to stretch the pulses. The extended duration reduces the peak power of the pulses to a low level and allows the pulses to be amplified to saturation while it maintains the peak power at a relatively low level, where SPM and damage problems in the gain medium are avoided. At the output of the amplifier, typically, a bulk grating compressor with opposite dispersion un-chirps the pulses and thus reduces the pulse width and increases the peak power.

As the peak power becomes very high at the compressor, the beam size on the compressor grating has to be large. Through this CPA method, more energy can be extracted without the nonlinearity and damage problems within the amplifier caused by high peak intensities.

With the exploitation and steady improvement of two technologies, CPA and LMA fibres, the average power of ultrafast pulse fibre lasers has reached tremendous performance. In 2010, Eidam *et al*. demonstrated a record 830-W average output power in a single mode femtosecond fibre CPA system [49]. It is noted that further average-power-scaling would be limited by the onset of TMI. Likewise, with regard to the peak power extreme, a record 3.8-GW peak power has been achieved in a femtosecond fibre CPA system that comprises a large pitch fibre with a 105-μm mode field diameter (MFD) with active phase control [50]. According to a numerical study [51], an optimized ultrafast fibre laser with a 10-GW peak power should be achievable. Despite the employment of CPA and LMA fibre designs, which have improved the pulse peak-power by orders of magnitude [49-53], further scaling is now again severely restricted by the same nonlinear effects, i.e., SPM in the first instance. SPM imposes phase fluctuations which lead to a nonlinear frequency chirp across the pulse, which cannot be compensated for by standard dispersive elements, and which thus reduce the recompressed pulse quality and the corresponding peak power. It is worth noting that the SPM-induced phase depends on the stretched pulse shape. For typical $sech^2$ or Gaussian pulse shape, active phase control is needed to control the nonlinear chirp for ensuring the pulse quality in the highly nonlinear regime [50, 54]. It has been experimentally demonstrated that a *B*-integral (a measure of the maximum accumulated nonlinear phase at the pulse centre) as high as 16 rad could be controlled in an Yb-doped fibre-CPA-system [55]. However, a parabolic-pulse seems to be an exception, which has been developed into a technology called high-*B* parabolic-pulse amplification.

Parabolic-pulse amplification can avoid catastrophic pulse break-up induced by excessive SPM in CPA, and has therefore great potential to break the ultrafast pulse peak-power limit [56]. Parabolic-profile pulses, also referred to as self-similar pulses, are solutions to the nonlinear Schrödinger equation (NLSE) with gain and normal dispersion [57]. These self-similar pulses will remain parabolic in profile with a linear chirp across the central region of the pulse, as they are amplified in fibre with normal dispersion [58, 59]. As the pulse is gradually amplified, it will be temporally broadened, thereby spreading the pulse energy over a larger time scale and reducing the pulse peak power. At the output, these linearly chirped pulses can be compressed by an appropriately dispersive element even with significant SPM in the fibre. Through this technique, 1.2-μJ pulse energy has been achieved in a femtosecond fibre source based on an Yb-doped PM PCF [60].

On the whole, with the development of CPA and parabolic-pulse amplification technologies,

the achievable average output power and pulse energy from a single fibre have seen great improvement. Of the two, CPA allows for the highest energy. Still, even for CPA, limitations on pulse energy remain severe for in fibres [53], where recompressed-pulse distortions caused by SPM occur at relatively low pulse energies, in the ~mJ range [61]. Besides, the TMI effect currently limits the average output power of diffraction-limited beam to 1 kW [49]. To scale the energy and power of ultrafast laser sources beyond a single-amplifier technical limitation, the approach of coherently combining the outputs from an array of fibre lasers has been established and developed [62].

### 2.1.3 Development on coherent combining of ultrafast pulses

Coherent beam combination (CBC) involves the amplification of seed beams in separate channels and coherent combination at the output. In this way, the on-axis far-field intensity can increase to $N^2$ times the intensity of a single laser beam and $N$ times the intensity of an incoherently combined laser [62] (this assumes in both cases that the total emitter area scales by $N$). It was firstly demonstrated that CBC of fibre amplifiers is a scalable technique to increase the available power in the CW regime. Then it was extended to the long-pulse regime and has now been adapted to the femtosecond regime, with potential breakthroughs in a vast field that remains largely unexplored. As one important example, enhancement cavities and temporal stacking allow these coherently controlled pulsed systems to achieve combinations of peak and average powers that are difficult or impossible to achieve by conventional laser technology. As another example, while conventional spectral beam combination allows for power-scaling that is at best proportional to the spectral bandwidth, coherent spectral beam combination in the pulsed regime allows the pulse peak power to grow quadratically with the bandwidth.

#### 2.1.3.1 Spatial and temporal coherent combining

Here, approaches for realizing CBC of femtosecond fibre systems and significant results will be described. Basically, the femtosecond pulses in fibre systems can be coherently combined through spatial and temporal coherent combination techniques, as shown in Figure 2.2. These setups typically consist of a femtosecond oscillator, spatial/temporal splitter, amplifiers and a spatial/temporal combiner.

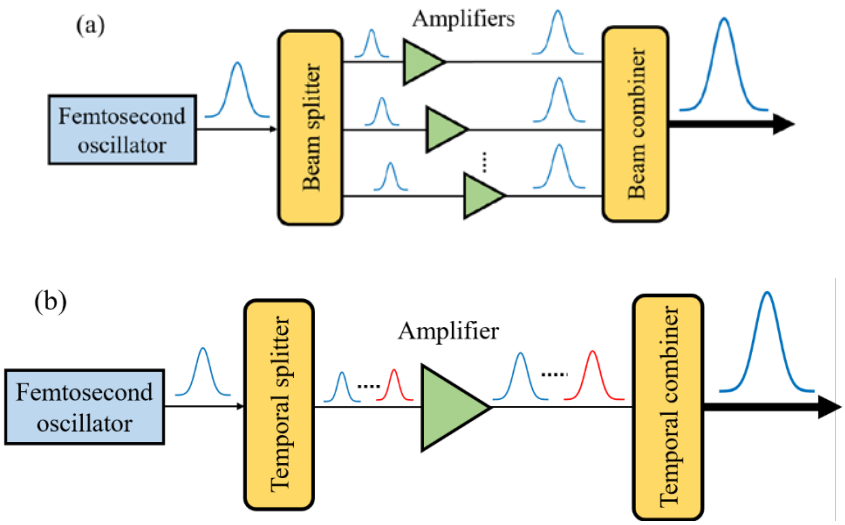


Figure 2.2: Schematic setups of (a) spatial and (b) temporal coherent combining of femtosecond pulses.

Generally, the spatial case can be regarded as an artificial increase of the fibre MFD while a diffraction-limited beam quality will be preserved. The first coherent beam combining of femtosecond amplifiers was experimentally demonstrated in a spatial CBC scheme [63]. In this technique, intensity beam splitter and polarisation beam splitter (PBS) were commonly used to split the beam into different individual fibre amplifiers. Conventional CPA-based independent fibre amplifiers are commonly adopted in these coherent combination systems. Besides, there is another option which transfers independent fibre amplifier channels into a single fibre with a multi-core structure [64]. The large cladding area allows for higher pump power, while the beam quality remains single-mode for each core. Currently, coherent femtosecond pulse combination has been achieved in a fibre with 49 cores [65]. Regarding the coherent combination of spatial CBC, it can be implemented by tiled-aperture and filled-aperture approaches. In the tiled-aperture case, several parallel beams are arranged adjacently to each other in the near field and will be naturally overlapped in the far field to construct a large aperture beam [66]. The advantage of this approach is that no beam combining element is required, which promotes scalability. However, a high combining efficiency is challenging to achieve, because imperfect spatial filling of the tiled beam leads to sidelobes. The filled-aperture is another well-known approach and has been widely applied. For combination, the individual beams are stacked “on top” of each other by optical elements, such as polarisation beam splitters [63], thin-film polarisers [67], diffractive optical elements [68] or others. Theoretically, 100% combining efficiency can be achieved in this approach.

Coherent combination of ultrafast pulses can also be applied in the temporal domain, which was first demonstrated with divided-pulse amplification [69]. Importantly, both temporal and spatial CBC can be used together with CPA, and in some cases also with parabolic-pulse

amplification. Generally, CBC is only considered when CPA on its own is no longer adequate. In divided pulse amplification (DPA), the initial (optionally stretched) single laser pulse is temporally divided into a sequence of pulses with an equal optical delay, and then these pulses are amplified and finally recombined into a high intensity single pulse. This scheme is analogous to having a significantly increased effective pulse duration during the amplification. DPA of femtosecond pulses was initially implemented in a passive configuration based on Mach–Zehnder interferometers, without phase stabilization [70]. However, when aiming for high energy extraction efficiency from the amplifier, gain saturation can lead to amplitude deformation of the pulse burst. This amplitude deformation can by itself reduce the combining efficiency and also lead to differences in nonlinear phase between pulses, which further degrades the efficiency. Thus, actively controlled DPA based on the Locking of Optical Coherence by Single-detector Electronic-frequency Tagging (LOCSET) technique was proposed to compensate the pulse distortions due to saturation, and to finally achieve pulses with an energy of 1.25 mJ and a peak power of 2.9 GW [71]. Afterwards, to allow the compensation of gain saturation and nonlinear phase mismatch within the burst, an improved electro-optically controlled DPA was demonstrated [72].

Recently, another temporal approach called coherent pulse stack amplification (CPSA) was proposed and has been widely investigated [73]. It also employs DPA but uses a Gires-Tournois interferometer (GTI) resonant low-Q cavity to stack a train of pulses into a high intensity pulse. Through CPSA, a 5.4-mJ ultrafast pulse has been achieved from an Yb-doped 85-μm chirally-coupled core (CCC) fibre [74]. Similarly, coherent pulse stacking was realized in a passive high-Q enhancement cavity with an active pulse dumping element [75].

Thus, impressive results have been achieved with both spatial and temporal combination techniques. Motivated by the advantages of these two techniques, a multidimensional amplification architecture has been proposed to explore the potential for further performance-scaling [76]. Through parallel amplification in eight amplifier channels and four temporal pulse replicas, an ultrafast pulse with 12-mJ pulse energy and 700-W average power has been successfully demonstrated [77].

These and other excellent achievements have developed the research on ultrafast pulse coherent combination. It has also inspired further research. The main challenge for all spatial and temporal concepts is the efficient combination of the different pulses into a single intense pulse after amplification, where phase and temporal overlap mismatches degrade efficiency. In practice, however, phase differences (temporal/spectral and spatial) are inevitable, especially when amplifiers are operating in the highly nonlinear regimes. These phase differences can arise from temporal and spectral effects such as SPM, dispersion and optical

path-length difference (OPLD) between the pulses [78, 79]. Therefore, the detection and accurate control of relative phase between channels is crucial for efficient CBC. Especially in the pulsed regime, nonlinear phase distortions have been the subject of considerable attention, and call for more accurate and sophisticated phase control. Nonlinear phase distortions caused by SPM, Kramers-Kronig (K-K) effect, quantum-defect (QD) induced heating and photo-darkening (PD) induced heating, occur within the pulse and strongly affect the pulse behaviour. Their influence on ultrafast pulse coherent combination have been theoretically investigated [80-83]. The experimental implementations of phase stabilization in ultrafast pulse coherent combining can be separated into two categories: active and passive coherent combining.

#### 2.1.3.2 Active and passive coherent combining

Active coherent combining systems rely on an active phase stabilization, which comprises a phase detection scheme, feedback electronics, and a phase-controlling element in each amplifying arm. Normally, phase differences between the individual beams are measured directly or indirectly, and corrected by phase actuators according to a suitable algorithm in a feedback loop. To date, a variety of active phase stabilization methods have been developed for ultrafast pulse coherent combination and applied to a range of configurations. For instance, Hänsch-Couillaud detection can be used together with a piezo stage to match the OPLD and achieve polarisation combination [63]. Other techniques such as active electronic phase locking and so-called LOCSET are widely implemented to correct the relative phase difference with electro-optic phase modulators (EOPMs) [84, 85]. Furthermore, a multiphoton-intrapulse-interference-phase-scan (MIIPS) technique has also been employed to actively shape the spectral phase based on a spatial light modulator (SLM). In this way, a record pulse peak power of 22 GW in a coherently combined femtosecond fibre CPA system was achieved [86]. Recently, with a LOCSET technique, a highest average output power of 3.5 kW from four coherently combined femtosecond fibre amplifiers was demonstrated [87].

In terms of passive coherent combining, its principle of operation is shown in Figure 2.3. The input beam is divided into halves and travel through the same overall optical path, but go through the elements in different order, resulting in passive automatic cancelation of the path fluctuations. Both beams undergo the same level of amplification and interfere constructively at the output due to the same accumulated phase. Therefore, no phase detection or active feedback mechanism is used for accomplishing the combination of the independent amplifiers, in other words, the phase stabilization is an inherent characteristic [88]. The Sagnac interferometer type would be the simplest configuration to realize a passive coherent combining. The schematic of such a system is shown in Figure 2.3 (a).

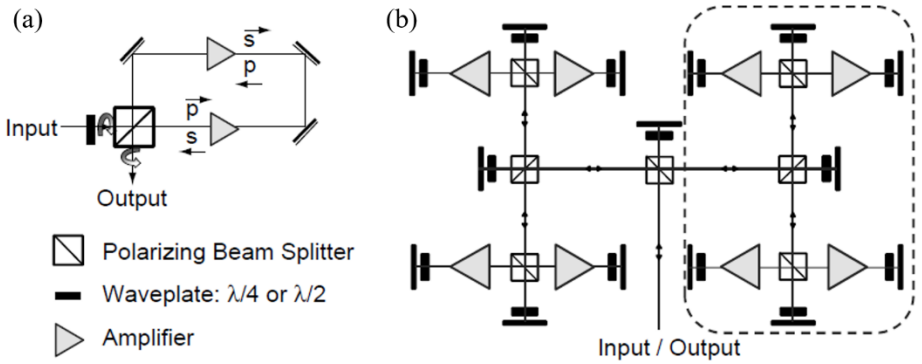


Figure 2.3: The passive coherent combination concept for two (a) and N (b) multi-pass amplifiers (reproduced from Ref. [88]).

So far, the idea of passive coherent combining has been confirmed by only two experiments which both consist of two independent femtosecond fibre amplifiers. In 2011, Daniault *et al*. demonstrated the first passive coherent combining of two femtosecond LMA fibre CPAs using a Sagnac interferometer [89]. A combining efficiency of up to 96% was achieved with a pulse duration of 250 fs at 10-W output power level. It provided the first proof of the applicability of the passive combination architecture with a relatively high nonlinearities (*B*-integral 15-rad). Afterward, the high-power, high-energy potential of this technique has been demonstrated in a similar passive combining architecture with rod-type fibre amplifiers [90]. High temporal quality 300-fs pulses with 650-μJ of pulse energy was generated at 92-kHz repetition rate. This corresponds to an average power of 60 W and a peak power in excess of 2 GW, Furthermore, at higher repetition rate of 2 MHz, a passively combined average power of 135 W and a compressed average power 105 W have been obtained.

## 2.2 Ultrafast pulse phasing techniques

As introduced in Section 2.1.2, to characterize and compensate phase distortions in coherently combined ultrafast systems, a number of phase detection and control techniques have been developed. The rapid progresses on the scaling of power and energy in the ultrafast pulse coherent combination architectures have been driven by these constantly emerging phasing techniques. In this section, phasing techniques applicable to ultrafast pulses are described

Interferometric phase measurement is one approach to characterize the phase. One option is to use a self-referenced quadriwave shearing interferometer and active control with arrays of electro-optic ceramic modulators [91]. In the interferometer, the generated complex segmented wavefront, which stems from the juxtaposition of the quasi-plane sub-wavefronts from each fibre, will be analysed and used to provide feedback signals to the modulators. This approach can actively control the individual phase of each fibre channel without an external

reference. It is well suited for CBC of a very large number of fibre amplifiers. In a tiled-aperture scheme, CBC of 19 fibres in the femtosecond regime with this phasing approach has been successfully demonstrated [64].

In terms of the spectral phasing, one typical representative is the LOCSET approach [92]. In this technique, a sinusoidal phase dither is applied to one channel of the interferometer via the respective piezo-driven mirror, creating an intensity dither at the interferometer output. The intensity dither is detected by a photodiode, and its electric signal is demodulated with the initial sinusoid yielding an asymmetric error signal with zero crossings at the interference extrema of the carrier wave. This error signal is used for a feedback loop acting upon the piezo-driven mirror in that particular channel. Several interferometer channels are addressed by choosing distinct modulation frequencies. The frequencies are chosen to be below the resonance frequency of the piezo mirrors (~10 kHz), but still sufficiently separated to avoid crosstalk and high enough to cover most phase fluctuations.

The MIIPS technique [93] combined with an active spectral phase-shaping system based on a SLM is another possible choice, which can be used to compensate for any residual spectral phase, including accumulated nonlinear phase induced by SPM [86]. Other approaches such as fibre-coupled $LiNbO_3$ integrated phase modulator based on a single frequency dithering technique has also been used to actively control the phase [94]. In CPS, the differences in phase profile induced by saturation during amplification can be corrected by imprinting correct phase profiles on initial pulses through amplitude and phase modulators [73].

## 2.3 Self-phase modulation

In optical fibres, self-phase modulation is one of the lowest-order nonlinear effects that originate from nonlinear refraction, a phenomenon referring to the intensity dependence of the refractive index. SPM refers to the self-induced phase shift experienced by an optical field during its propagation, and is responsible for spectral broadening of optical pulses in optical fibres. For pulses with width over 5 ps, the effects of third-order dispersion, self-steepening and shock formation, and self-frequency shift are negligible. Then, SPM in optical fibres is described by numerical solutions of a simplified pulse-propagation equation, given by

$$i\frac{\partial A}{\partial z}+\frac{i\alpha}{2}A-\frac{\beta_2}{2}\frac{\partial^2 A}{\partial T^2}+\gamma|A|^2A=0, \tag{2.1}$$

where $A$ is the normalized slowly varying amplitude of the pulse envelope, $|A|^2$ represents the optical power, $\alpha$ is the absorption coefficient, $\beta_2$ is the group velocity dispersion (GVD)

parameter, $T$ is measured in a frame of reference moving with the pulse at the group velocity $v_g$ ($T = t - z/v_g$), and the effective nonlinear coefficient $\gamma$ is defined as

$$\gamma = \frac{n_2 \omega_0}{c A_{eff}}, \tag{2.2}$$

where $\omega_0$ is the centre angular frequency of the optical field, $n_2$ is the nonlinear-index coefficient, the parameter $A_{eff}$ is known as the effective mode area and is defined as

$$A_{eff} = \frac{\left(\iint_{-\infty}^{\infty} |E(x,y)|^2 dxdy\right)^2}{\iint_{-\infty}^{\infty} |E(x,y)|^4 dxdy}, \tag{2.3}$$

where $E(x,y)$ is the modal distribution. If the effect of GVD on SPM is negligible, namely if the dispersion length $L_D$ is much larger than the nonlinear length $L_{NL}$, the GVD parameter $\beta_2$ can be set to be zero, then a further simplified equation is given by

$$i\frac{\partial A}{\partial z} + \frac{i\alpha}{2}A + \gamma |A|^2 A = 0. \tag{2.4}$$

Then a time scale normalized to the input pulse width $T_0$ is introduced as

$$\tau = \frac{T}{T_0} = \frac{t - z/v_g}{T_0} \tag{2.5}$$

At the same time, a normalized amplitude $U$ is also introduced as

$$A(z,\tau) = \sqrt{P_0} exp\left[-\frac{\alpha z}{2}\right] U(z,\tau), \tag{2.6}$$

where $P_0$ is the peak power of the incident pulse. By using Equations (2.4) – (2.6), $U(z,\tau)$ becomes

$$\frac{\partial U}{\partial z} = i\gamma |U|^2 U. \tag{2.7}$$

The general solution of Equation (2.7) is

$$U(L,\tau) = U(0,\tau) exp[i\phi_{NL}(L,\tau)], \tag{2.8}$$

where $L$ is the fibre length and nonlinear phase shift is described as

$$\phi_{NL}(L,\tau) = |U(0,\tau)|^2 \, L_{eff}/L_{NL}. \tag{2.9}$$

If the gain per unit length is constant, $L_{eff} = [1 - exp(-gL)]/g$ is the fibre effective length, and $g$ [Np/m] is the gain coefficient of the amplifier.

Equation (2.8) shows that the phase shift induced by SPM is intensity-dependent, while the pulse profile remains unaffected when GVD is negligible. A parameter to estimate the maximum accumulated nonlinear phase $\phi_{max}(z)$ at the pulse centre, called *B*-integral, is defined as

$$B = \int_0^L \phi_{max}\,(z)dz = \int_0^L \gamma P_0(z)\,dz, \tag{2.10}$$

where $P_0(z)$ is the propagation-dependent peak power. In a fibre amplifier, the *B*-integral can be written as

$$B = \frac{2\pi n_2}{\lambda A_{eff}} P_0 L_{eff}, \tag{2.11}$$

where $\lambda$ is the signal wavelength, $A_{eff}$ is the fibre effective mode area.

The time-dependent phase change caused by SPM leads to the creation of new frequency components, which results in spectral broadening of the laser pulses. The temporally varying phase will induce different instantaneous optical frequencies $\partial\phi_{NL}/\partial t$ across the pulse from its central value, $\omega_0$. This time dependent instantaneous optical frequency change is given by:

$$\delta\omega(T) = -\frac{\partial\phi_{NL}}{\partial T} = -(\frac{L_{eff}}{L_{NL}})\frac{\partial}{\partial T}|U(0,\tau)|^2. \tag{2.12}$$

It can be seen from Equation (2.12) that the output spectrum will be continuously broadened as the pulse propagates in the fibre.

One important consequence is that the phase imposed by SPM can lead to a nonlinear chirp, which cannot be compensated by standard dispersive elements. These nonlinear chirps play an important role in the efficient extraction of the stored energy out of the amplifier in CPA and CPSA systems, which makes our investigations necessary and meaningful.

## References


[1]. T. H. Maiman, “Stimulated Optical Radiation in Ruby”, Nature **187**, 493 (1960).

[2]. E. Snitzer, “Optical maser action of $Nd^{3+}$ in a barium crown glass”, Phys. Rev. Lett. **7**, 444 (1961).

[3]. F. P. Kapron, D. Keck, and R. D. Maurer, “Bending losses in single-mode fibers”, in IEE Conference on Trunk Telecommunication by Guided Waves, London, 1970.

[4]. J. Stone and C. A. Burrus, “Neodymium-doped silica lasers in end-pumped fiber geometry”, Appl. Phys. Lett. **23**, 388 (1973).

[5]. S. B. Poole, D. N. Payne, and M. E. Fermann, “Fabrication of low loss optical fibres containing rare-earth ions”, Electron. Lett. **21**, 737 (1985).

[6]. R. J. Mears, L. Reekie, S. B. Poole, and D. N. Payne, “Neodymium-doped silica single-mode fibre laser”, Electron. Lett. **21**, 738 (1985).

[7]. R. J. Mears, L. Reekie, M. Jauncey, and D. N. Payne, “Low-noise erbium-doped fiber amplifier operating at 1.54 μm”, Electron. Lett. **26**, 1026 (1987).

[8]. R. D. Maurer, “Optical waveguide light source”, U.S. patent 3,808,549 (30 April 1974).

[9]. J. D. Kafka, “Laser diode pumped fiber laser with pump cavity”, U.S. patent 4,829,529 (5 September 1989).

[10]. E. Snitzer, H. Po, F. Hakimi, R. Tumminelli, and B. C. McCollum, “Double clad, offset core Nd fiber laser”, in Optical Fiber Sensors (Optical Society of America, 1988), paper PD5.

[11]. M. L. Osowski, W. Hu, R. M. Lammert, S. W. Oh, P. T. Rudy, T. Stakelon, and J. E. Ungar, “Advances in high-brightness semiconductor lasers”, in Laser Source Technology for Defense and Security IV 2008, paper 68761E.

[12]. D. J. Richardson, J. Nilsson, and W. A. Clarkson, “High power fiber lasers: current status and future perspectives [Invited]”, J. Opt. Soc. Am. B **27**, B63 (2010).

[13]. C. Jauregui, J. Limpert, and A. Tünnermann, “High-power fibre lasers”, Nat. Photonics **7**, 861 (2013).

[14]. M. N. Zervas and C. A. Codemard, “High power fiber lasers: a review”, IEEE J. Sel. Top. Quantum Electron. **20**, 0904123 (2014).

[15]. V. Dominic, S. MacCormak, R. Waarts, S. Sanders, S. Bicknese, R. Dohle, E. Wolak, P. S. Yeh, and E. Zucher, “110 W Fiber Laser”, in Conference on Lasers and Electro-Optics (Optical Society of America, 1999), paper CPD-11.

[16]. Y. Jeong, J. K. Sahu, D. N. Payne, and J. Nilsson, “Ytterbium-doped large-core fiber laser with 1.36 kW continuous-wave output power”, Opt. Express **12**, 6088 (2004).

[17]. Y. Xiao, F. Brunet, M. Kanskar, M. Faucher, A. Wetter, and N. Holehouse, “1-kilowatt CW all-fiber laser oscillator pumped with wavelength-beam-combined diode stacks”, Opt. Express **20**, 3296 (2012).

[18]. Y. Fan, B. He, J. Zhou, J. Zheng, H. Liu, Y. Wei, J. Dong, and Q. Lou, “Thermal effects in kilowatt all-fiber MOPA”, Opt. Express **19**, 15162 (2011).

[19]. T. Erdogan, “Fiber grating spectra”, J. Lightwave Technol. **15**, 1277 (1997).

[20]. A. Wetter, M. Faucher, M. Lovelady, and F. Seguin, “Tapered fused-bundle splitter capable of 1KW CW operation”, in Proceedings of SPIE 6453, Fiber Lasers IV: Technology, Systems, and Applications 2007, paper 64530I.

[21]. Q. Fang, J. H. Li, W. Shi, Y. G. Qin, Y. Xu, X. J. Meng, R. A. Norwood, and N. Peyghambarian, “5kW Near-diffraction-limited and 8kW High-brightness Monolithic Continuous Wave Fiber Lasers Directly Pumped by Laser Diodes”, IEEE Photonics J. **9**, 1506107 (2017).

[22]. H. Zimer, M. Kozak, A. Liem, F. Flohrer, F. Doerfel, P. Riedel, S. Linke, R. Horley, F. Ghiringhelli, S. Desmoulins, M. Zervas, J. Kirchhof, S. Unger, S. Jetschke, T. Peschel, and T. Schreiber, “Fibers and fiber-optic components for high power fiber lasers”, in Proceedings of SPIE 7914, Fiber Lasers VIII: Technology, Systems, and Applications 2011, paper 791414.

[23]. E. Stiles, “New developments in IPG fiber laser technology”, in Proceedings of the 5th International Workshop on Fiber Lasers 2009.

[24]. J. Nilsson, J. K. Sahu, J. N. Jang, R. Selvas, D. C. Hanna, and A. B. Grudinin, “Cladding-pumped Raman fiber amplifier”, in Optical Amplifiers and Their Applications (Optical Society of America, 2002), paper PD2.

[25]. A. B. Grudinin, P. W. Turner, M. Ibsen, M. K. Durkin, J. Nilsson, D. N. Payne, and M. N. Zervas, “Multi-fibre arrangements for high-power fibre lasers and amplifiers”, U.S. patent 6,826,335 (30 November 2004).

[26]. V. Gapontsev, D. Gapontsev, N. Platonov, O. Shkurikhin, V. Fomin, A. Mashkin, M. Abramov, and S. Ferin, “2 kW CW ytterbium fiber laser with record diffraction-limited brightness”, in Proceedings of IEEE Conference on Lasers and Electro-Optics Europe (Academic, Europe, 2005), paper 508.

[27]. H. Zhan, Q. Liu, Y. Wang, W. Ke, L. Ni, X. Wang, K. Peng, C. Gao, Y. Li, H. Lin, J. Wang, F. Jing, and A. Lin, “5kW GTWave fiber amplifier directly pumped by commercial 976nm laser diodes”, Opt. Express **24**, 27087 (2016).

[28]. J. M. Fini, “Bend-resistant design of conventional and microstructure fibers with very large mode area”, Opt. Express **14**, 69 (2006).

[29]. J. M. Fini, “Intuitive modeling of bend distortion in large-mode-area fibers”, Opt. Lett. **32**, 1632 (2007).

[30]. J. Fini and J. Nicholson, “Bend compensated large-mode-area fibers: achieving robust single-modedness with transformation optics”, Opt. Express **21**, 19173 (2013).

[31]. T. Eidam, C. Wirth, C. Jauregui, F. Stutzki, F. Jansen, H. J. Otto, O. Schmidt, T. Schreiber, J. Limpert, and A. Tünnermann, “Experimental observations of the threshold-like onset of

mode instabilities in high power fibre amplifiers", Opt. Express **19**, 13218 (2011).

[32]. B. Ward, C. Robin, and I. Dajani, "Origin of thermal modal instabilities in large mode area fiber amplifiers", Opt. Express **20**, 11407 (2012).

[33]. F. Beier, C. Hupel, S. Kuhn, S. Hein, J. Nold, F. Proske, B. Sattler, A. Liem, C. Jauregui, J. Limpert, N. Haarlammert, T. Schreiber, R. Eberhardt, and A. Tünnermann, "Single mode 4.3 kW output power from a diode-pumped Yb-doped fiber amplifier", Opt. Express **25**, 14892 (2017).

[34]. J. J. Koponen, M. J. Söderlund, H. J. Hoffman, and S. K. T. Tammela, "Measuring photodarkening from single-mode ytterbium doped silica fibers", Opt. Express **14**, 11539 (2006).

[35]. M. Engholm, P. Jelger, F. Laurell, and L. Norin, "Improved photodarkening resistivity in ytterbium-doped fiber lasers by cerium codoping", Opt. Lett. **34**, 1285 (2009).

[36]. G. A. Mourou, T. Tajima, and S. V. Bulanov, "Optics in the relativistic regime", Rev. Mod. Phys. **78**, 309 (2006).

[37]. Y. Jeong, J. K. Sahu, D. N. Payne, and J. Nilsson, "Ytterbium-doped large-core fiber laser with 1.36 kW continuous-wave output power", Opt. Express **12**, 6088 (2004).

[38]. F. Stutzki, F. Jansen, A. Liem, C. Jauregui, J. Limpert, and A. Tünnermann, "26 mJ, 130 W Q-switched fiber-laser system with near-diffraction-limited beam quality", Opt. Lett. **37**, 1073 (2012).

[39]. J. W. Dawson, M. J. Messerly, R. J. Beach, M. Y. Shverdin, E. A. Stappaerts, A. K. Sridharan, P. H. Pax, J. E. Heebner, C. W. Siders, and C. P. J. Barty, "Analysis of the scalability of diffraction-limited fiber lasers and amplifiers to high average power", Opt. Express **16**, 13240 (2008).

[40]. J. P. Koplow, D. A. Kliner, and L. Goldberg, "Single-mode operation of a coiled multimode fiber amplifier", Opt. Lett. **25**, 442 (2000).

[41]. M. E. Fermann, "Single-mode excitation of multimode fibers with ultrashort pulses", Opt. Lett. **23**, 52 (1998).

[42]. J. R. Marciante, "Gain filtering for single-spatial-mode operation of large-mode-area fiber amplifiers", IEEE J. Sel. Top. Quantum Electron. **15**, 30 (2009).

[43]. C. Liu, G. Chang, N. Litchinitser, A. Galvanauskas, D. Guertin, N. Jacobson, and K. Tankala, "Effective single-mode chirally-coupled core fiber", in Advanced Solid-State Photonics (Optical Society of America, 2007), paper ME2.

[44]. L. Dong, T. W. Wu, H. A. McKay, L. Fu, J. Li, and H. G. Winful, "All-glass large-core leakage channel fibers", IEEE J. Sel. Top. Quantum Electron. **15**, 47 (2009).

[45]. J. Limpert, F. Stutzki, F. Jansen, H. J. Otto, T. Eidam, C. Jauregui, and A. Tünnermann, "Yb-doped large-pitch fibers: effective single-mode operation based on higher-order mode delocalization", Light: Sci. & App. **1**, 1 (2012).

[46]. D. Jain, C. Baskiotis, and J. K. Sahu, "Mode area scaling with multi-trench rod-type fibers",

Opt. Express **21**, 1448 (2013).

[47]. L. Dong, H. A. McKay, L. B. Fu, M. Ohta, A. Marcinkevicius, S. Suzuki, and M. E. Fermann, "Ytterbium-doped all glass leakage channel fibers with highly fluorine-doped silica pump cladding", Opt. Express **17**, 8962 (2009).

[48]. D. Strickland and G. Mourou, "Compression of amplified chirped optical pulses", Opt. Commun. **55**, 447 (1985).

[49]. T. Eidam, S. Hanf, E. Seisse, T. V. Andersen, T. Gabler, C. Wirth, T. Schreiber, J. Limpert, and A. Tünnermann, "Femtosecond fiber CPA system emitting 830 W average output power", Opt. Lett. **35**, 94 (2010).

[50]. T. Eidam, J. Rothhardt, F. Stutzki, F. Jansen, S. Hädrich, H. Carstens, C. Jauregui, J. Limpert, and A. Tünnermann, "Fiber chirped-pulse amplification system emitting 3.8 GW peak power", Opt. Express **19**, 255 (2011).

[51]. D. N. Schimpf, J. Limpert, and A. Tünnermann, "Optimization of high performance ultrafast fiber laser systems to >10 GW peak power", J. Opt. Soc. Amer. B, **27**, 2051 (2010).

[52]. F. Röser, T. Eidam, J. Rothhardt, O. Schmidt, D. N. Schimpf, J. Limpert, and A. Tünnermann, "Millijoule pulse energy high repetition rate femtosecond fiber chirped-pulse amplification system", Opt. Lett. **32**, 3495 (2007).

[53]. J. Limpert, F. Röser, D. N. Schimpf, E. Seisse, T. Eidam, S. Hädrich, L. Rothhardt, C. Jauregui Misas, and A. Tünnermann, "High repetition rate gigawatt peak power fiber laser-systems: Challenges, design, and experiment", IEEE J. Sel. Top. Quantum Electron. **15**, 159 (2009).

[54]. F. He, H. S. S. Hung, J. H. V. Price, N. K. Daga, N. Naz, J. Prawiharjo, D. C. Hanna, D. P. Shepherd, D. J. Richardson, J.W. Dawson, C.W. Siders, and C. P. Barty, "High energy femtosecond fiber chirped pulse amplification system with adaptive phase control", Opt. Express **16**, 5813 (2008).

[55]. D. N. Schimpf, J. Limpert, and A. Tünnermann, "Controlling the influence of SPM in fiber-based chirped-pulse amplification systems by using an actively shaped parabolic spectrum", Opt. Express **15**, 16945 (2007).

[56]. D. Anderson, M. Desaix, M. Karlson, M. Lisak, and M. L. Quiroga-Teixeiro, "Wave-breaking-free pulses in nonlinear optical fibers", J. Opt. Soc. Am. B **10**, 1185 (1993).

[57]. M. E. Fermann, V. I. Kruglov, B. C. Thomsen, J. M. Dudley, and J. D. Harvey, "Self-Similar Propagation and Amplification of Parabolic Pulses in Optical Fibers", Phys. Rev. Lett. **84**, 6010 (2000).

[58]. V. I. Kruglov, A. C. Peacock, J. M. Dudley, and J. D. Harvey, "Self-similar propagation of high-power parabolic pulses in optical fiber amplifiers", Opt. Lett. **25**, 1753 (2000).

[59]. J. M. Dudley, C. Finot, D. J. Richardson, and G. Millot, "Self-similarity in ultrafast nonlinear optics", Nat. Phys. **3**, 597 (2007).

[60]. T. Schreiber, C. K. Nielsen, B. Ortac, and J. Limpert, "Microjoule-level all-polarization-

maintaining femtosecond fiber source", Opt. Lett. **31**, 574 (2006).

[61]. T. Schreiber, D. Schimpf, D. Müller, F. Röser, J. Limpert, and A. Tünnermann, "Influence of pulse shape in self-phase-modulation-limited chirped pulse fiber amplifier systems", J. Opt. Soc. Am. B **24**, 1809 (2007).

[62]. T. Y. Fan, "Laser beam combining for high-power, high-radiance sources", IEEE J. Sel. Top. Quantum Electron. **11**, 567 (2005).

[63]. E. Seise, A. Klenke, J. Limpert, and A. Tünnerman, "Coherent addition of fiber-amplified ultrashort laser pulses", Opt. Express **18**, 27827 (2010).

[64]. I. Hartl, A. Marcinkevičius, H. A. McKay, L. Dong, and M. E. Fermann, "Coherent beam combination using multi-core leakage-channel fibers", in Advanced Solid-State Photonics (Optical Society of America, 2009), paper TuA6.

[65]. J. Lhermite, E. Suran, V. Kermene, F. Louradour, A. Desfarges-Berthelemot, and A. Barthélémy, "Coherent combining of 49 laser beams from a multiple core optical fiber by a spatial light modulator", Opt. Express **18**, 4783 (2010).

[66]. J. Le Dortz, A. Heilmann, M. Antier, J. Bourderionnet, C. Larat, I. Fsaifes, L. Daniault, S. Bellanger, C. Simon Boisson, J.-C. Chanteloup, E. Lallier, and A. Brignon, "Highly scalable femtosecond coherent beam combining demonstrated with 19 fibers", Opt. Lett. **42**, 1887 (2017).

[67]. A. Klenke, S. Breitkopf, M. Kienel, T. Gottschall, T. Eidam, S. Hädrich, J. Rothhardt, J. Limpert, and A. Tünnermann, "530 W, 1.3 mJ, four-channel coherently combined femtosecond fiber chirped-pulse amplification system", Opt. Lett. **38**, 2283 (2013).

[68]. T. Zhou, T. Sano, and R. Wilcox, "Coherent combination of ultrashort pulse beams using two diffractive optics", Opt. Lett. **42**, 4422 (2017).

[69]. S. Zhou, F. W. Wise, and D. G. Ouzounov, "Divided-pulse amplification of ultrashort pulses", Opt. Lett. **32**, 87 (2007).

[70]. Y. Zaouter, F. Guichard, L. Daniault, M. Hanna, F. Morin, C. Hönninger, E. Mottay, F. Druon, and P. Georges, "Femtosecond fiber chirped- and divided-pulse amplification system", Opt. Lett. **38**, 106 (2013).

[71]. M. Kienel, A. Klenke, T. Eidam, S. Hädrich, J. Limpert, and A. Tünnermann, "Energy scaling of femtosecond amplifiers using actively controlled divided-pulse amplification", Opt. Lett. **39**, 1049 (2014).

[72]. H. Stark, M. Müller, M. Kienel, A. Klenke, J. Limpert, and A. Tünnermann, "Electro-optically controlled divided-pulse amplification", Opt. Express **25**, 13494 (2017).

[73]. T. Zhou, J. Ruppe, C. Zhu, I. Hu, J. Nees, and A. Galvanauskas, "Coherent pulse stacking amplification using low-finesse Gires-Tournois interferometers", Opt. Express **23**, 7442 (2015).

[74]. H. Pei, J. Ruppe, S. Chen, M. Sheikhsofla, J. Nees, and A. Galvanauskas, "Multi-mJ Ultrashort Pulse Coherent Pulse Stacking Amplification in a Yb-doped 85μm CCC Fiber

Based System", in Conference on Lasers and Electro-Optics (Optical Society of America, 2017), paper SM1L.2.

[75]. S. Breitkopf, T. Eidam, A. Klenke, L. von Grafenstein, H. Carstens, S. Holzberger, E. Fill, T. Schreiber, F. Krausz, A. Tünnermann, I. Pupeza, and J. Limpert, "A concept for multiterawatt fibre lasers based on coherent pulse stacking in passive cavities", Light Sci. Appl. **3**, e211 (2014).

[76]. M. Kienel, M. Müller, A. Klenke, T. Eidam, J. Limpert, and A. Tünnermann, "Multidimensional coherent pulse addition of ultrashort laser pulses", Opt. Lett. **40**, 522 (2015).

[77]. M. Kienel, M. Müller, A. Klenke, J. Limpert, and A. Tünnermann, "12 mJ and 1 kW Ultrafast Fiber-Laser System using Spatial and Temporal Coherent Pulse Addition", in Advanced Solid State Lasers (Optical Society of America, 2016), paper AM4A.3.

[78]. A. Klenke, E. Seise, J. Limpert, and A. Tünnerman, "Basic considerations on coherent combining of ultrashort laser pulses", Opt. Express **19**, 25379 (2011).

[79]. L. Daniault, M. Hanna, L. Lombard, Y. Zaouter, E. Mottay, D. Goular, P. Bourdon, F. Druon, and P. Georges, "Impact of spectral phase mismatch on femtosecond coherent beam combining systems", Opt. Lett. **37**, 650 (2012).

[80]. S. Jiang, M. Hanna, F. Druon, and P. Georges, "Impact of self-phase modulation on coherently combined fiber chirped-pulse amplifiers", Opt. Lett. **35**, 1293 (2010).

[81]. S. Palese, E. Cheung, G. Goodno, C. C. Shih, F. Di Teodoro, T. McComb, and M. Weber, "Coherent combining of pulsed fiber amplifiers in the nonlinear chirp regime with intra-pulse phase control", Opt. Express **20**, 7422 (2012).

[82]. F. Guichard, L. Lavenu, M. Hanna, Y. Zaouter, and P. Georges, "Coherent combining efficiency in strongly saturated divided-pulse amplification systems", Opt. Express **24**, 25329 (2016).

[83]. Y. Feng, B. M. Zhang, and J. Nilsson, "Photodarkening-induced phase distortions and their effects in single-channel and coherently combined Yb-doped fiber chirped pulse amplification systems", J. Lightwave Technol. **36**, 5521 (2018).

[84]. L. Daniault, M. Hanna, L. Lombard, Y. Zaouter, E. Mottay, D. Goular, P. Bourdon, F. Druon, and P. Georges, "Coherent beam combining of two femtosecond fiber chirped-pulse amplifiers", Opt. Lett. **36**, 621 (2011).

[85]. L. A. Siiman, W. Chang, T. Zhou, and A. Galvanauskas, "Coherent femtosecond pulse combining of multiple parallel chirped pulse fiber amplifiers", Opt. Express **20**, 18097 (2012).

[86]. A. Klenke, S. Hädrich, T. Eidam, J. Rothhardt, M. Kienel, S. Demmler, T. Gottschall, J. Limpert, and A. Tünnermann, "22 GW peak-power fiber chirped-pulse amplification system", Opt. Lett. **39**, 6875 (2014).

[87]. M. Müller, A. Klenke, A. Steinkopff, H. Stark, A. Tünnermann, and J. Limpert, "3.5 kW

coherently combined ultrafast fiber laser", Opt. Lett. **43**, 6037 (2018).

[88]. A. Brignon, "Coherent laser beam combining", Wiley-VCH, 2013.

[89]. L. Daniault, M. Hanna, D. N. papadopoulos, Y. Zaouter, E. Mottay, F. Druon, and P. Georges, "Passive coherent beam combining of two femtosecond fiber chirped-pulse amplifiers", Opt. Lett. **36**, 4023 (2011).

[90]. Y. Zaouter, L. Daniault, M. Hanna, D. N. papadopoulos, F. Morin, C. Hönninger, F. Druon, E. Mottay, and P. Georges, "Passive coherent combination of two ultrafast rod type fiber chirped pulse amplifiers", Opt. Lett. **37**, 1460 (2012).

[91]. J. Bourderionnet, C. Bellanger, J. Primot, and A. Brignon, "Collective coherent phase combining of 64 fibers", Opt. Express **19**, 17053 (2011).

[92]. T. M. Shay, V. Benham, J. T. Baker, A. D. Sanchez, D. Pilkington, and C. A. Lu, "Self-synchronous and self-referenced coherent beam combination for large optical arrays", IEEE J. Sel. Top. Quantum Electron. **13**, 480 (2007).

[93]. V. Lozovoy, I. Pastirk, and M. Dantus, "Multiphoton intrapulse interference. IV. Ultrashort laser pulse spectral phase characterization and compensation", Opt. Lett. **29**, 775 (2004).

[94]. H. Yu, Z. Zhang, X. Wang, R. Su, H. Zhang, Y. Ma, P. Zhou, and J. Chen, "High average power coherent femtosecond pulse combining system based on an all fiber active control method", Laser Phys. Lett. **15**, 075101 (2018).

# Chapter 3
# High-energy narrow-linewidth linearly-polarised pulse-burst Yb-doped fibre amplifier system

## 3.1 Overview

One key objective of our research project is to investigate and characterize fundamental of short-pulse propagation and nonlinear phase effects in high power, high energy fibre amplifiers and their application on coherent beam combination (CBC). In this chapter, it is dedicated to an overview of a high-energy narrow-linewidth linearly-polarised pulse-burst Yb-doped fibre amplifier system, which will be applied on the investigations of the phase distortions, fluctuations within the pulse-burst combined with the amplitude and phase controls for the CPSA application in Chapter 4 and 5. The details of seed source and pulse-burst generation, four cascaded PM-fibre pre-amplifiers, and a low-birefringence low-NA large-mode-area fibre-based main amplifier are fully described in Section 3.2. The pump contributed phase noise is characterized and the relevant results are given in Section 3.3. Finally, Section 3.4 summaries the established system.

## 3.2 Narrow-linewidth linearly-polarised pulse-burst Yb-doped fibre amplifier system

The schematic of the narrow-linewidth linearly-polarised pulse-burst Yb-doped fibre amplifier system is illustrated in Figure 3.1. Generally, it is difficult to generate sufficiently narrow pulses from an externally modulated seed-LD. Instead, I used an electro-optic amplitude modulator (EOAM) to produce 1-MHz bursts of 50 1-ns pulses with 10-ns separation, while the seed-LD operated CW. The bursts were pre-amplified by four Yb-doped fibre amplifiers (YDFAs), which were co-pumped and fully fibreised with PM fibres. An intermediate acousto-optic modulator (AOM) reduced the burst repetition rate to 100 kHz for high energy extraction. After each amplifier, a polarising isolator rejected orthogonally polarised light, including ASE. Finally, counter-pumped by a low-birefringence low-NA large-mode-area Yb-doped fibre, the bursts were amplified with an output of 250-W average power and 2.5-mJ burst energy.

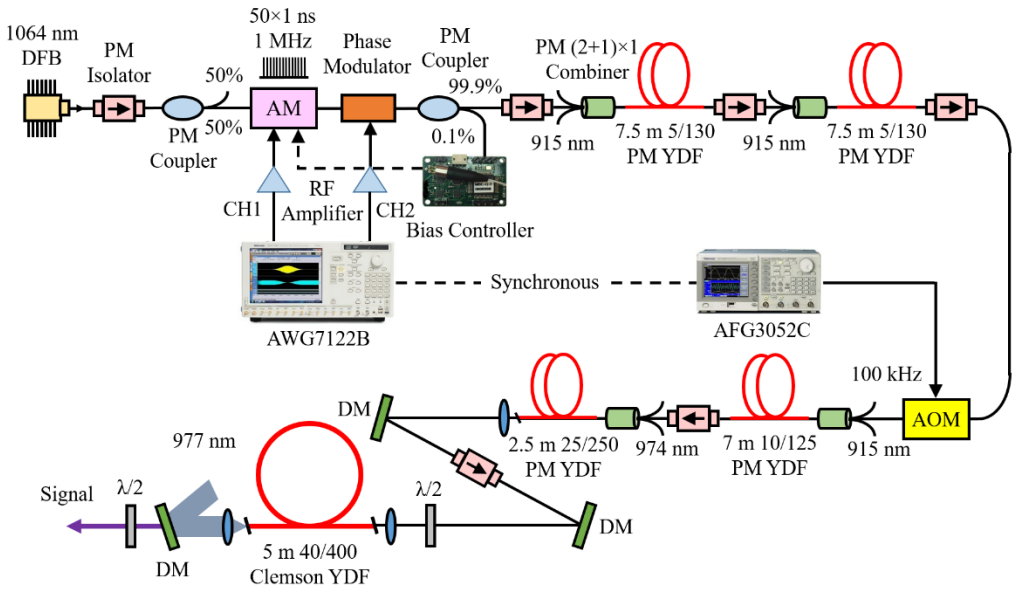


Figure 3.1: Schematic of the narrow-linewidth linearly-polarised pulse-burst Yb-doped fibre amplifier system.

### 3.2.1 Seed source and pulse-burst generation

Here, a single-frequency CW distributed-feedback (DFB) diode laser (II-VI CMDFB1064A, driven by a Newport Model 560 laser diode driver) with a 3-dB linewidth of <1 MHz and 30 dB side mode suppression ratio (SMSR) was used as the seed source. Its linewidth corresponds to a coherence length of ~95 m if a Lorentzian optical spectrum is assumed. The selection of narrow linewidth, i.e., large coherence length ensures that a pronounced interference can be achieved even with a large optical path length difference between the signal and the reference in the phase measurement, described later in Section 4.4. Figure 3.2 (a) shows the power characteristics of the seed source, whilst Figure 3.2 (b) shows the resulting spectrum at an output power of 140 mW, measured by an Ando AQ6315E optical spectrum analyser (OSA). The choice of this output power is based on the power handling capability of the followed EOAM. The spectrum had a central wavelength of 1063.4 nm and a 3-dB bandwidth of 0.11 nm at a resolution of 0.05 nm.

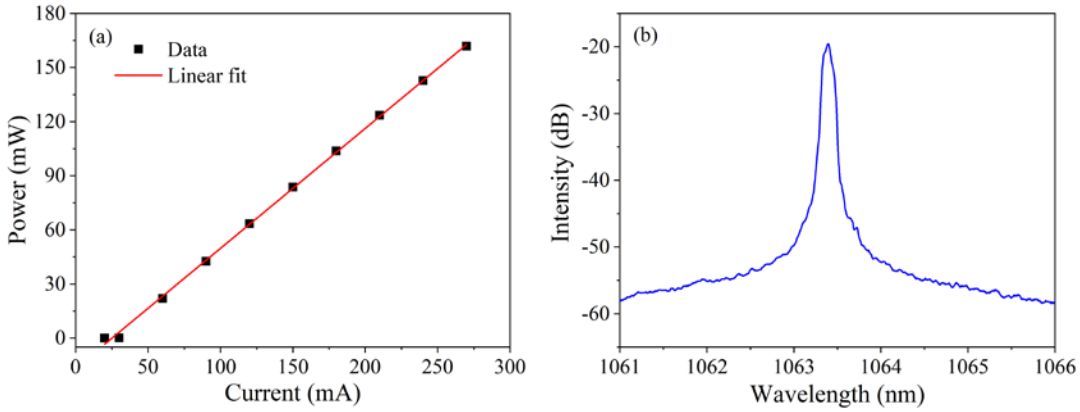


Figure 3.2: (a) II-VI single mode diode laser output power as a function of pump current. (b) Output spectrum at a power of 140 mW, resolution: 0.05 nm.

The CW seed source was protected by a PM fast-axis-blocking fibre isolator (AFW Technologies). This was in turn spliced to an 50/50 tap-coupler (Gooch & Housego) where half of the power was tapped off to serve as a CW reference, described later in Section 4.4. The EOAM (EOSpace AZ-2K5-10-PFU-PFU-108, 10-GHz bandwidth, 21-dB extinction ratio, 2.3-dB insertion loss) used to modulate the CW light from the seed-LD was driven by radio-frequency (RF) pulses (4 V peak-to-peak) from an arbitrary waveform generator (AWG, Tektronix AWG7122B, 12 GS/s sampling rate) followed by a RF amplifier (Mini-Circuits ZPUL-30P). The EOM produced 1-MHz bursts of 50 1-ns pulses with 10-ns separation. The temporal trace of the pulse-burst with a pulse peak fluctuation of 1% is shown in Figure 3.3. These pulses have a transform-limited bandwidth of ~0.44 GHz. Generally, stimulated Brillouin scattering (SBS) is the most severe restriction for high-power narrow-linewidth operation. However, in the short pulse fibre amplifier, the interaction length could be very short and thus SBS is suppressed, pulses of 1-ns duration are sometimes viewed as not limited by SBS [1]. Additionally, the response time of SBS is governed by the acoustical phonon lifetime of 10 ns. A setting of 10-ns separation exactly avoids a successive interaction before encountering the next coming pulse. Furthermore, the appearing SPM will broaden the spectrum to sufficiently suppress SBS. On the other hand, a broadened spectrum may well be undesired, and is also a problem for the coherent combination. Therefore, a spectrum at, or close to, the transform limit is often preferable.

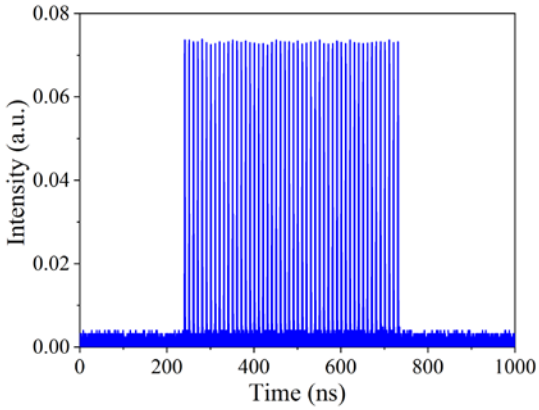


Figure 3.3: Temporal trace of the 1-MHz bursts of 50 1-ns pulses with 10-ns separation.

Furthermore, the repetition rate was 1 MHz in order to saturate the first YDFA. A phase modulator was also included and reserved for the future phase controlling, will be described in Chapter 5. Then a weak feedback signal divided from the subsequent 99.9/0.1 tap-coupler was received by a bias controller (YY Labs Mini-MBC-1), which locks the EOAM at an appropriate working point and thus ensures an adequate extinction ratio. A followed PM isolator (AFW Technologies) was also used to prevent the counter-propagation radiation on the EOAM. Thus, the first-stage amplifier input signal average power was only ~0.3 mW due to the high insertion losses of the EOAM (2.3 dB), the phase modulator (2.6 dB) and the PM isolator (2.6 dB), together with a low duty cycle (5%). The polarisation extinction ratio (PER) from the EOAM output was measured to 21.8 dB.

### 3.2.2 Four cascaded PM-fibre pre-amplifiers

A 7.5 m long PM Yb-doped fibre (Nufern PM-YDF-5/130-VIII) which has a 5 μm core diameter with a 0.12 core NA and a cladding absorption of 0.55±0.10 dB/m at 915 nm was adopted in the first-stage amplifier. It is note that the choice of the gain fibre length (including the subsequent amplifiers) was determined by a desired signal gain calculated from the fibre emission and absorption cross-sections. Besides, the position of the output ASE component can further assist to optimize the fibre length. The gain fibre was co-directionally cladding-pumped by a 915 nm multimode diode laser (JDS Uniphase) using a (2+1)×1 pump combiner (LightComm Technology). At the output, a homemade cladding light stripper (CLS) was used to strip the unabsorbed pump light. A PM isolator (AFW Technologies) with built-in bandpass filter (Advanced Fibre Resources Ltd) removed the ASE and blocked the backward-propagating light. Figure 3.4 (a) shows the signal output power as a function of pump power. An average power of ~150 mW was chosen as the first-stage amplifier output. This 150-mW power corresponds to a 0.15-μJ burst energy, which is far lower than the 9-μJ calculated

saturation energy of the gain fibre. The output spectrum at this output power is shown in Figure 3.4 (b). The output spectrum displayed an extinction ratio (ER) of 25 dB between the laser signal and the ASE. The Figure 3.4 (b) inset shows that the spectrum has a 3-dB bandwidth of 0.08 nm. The PER from the isolator was about 23 dB.

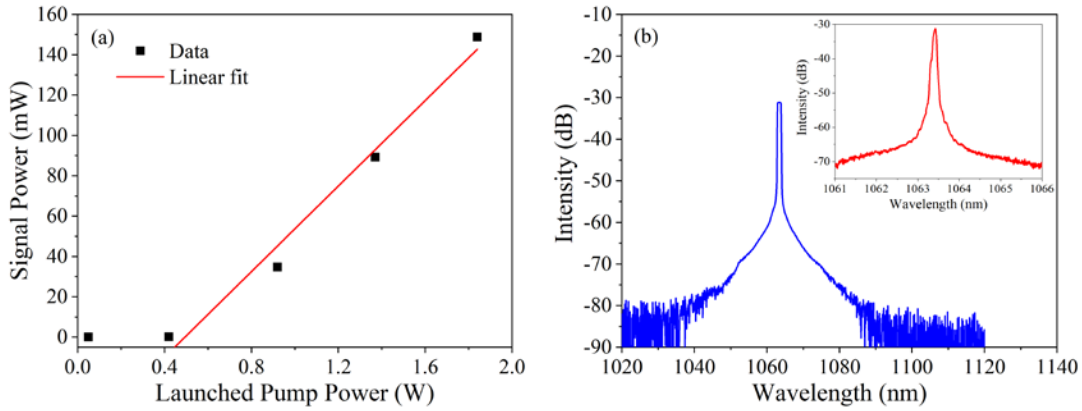


Figure 3.4: (a) First-stage amplifier output power as a function of pump power and (b) output spectrum (150 mW) at 1 nm and 0.05 nm resolution (inset).

For the second YDFA, it had a structure which is identical to the first YDFA. Then an AOM (Gooch & Housego T-M200-0.1C2G-3-F2P with driver Gooch & Housego 1200AF-DINA-2.5 HCR) was used to reduce the burst repetition rate to 100 kHz for high energy extraction. A 24 V direct current supply voltage was applied on the AOM driver. An arbitrary function generator (AFG, Tektronix AFG3052C) generated an electrical pulse with a 550-ns duration and a 100-kHz repetition rate to pick up one burst within ten input burst periodically. It was functionally realized by synchronizing both RF signals applied onto the EOAM and AOM. Moreover, the electrical signal from the AFG was also set with an appropriate time delay to compensate the optical delay introduced by the length of fibres. Again, a 99.9/0.1 tap-coupler (Advanced Fibre Resources Ltd) monitored the AOM output and backward SBS.

The second-stage amplifier (from the AOM) output power as a function of pump power is shown in Figure 3.5 (a). The output power increased linearly with the pump power and there was no roll-off at the maximum output power. Limited by the 1-W maximum handling power and 4-dB insertion loss of the AOM, an output power of 28 mW was chosen in the second-stage amplifier. The corresponding burst energy was estimated to 0.28 μJ, which is again far lower than the gain fibre saturation energy. The corresponding output spectrum is shown in Figure 3.5 (b). The spectrum ER of the signal-to-ASE was remained ~25 dB and the 3-dB bandwidth was 0.06 nm. It was also confirmed that the output bursts from the AOM has a temporal contrast of 36 dB.

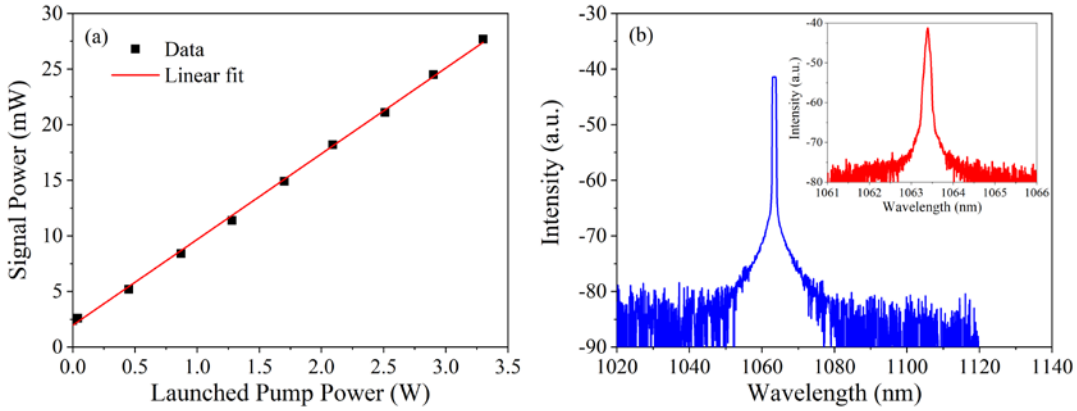


Figure 3.5: (a) Second-stage amplifier (from the AOM) output power as a function of pump power and (b) output spectrum (21 mW) at 1 nm and 0.05 nm resolution (inset).

In the third YDFA, a 7-m Yb-doped fibre (Nufern PLMA-YDF-10/125-VIII) was utilized as the gain fibre, which has an 11-μm core diameter with a 0.075 core NA, and an absorption of 1.30±0.20 dB/m at 915 nm. It was co-directionally cladding-pumped by a 915 nm multimode diode laser (JDS Uniphase) by means of a (2+1)×1 pump combiner (LightComm Technology). At the output, a homemade CLS was used to strip the unabsorbed pump light and a high-power isolator (Advanced Fibre Resources Ltd) was used to prevent feedback. A 99.9/0.1 custom-made tap-coupler (LightComm Technology) was used to monitor the backward SBS. The output power characteristics of the third-stage amplifier are shown in Figure 3.6 (a) and Figure 3.6 (b) shows the corresponding output spectra. The spectrum ER of the signal-to-ASE was >20 dB and the 3-dB bandwidth was 0.1 nm. The maximum output power was 0.9 W which corresponds to a burst energy of 9 μJ and a burst peak power (average) of 0.18 kW. The saturation energy of the 10/125 YDF was calculated to 25 μJ. Thus, there is no evident gain saturation in this stage. The PER from the third-stage amplifier was measured to be 18.5 dB.

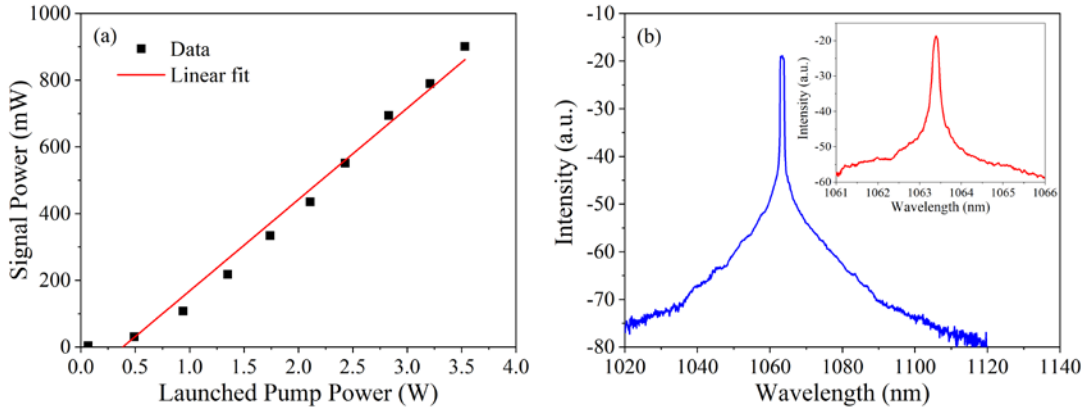


Figure 3.6: (a) Third-stage amplifier output power as a function of pump power and (b) output spectrum (0.9 W) at 1 nm and 0.05 nm resolution (inset).

In the fourth YDFA, a 2.5 m Yb-doped fibre (Nufern PLMA-YDF-25/250-VIII) with a 25 μm

core diameter, a 0.06 core NA and an absorption of 5.1 dB/m at 975 nm was utilized as the gain fibre. The fibre end facet was cleaved with an angle of 6° to prevent reflected light going back into the fibre core. It was co-directionally cladding-pumped by four 974 nm multimode LDs (IPG PLD-33-974) by means of a (6+1)×1 pump combiner (LightComm Technology). At the output, the residual co-propagating pump light was filtered out by a dichromic mirror (DM), while the signal was reflected at a small incident angle. Then the signal went through a high-power free-space polarisation-dependent isolator (OFR IO-5-1064-HP) which is used to prevent detrimental feedback. The output power varied linearly with respect to the launched pump power, as shown in Figure 3.7 (a). A signal with 9-W output power was utilized to seed the main amplifier and the corresponding output spectrum is shown in Figure 3.7 (b). The spectrum ER of the signal-to-ASE was kept >20 dB and the 3-dB bandwidth was 0.09 nm. Taking into account a 1.8-dB isolator insertion loss, the achieved burst energy within the gain fibre was 0.13 mJ. The saturation energy of the 25/250 YDF was estimated to 0.2 mJ. According to the Frantz-Nodvik equation [2], the amplitude of the leading pulse within a burst is 1.85 times the trailing pulse. Thus, with a 9-W output power, the burst peak power (average) was 1.8 kW while the peak power of the leading pulse reached 2.5 kW. The PER from the isolator of the fourth-stage amplifier was measured to be ~20 dB.

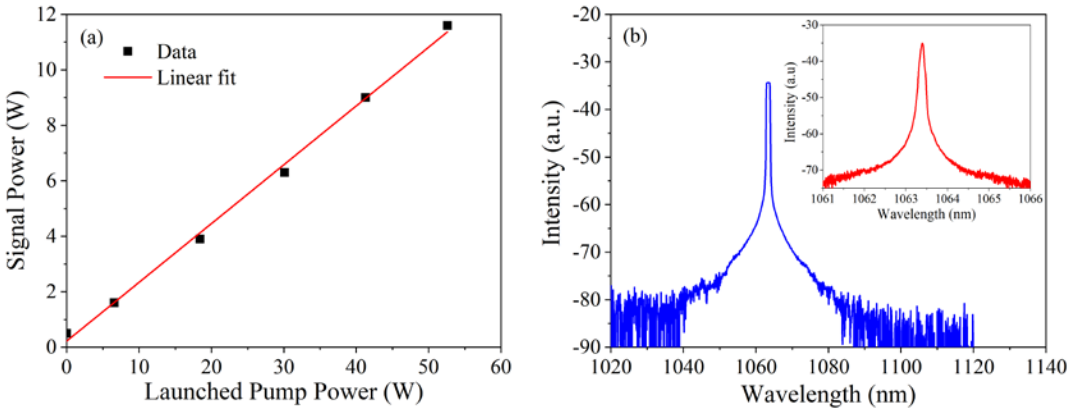


Figure 3.7: (a) Fourth-stage amplifier output power as a function of pump power and (b) output spectrum (9 W) at 1 nm and 0.05 nm resolution (inset).

Though the 1-ns pulses (particularly with a potential broadened spectrum) may not cause a SBS effect in the amplifiers. However, the CW components are still possible to induce a significant SBS effect. In terms of the CW component between the bursts, it is negligible because the AOM had guaranteed a 36-dB temporal contrast. On the other hand, the CW component located between the pulses within the burst would be considerable due to an intrinsic low EOAM ER (21 dB). Besides, the electrical response time and deviation of the bias controller will further degrade its ER performance. Thus, the potential backward SBS from the fourth-stage amplifier was measured and characterized.

The backward output power varied with the fourth-stage amplified signal power is shown in Figure 3.8 (a). At the maximum output power (9 W), the backward output power was 92 µW which means that the backward power to the system was about 20 mW. Figure 3.8 (b) shows the backward output spectrum at a low and maximum amplified signal power. The centre wavelength of the spectrum was 1063.37 nm. The red-shift wavelength was calculated to be 0.04 nm by assuming a Stokes shift of 10 GHz [1]. As pointed out by the arrow in Figure 3.8 (b), there was a slightly elevated spectrum peak around 1063.45 nm, which might have a deviation due to a 0.05 nm resolution. Thus, it is obvious that the SBS starts to grow, however, is still negligible under this output power.

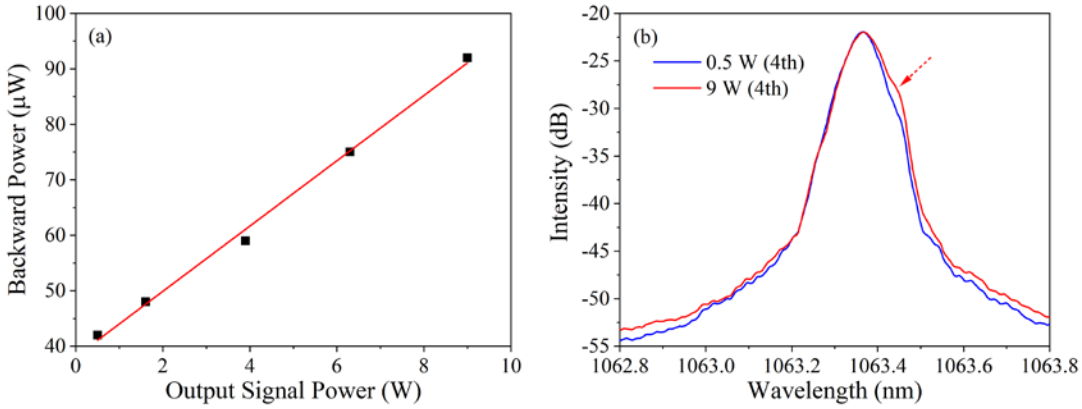


Figure 3.8 (a) Monitored backward output power *vs.* the fourth-stage output signal power. (b) Backward output spectrum at a low and maximum amplified signal power, resolution: 0.05 nm.

### 3.2.3 Non-PM low-NA LMA Yb-doped fibre based main amplifier

It is noted that when a PM fibre operates in the high-power region, the thermal stress can reach a same order of the material-induced stress. Thus, the PM fibre can hardly preserve a good polarisation state for high-power fibre amplifiers. Alternatively, it has been verified that a linearly polarised laser output can be achieved through an active polarisation control in narrow linewidth non-PM Yb-doped fibre amplifiers [3,4]. Though, in multi-mode or few-mode fibres, it is difficult to guarantee that the higher order (transverse) modes has the same state of polarisation as the fundamental mode [5]. In other words, the degree of polarisation of the output laser must be degraded when the fraction of higher order modes increases. Notably, as in Ref. [6], the loosely-coiled low-birefringence final amplifier maintains the polarisation. Therefore, it is possible for a long-coiled booster non-PM fibre to mitigate thermal effects even at high power and maintain polarisation by virtue of a low birefringence.

In the main amplifier, the gain fibre was a 5-m length non-PM LMA Yb-doped fibre

(DB01216). It is fabricated by Clemson University with an improved technique which effectively eliminates the NA limit of ~0.06 of conventional approaches and opens up a new possibility for larger cores with improved mode quality [7]. Its phosphosilicate core had a hexagonal shape with 42 μm flat-to-flat and 46 μm corner-to-corner size, and a 0.028 core NA (i.e. $\Delta N=2.7\times10^{-4}$), which corresponds to a V parameter of 3.3. The pump would be guided in a 411 μm flat-to-flat and 431 μm corner-to-corner hexagonal cladding. The fibre facet image is shown in Figure 3.9 (a). As shown in Figure 3.9 (b), the absorption and emission cross-sections of the fibre were used to design and optimize the main amplifier. The measured pump absorption is ~4.5 dB/m at 976 nm, from which I estimated an $Yb^{3+}$-concentration to be as high as $8.78\times10^{25}$ $m^{-3}$.

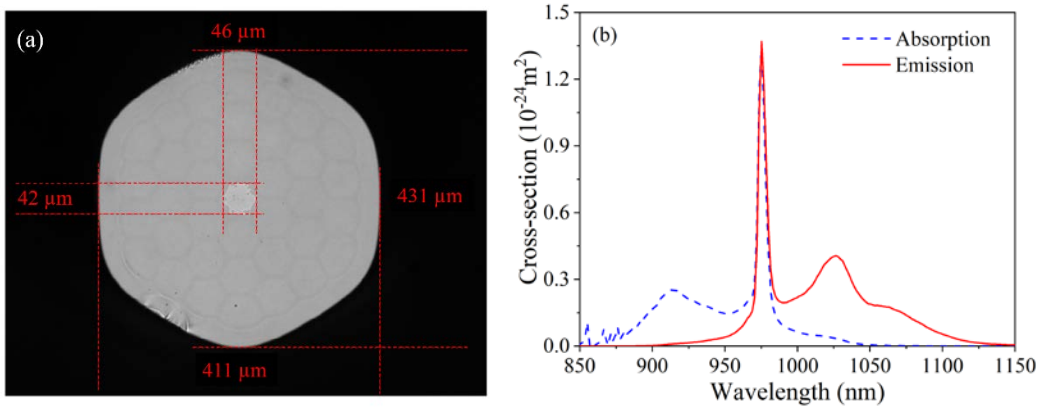


Figure 3.9: (a) Fibre facet image and (b) absorption and emission cross-sections of the low-NA LMA Yb-doped fibre.

In practice, the fibre was coiled to 1-m diameter to mitigate bend loss due to a low NA. Both two fibre end facets were angle-cleaved at ~6° to suppress parasitic lasing. The signal is launched into the fibre through a DM that filters out any backward unabsorbed pump and a 30-mm focal length aspheric lens. A 1.1-kW diode-laser-stack-based source (Laserline LDL 80-1000) centred at 977 nm was used to counter-pump the fibre via a combination of lenses and a DM. Two half-wave plates, located at the input and output of the gain fibre, were finely rotated to get an optimized and stable linear-polarisation output.

Figure 3.10 (a) shows the average output power from the main amplifier *vs.* absorbed pump power. It reached a maximum output power of 250 W with a slope efficiency of 62.3%. I attributed this low slope efficiency mainly to a small emission cross-section at 1064 nm ($1.7\times10^{-25}$ $m^2$) and a comparatively large bend loss (~0.6 dB/m) [7]. The pulse-burst temporal trace from the main amplifier is shown in Figure 3.10 (b). The burst had a total energy of 2.5 mJ, which is ~3.6 times the calculated 0.7 mJ saturation energy. The burst peak power (average) was 50 kW, while the peak power and energy of the leading pulse were as high as

0.45 MW and 0.45 mJ. Within the final stage, gains of the leading and trailing pulses were 23 and 9 dB, respectively.

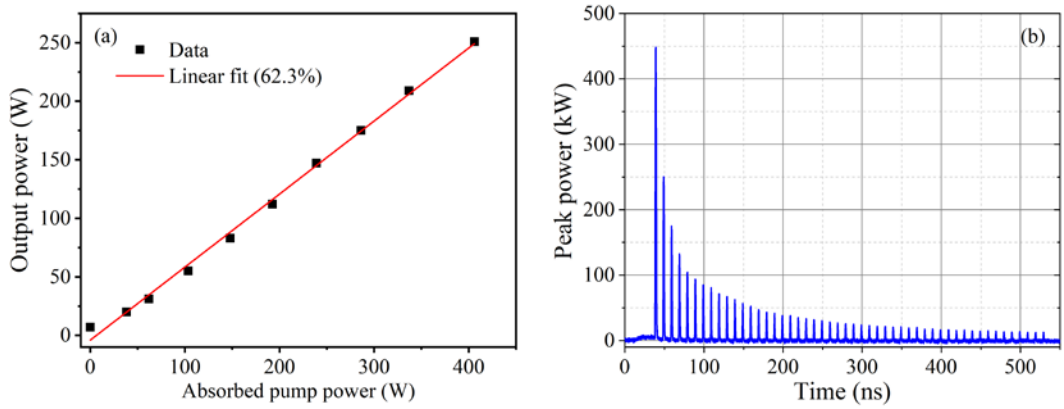


Figure 3.10: (a) The average output power from the main amplifier *vs.* absorbed pump power and (b) output pulse-burst temporal trace at a maximum output power.

For short pulse (with a duration below the upper-state lifetime) amplification, the pulse temporal profile in the amplification process can be accurate expressed by the simplified Frantz-Nodvik equations [8,9], which is given by

$$I_{out}(t) = \frac{I_{in}(t)}{1 - [1 - exp(g_0)^{-1}] \times \exp(-t \times E_{in}/E_{sat})}, \tag{3.1}$$

$$E_{out} = E_{sat} ln\{1 + g_0[exp(E_{in}/E_{sat}) - 1]\}, \tag{3.2}$$

where $I_{out}(t)$ and $I_{in}(t)$ are output and input time-independent pulse intensities in temporal regime, respectively, $g_0$ is the initial small-signal gain coefficient, $E_{out}$ and $E_{in}$ are the output and input energies of the amplified pulse. Furthermore, the saturation energy is $E_{sat} = A_{eff} h\nu_s/[(\sigma_{es} + \sigma_{as})\Gamma_s]$, where $A_{eff}$ is the effective mode area, $h\nu_s$ is the signal photon energy, $\sigma_{es}$ and $\sigma_{as}$ are the emission and absorption cross-sections at the signal wavelength, and $\Gamma_s$ is the signal overlap with an active dopant. Based on the $\sigma_{as}$ and $\sigma_{es}$ data, and a 29-μm MFD [7], the saturation energy was estimated to ~0.7 mJ. Then the burst temporal profile was calculated via the equation (3.1) and (3.2) and shown in Figure 3.11. The figure indicates that there is a good agreement between the Frantz-Nodvik equations predicted pulse saturation performance and the measured data.

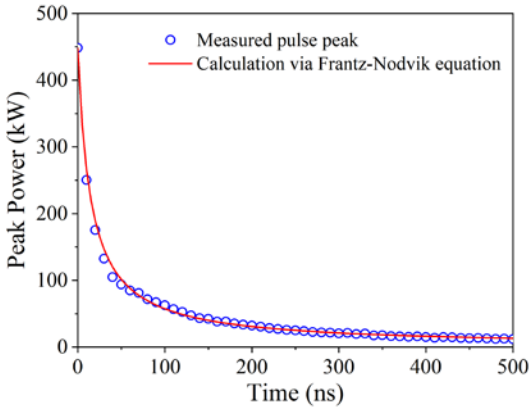


Figure 3.11: Retrieved pulse peaks within the burst and calculated burst profile.

From the measured spectrum shown in Figure 3.12 (a), the ASE component was estimated to <5% of the output power. The central wavelength of the output laser was at 1064 nm. The beam quality factor ($M^2$) of the output signal was measured using a scanning-slit beam profiler (Thorlabs BP104-IR) and the result can be seen in Figure 3.12 (b). At maximum output power, the $M^2$-factor became 1.08 and 1.12 in orthogonal directions, according to a hyperbolic fit to the measured beam width at the $1/e^2$ intensity-level. Finally, the PER of the output signal was measured to 19 dB, which can be attributed to a successful single-mode and narrow linewidth operation in the low-birefringence fibre.

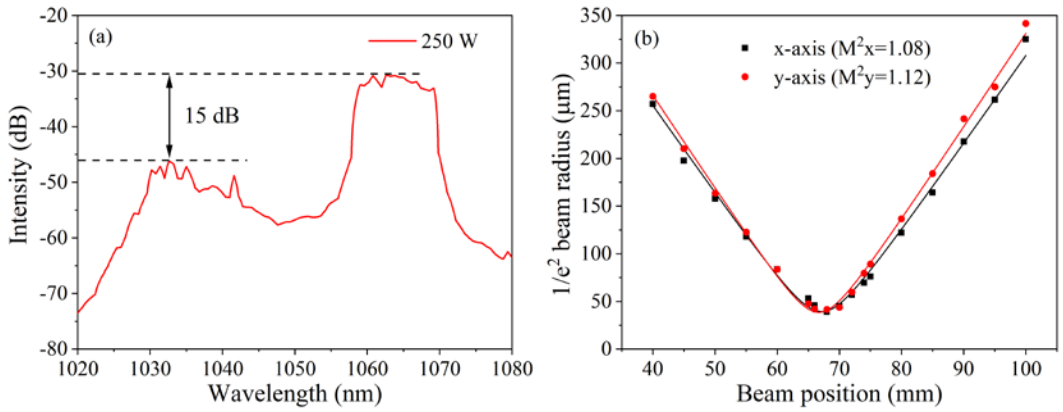


Figure 3.12: (a) Measured output spectrum at a resolution of 10 nm and (b) $1/e^2$ intensity beam radius of the output signal in x-axis and y-axis directions at maximum output power.

## 3.3 RF measurement of the pump diode

On the one hand, an optimized amplifier chain design is required to minimize the pulse phase noise with a higher energy output. On the other hand, compared to the CW and long-pulse regimes, the efficient combination of ultrafast pulses requires the optical phase to be matched over the whole spectrum. All these suggests that the phase noise should be characterized and

analysed. The main phase noises include low-frequency thermal noise, medium-frequency mechanical vibration noise and high-frequency electrical noise. The bandwidth of these noises is typically limited to several 10 kHz. Here, to measure the noise contributions of the diode laser driver (electrical noise).

I carried out this comparison experiment with three different drivers: LDI-820 (S/N: 210648), SDL-820 (S/N: B682) and TDK Lambda (GEN40-38/LN, S/N: LOC540A066-0005). Due to the limited maximum drive current of the drivers, a 10-A current was used to drive the multimode diode laser (JDSU) with a maximum output power of ~7 W. The measured RF spectra under a low power output (50 mW) and a nearly full power output (7 W) were illustrated in Figure 3.13. The DET data shows the detector background noise. I found that these diode laser drivers did not contribute additional noises even with high power output. In the later experiment, other phase noise will also be measured and analysed.

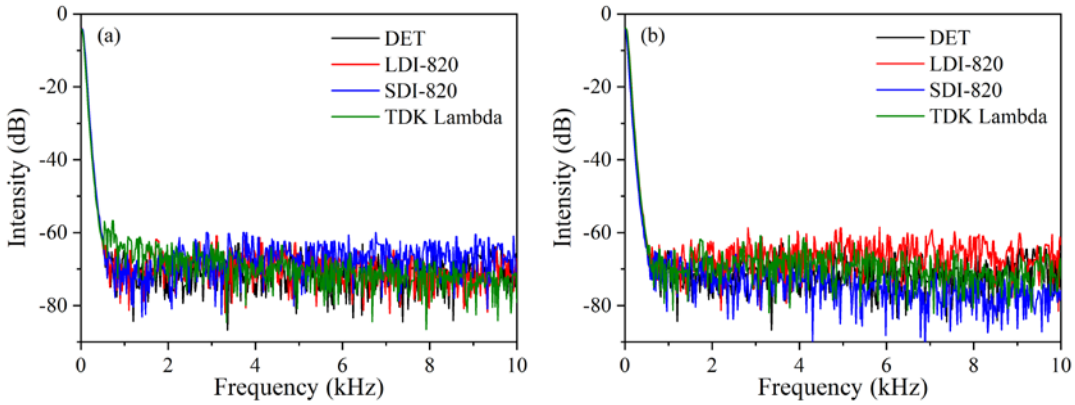


Figure 3.13: RF spectra under (a) 50 mW and (b) 7 W output power with three different drivers (resolution: 100 Hz). The DET data indicates our detector noise floor.

## 3.4 Conclusion

I have demonstrated the feasibility of fibre-based sources for high-energy narrow-linewidth linearly-polarised pulse bursts at high average power. Such sources can be used for CPSA and applications such as lidar that that require high-coherence high-energy pulses or pulse bursts. However, the high gain and strong ASE in the main amplifier might be an issue for a stable long-term operation. Meanwhile, the high portion of excited-state population ($n_2$) can also cause self-pulsing before reaching the burst. Therefore, this amplifier system with a lower power output will be applied on both the measurements and controls of the pulse-burst amplitude and phase in Chapter 4 and 5.

## References

[1]. G. P. Agrawal, “Nonlinear fiber optics”, Academic Press, San Diego, 2000.

[2]. M. Cheng, Y. Chang, A. Galvanauskas, P. Mamidipudi, R. Changkakoti, and P. Gatchell, “High-energy and high-peak-power nanosecond pulse generation with beam quality control in 200-μm core highly multimode Yb-doped fiber amplifiers”, Opt. Lett. **30**, 358 (2005).

[3]. Y. Wang, Y. Feng, X. Wang, H. Yan, J. Peng, W. Peng, Y. Sun, Y. Ma, and C. Tang, “6.5 GHz linearly polarized kilowatt fiber amplifier based on active polarization control”, Appl. Opt. **56**, 2760 (2017).

[4]. G. D. Goodno, S. J. McNaught, J. E. Rothenberg, T. S. McComb, P. A. Thielen, M. G. Wickham, and M. E. Weber, “Active phase and polarization locking of a 1.4 kW fiber amplifier”, Opt. Lett. **35**, 1542 (2010).

[5]. N. Andermahr, T. Theeg, and C. Fallnich, “Novel approach for polarization-sensitive measurements of transverse modes in few-mode optical fibers”, Appl. Phys. B **91**, 353 (2008).

[6]. Z. Huang, S. Pidishety, T. W. Hawkins, Y. Feng, Y. Feng, S. Zhu, L. Dong, and J. Nilsson, “Low-birefringence 120 W Yb fiber amplifier producing linearly polarized pulses with 69-GHz linewidth at 1083 nm”, in Advanced Solid State Lasers (Optical Society of America, 2018), paper ATu1A.1.

[7]. F. Kong, C. Dunn, J. Parsons, M. T. Kalichevsky-Dong, T. W. Hawkins, M. Jones, and L. Dong, “Large-mode-area fibers operating near single-mode regime”, Opt. Express. **24**, 10295 (2016).

[8]. L. M. Frantz and J. S. Nodvik, “Theory of pulse propagation in a laser amplifier”, J. of Appl. Phys. **34**, 2346 (1963).

[9]. D. N. Schimpf, C. Ruchert, D. Nodop, J. Limpert, A. Tünnermann, and F. Salin, “Compensation of pulse-distortion in saturated laser amplifiers”, Opt. Express **16**, 17637 (2008).

# Chapter 4
# Single-shot amplitude and phase measurement and fluctuation analysis of narrow-line pulse bursts in a divided-pulse amplification system

## 4.1 Overview

As we all know, the optical phase is crucial for CBC. While nonlinear phase distortions have generally been found to be small for CW systems, it becomes increasingly important in high energy, high peak power pulsed sources. A requirement of accurate amplitude and phase control is essential for ensuring a high combined efficiency in CBC systems. The first condition of fulfilling that control is an accurate measurement of amplitude and phase. In this chapter, I characterize the rapid nonlinear intra-pulse phase distortions within a burst, which provides a simple method for understanding of temporal phase responses in highly nonlinear and saturated regime. In Section 4.2, the motivation of realizing an intra-pulse phase characterization in pulse bursts fibre laser systems is firstly introduced. Our initial work focuses on amplitude and phase measurement and fluctuation analysis of narrow-line pulse bursts for a single fibre amplifier in a divided pulse amplification system, as detailed in Section 4.3. Then, in Section 4.4, our measurement technique would be optimized and applied to the cascaded fibre amplifiers, which operate in a highly nonlinear and heavily saturated regime. Finally, the achieved results and analysis are summarized in Section 4.5.

## 4.2 Introduction

Although chirped-pulse amplification (CPA) fibre systems are already leading contenders for a range of femtosecond-pulse applications, SPM and other nonlinearities in the fibre amplifiers impose severe limitations on the achievable pulse energy [1]. As we introduced in Chapter 2, promising approaches in both spatial and temporal coherent beam combination have been proposed and demonstrated for mitigating these nonlinearities in ultrafast pulsed regime [2-5]. Particularly, the temporal combination technique DPA has attracted great attention. In principle, the recombination of the pulses in DPA can be accomplished via passive solution, e.g. through a Sagnac interferometer [6]. While the passive solution is limited by gain saturation compensation when aiming for extracting high energy from the amplifier. Therefore, active solutions have been implemented to control the amplitude differences and phase

mismatches, and improve the combination efficiency [7, 8]. Recently, a so-called CPSA approach [9], is an alternative option for pulse amplification to high peak power and energy. Combined with chirped-pulse amplification, the femtosecond pulses can be stretched to ~1 ns and then further effective stretching by DPA avoids excessive nonlinearities and damage even at high energy extraction [10], with burst energy several times the saturation energy. Undoubtedly, CPSA works with other types of coherent pulses as well, e.g. narrow-line pulse throughout our investigation.

It is obvious that the amplitude and phase distortions would reduce the stacking efficiency of CPSA [9]. Thus, the achievable efficiency can be degraded by gain saturation in the amplifier and any mismatch of the accumulated phase between pulses due to e.g. peak-power-related SPM [11]. Higher peak power is more demanding in that a given relative change results in a larger change of the *B*-integral (which quantifies SPM), and thus in larger stacking-efficiency degradation [12]. Similarly, phase distortions caused by the K-K effect [13] and instantaneous heating [14] resulting from the quantum defect or photodarkening increase with higher pulse energy. To understand the potential of CPSA, it is necessary to characterize amplitude and phase distortions within the amplified burst, and estimate their stability, as affected by gain saturation and nonlinearities in parameter regimes of interest. The intra-pulse nonlinear chirp profile of single pulses has been measured via a best fit for *B*-integrals up to 38 rad [15]. For the case of pulse bursts, it is revealed for the first time through our investigations and the results are presented as followings.

Firstly, I demonstrated single-shot temporal-based interferometric phase measurements for bursts of 35 pulses of 1-ns duration in an YDFA seeded by a 1063-nm single-frequency diode laser with different amounts of saturation and nonlinearity. The aimed interference signal was achieved through mixing the amplified burst and the reference, i.e., input burst to the amplifier. The temporal phase retrieval result shows that the output burst has a *B*-integral of 2.4 rad when the burst energy is 10 μJ (25-μJ saturation energy). The corresponding amplitude and phase profiles, and their stability were also characterized and analysed [16].

A similar phase measurement scheme was then applied on a YDFA chain system, a maximum intra-pulse phase distortion (*B*-integral) of 21.2 rad was determined by mixing the burst with a continuous wave reference. The difference in the *B*-integral between the first and last pulse in the burst was large, 12.8 rad, but can be compensated for. Moreover, burst-to-burst amplitude fluctuations (standard deviation) were below <6%, where phase fluctuations were ~0.6 rad (std) or less. Even if these fluctuations cannot be compensated for, they still allow for efficient coherent combination, which opens up for transform-limited or narrow-line high-energy divided-pulse amplification with single-frequency seeding.

## 4.3 Single-shot amplitude and phase measurement and fluctuation analysis for a single fibre amplifier

### 4.3.1 Experimental setup and method

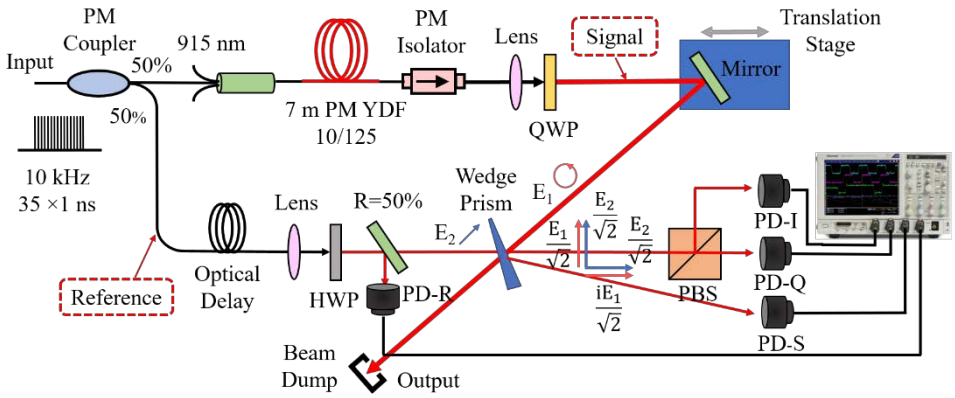


Figure 4.1: Schematic of the pulse-burst fibre amplifier and measurement setup. Pump diodes: JDSU 6397-L3 Series diode laser (915 nm), Pump diode drivers: Laser Driver Inc. Model LDI-820 (1st amplifier), SDL-822 (2nd amplifier).

Figure 4.1 shows the Yb-doped fibre DPA and measurement system. All fibres and fibre components are PM for the signal and reference, which were polarised throughout. The seed was a narrowband, single-frequency (a linewidth specification of <30 MHz) continuous-wave diode laser (Lumics, LU1064M150-1306E10A, driven by a Newport Model 560 laser diode driver) combined with an external fibre Bragg grating and protected by an isolator. An EOAM (EOSpace AZ-2K5-10-PFU-PFU-108) and an AOM (Gooch & Housego T-M200-0.1C2G-3-F2P with driver Gooch & Housego 1200AF-DINA-2.5 HCR) carve bursts of 35 1-ns pulses with 6 ns period. A bias controller (YY Labs Mini-MBC-1) was applied on the EOAM to ensure an adequate extinction ratio. The bursts, running at 10 kHz, are then amplified to 0.37 μJ in two YDFAs (Nufern PM-YDF-5/130-VIII, not shown) and are subsequently divided by a 50/50 fibre splitter into a signal and a reference. Finally, the half of the bursts were amplified by a 10-μm-core YDFA comprising 7 m of Nufern PLMA-YDF-10/125-VIII. At the output of each amplifier, a polarising isolator with built-in bandpass filter removed ASE and blocked backward-propagating light.

Optical heterodyne detection and optical homodyne detection are commonly used to measure gradual changes in the temporal phase [17]. The principle of optical heterodyne detection is based on two independent monochromatic lasers. Generally, an AOM is used to create a frequency shift in the reference for the heterodyne measurement [18]. One issue is that the temporal resolution is limited by the beat frequency. A beat frequency of 10 GHz is required

to achieve a 0.1-ns resolution. Thus, this heterodyne scheme is not suitable for characterizing our fibre laser system. In comparison, the optical homodyne detection is based on a single monochromatic laser and avoids that limitation. Thus, the optical homodyne detection scheme together with the 90° optical hybrid technique [19-21] was chosen to characterize the temporal phase in my investigations. In other words, the measurement of phase distortion is changed to the measurement of amplitude. However, this scheme requires a high-speed analog to digital convertor and a large amount of data analysis, the phase of the signal can be demodulated using software calculation [22].

To retrieve the temporal phase, I measured the instantaneous power of the amplified burst signal $\mathrm{I}_1(\mathrm{t}) = |E_1(t)|^2$ and, following interference with the burst reference $\mathrm{I}_2(\mathrm{t}) = |E_2(t)|^2$, its in-phase $\mathrm{I}_I(\mathrm{t})$ and quadrature (90-shifted) $\mathrm{I}_Q(\mathrm{t})$ homodyne signals via single-shot high-speed detection. Experimentally, I set up a 90° optical hybrid and generated the signals according to Figure 4.1. The output beam from the final amplifier was collimated and passed through a quarter-wave plate (QWP) placed with principal axes at 45° to the linear polarisation of the output beam. The resulting circular polarisation is here best thought of as two linearly polarised components with equal strength and 90° phase difference. For the reference beam, it was synchronized with the output beam via an optical fibre (Nufern PM980-XP) and a free space delay line. A 50% of the collimated reference beam was seperated to characterize its instantaneous power profile $\mathrm{I}_2{}'(t)$. Then a glass wedge at a small angle-of-incidence recombined the output beam with the other half of the collimated reference beam. Controlled by a half-wave plate (HWP), the reference beam was linearly polarised at 45° to the QWP's principal axes, so the combined beam carries both $\mathrm{I}_I(\mathrm{t})$ and $\mathrm{I}_Q(\mathrm{t})$ homodyne signals. These were split by a PBS aligned with the principal axes and then detected along with $\mathrm{I}_1{}'(t)$ (as reflected in the wedge) and $\mathrm{I}_2{}'(t)$ by biased photodiodes PD-I, PD-Q, PD-S, and PD-R (EO Technics ET-3500, bandwidth >12.5 GHz), respectively. A multi-channel, 20-GHz oscilloscope (Tektronix DSA72004B, 50 GSa/s sampling rate in each channel simultaneously) then acquired single-shot traces from these four photodiodes. We get [23]

$$I_I(t) = \left|\frac{E_1(t)}{\sqrt{2}} + \frac{E_2(t)}{\sqrt{2}}\right|^2 = \frac{I_1(t)}{2} + \frac{I_2(t)}{2} + [I_1(t)I_2(t)]^{1/2}\cos[\varphi(t)], \tag{4.1}$$

$$I_Q(t) = \left|\frac{iE_1(t)}{\sqrt{2}} + \frac{E_2(t)}{\sqrt{2}}\right|^2 = \frac{I_1(t)}{2} + \frac{I_2(t)}{2} + [I_1(t)I_2(t)]^{1/2}\sin[\varphi(t)], \tag{4.2}$$

$$\varphi(t) = \tan^{-1}\left\{\frac{I_Q(t) - I_1(t)/2 - I_2(t)/2}{I_I(t) - I_1(t)/2 - I_2(t)/2}\right\}. \quad (4.3)$$

Here, $\varphi(t)$ is the sought-after temporal phase of $E_1(t)$, i.e., of the signal burst, which was finally calculated in MATLAB. Moreover, $\mathrm{I}_1(\mathrm{t})$ and $\mathrm{I}_2(\mathrm{t})$ were indirectly obtained through the measurement and calibration of $\mathrm{I}_1{}'(t)$ and $\mathrm{I}_2{}'(t)$. In all cases, presented results are based on data from 100 bursts which were acquired within 30 s and averaged and used for fluctuation analysis. Although a slow drift could be significant over 30 s, I verified that the fluctuations were similar on a burst-to-burst basis. Note that whereas the whole system contributes to the measured instantaneous power, the measured phase profile corresponds essentially to the final YDFA.

Besides, the electric field of the sub-pulse in a burst is expressed as

$$E_s(t) = \sum_{j=1}^{50} \sqrt{I_j(t)} e^{i\varphi_j(t)}, \quad (4.4)$$

where $I_j(t)$ and $\varphi_j(t)$ are the measured temporal output pulse intensity and phase. Thus, based on the acquired data, the combining efficiency can be calculated as

$$\eta_{eff} = \frac{1}{50}\int |E_s(t) \times E_s^*(t)|dt \Big/ \sum_{j=1}^{50} \int I_j(t)dt. \quad (4.5)$$

### 4.3.2 Experimental results and analysis

The instantaneous power profile averaged over 100 bursts is shown in Figure 4.2. In order to compare different amounts of gain saturation and nonlinearity, I used two different pump powers for the 3rd YDFA, resulting of output burst energies of 2.8 μJ and 10 μJ. In Figure 4.2 (a), the high-power profile shows a characteristic tilt on the power envelope, caused by gain saturation (saturation energy 25 μJ calculated from the fibre parameters), whereas the low-power peaks remain at a nearly constant level. The first and last pulse within the bursts are shown in Figure 4.2 (b) with an enlarged and shifted time scale. Due to different amounts of gain saturation, the amplitudes of the first pulse were 1.58 and 1.31 times as high as for the last pulse for the high-power (HP) and low-power (LP) outputs, respectively. For comparison, the gain compression values expected from the extracted energies (2.8 μJ and 10 μJ) became 1.47 and 1.1, respectively.

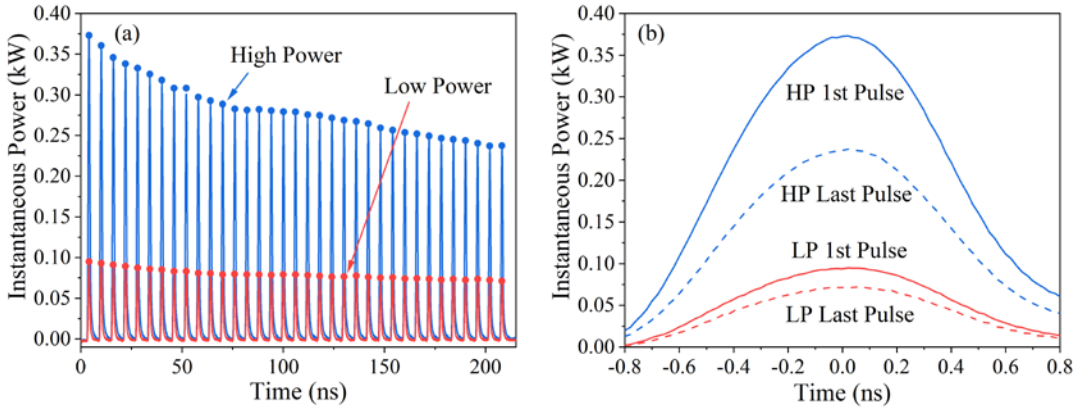


Figure 4.2: Instantaneous output power averaged over 100 bursts for high and low power (a) for the whole burst and (b) the first and last pulse.

The standard deviation (std) in the peak power of the individual pulses for 100 bursts was calculated and shown in Figure 4.3 (a). Overall, the std had a similar trend as the peak shown in Figure 4.2 (a). For the low power case, the std was stabilized to ~0.5 W for 35 individual pulses, while the std varied in the range from 0.8 W to 1.7 W in terms of the high-power case. In Figure 4.3 (b), the fluctuations were nearly located between 3% and 6% of the instantaneous power for both high and low power. Besides, the pulse peak fluctuation at the input to the 3rd YDFA was measured to be 1%.

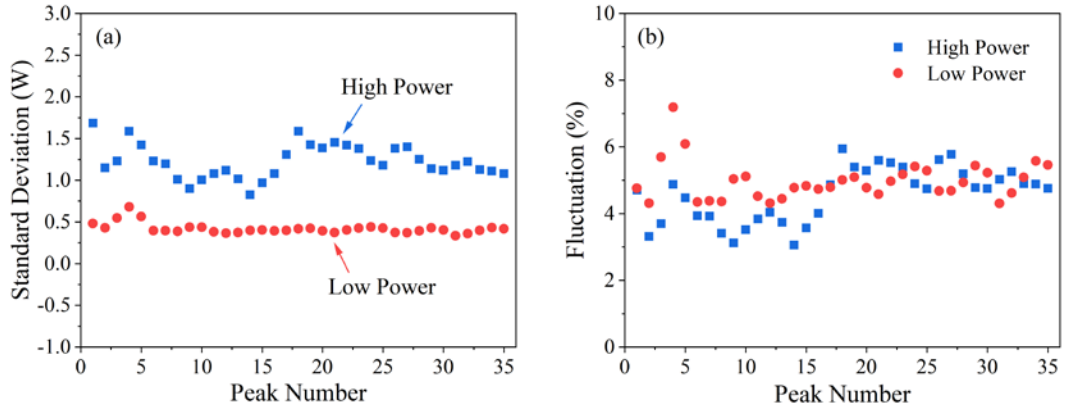


Figure 4.3: (a) Std and (b) fluctuation in pulse peak power of 100 bursts.

Mainly through SPM, these peak power-dependent profiles carry over to the phase profiles in Figure 4.4 (a). Figure 4.4 (b), shows the enlarged and shifted first and last pulse phase profiles within the burst. For the first peak, the phase difference within 1 ns (FWHM duration) was 1.2 rad for the high power and 0.4 rad for the low power, which correspond to only half of the pulse peak power and thus match the calculated *B*-integral of 2.4 rad and 0.8 rad, respectively. With a higher *B*-integral, there was a significant change in the shape of the high-power phase profile between the first and last pulse in Figure 4.4 (b). By contrast, the low-power phase profile remained nearly constant.

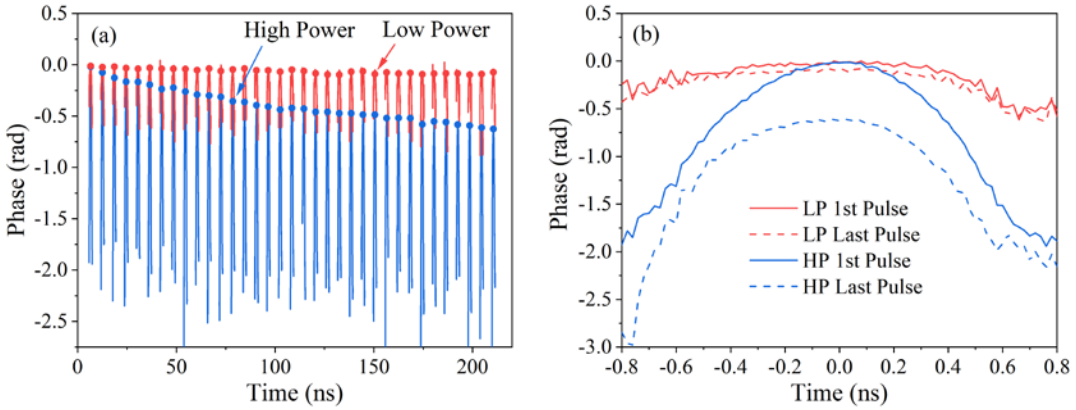


Figure 4.4: High and low power phase profiles for (a) bursts and (b) the first and last pulses. The curves are averaged over 100 bursts.

The burst-to-burst variations in the instantaneous phase of each pulse will affect the CPSA stacking efficiency. Figure 4.5 (a) shows the std of the relative phase for the last pulse, which is defined as the phase difference between the last and the first pulse within a burst. The std was below 0.3 rad for the high power and below 0.1 rad for the low power case. The std remained nearly constant within 1 ns range while was much larger in the edges of the pulses. A larger measurement error in the edges may be caused by noise, since the energy and instantaneous power are much smaller. Figure 4.5 (b) shows the std of the relative phase for each pulse throughout the burst. Whereas the average effects in Figure 4.2 and Figure 4.4 are possible to compensate for with amplitude and phase controllers, the fluctuations (std) in Figure 4.3 and Figure 4.5 are more difficult to handle. Still, even the 0.3 rad in our high-power case corresponds to only $\lambda/20$, which still have a 97% combination efficiency [24]. Nevertheless, for larger *B*-integrals, random fluctuations would become increasingly problematic.

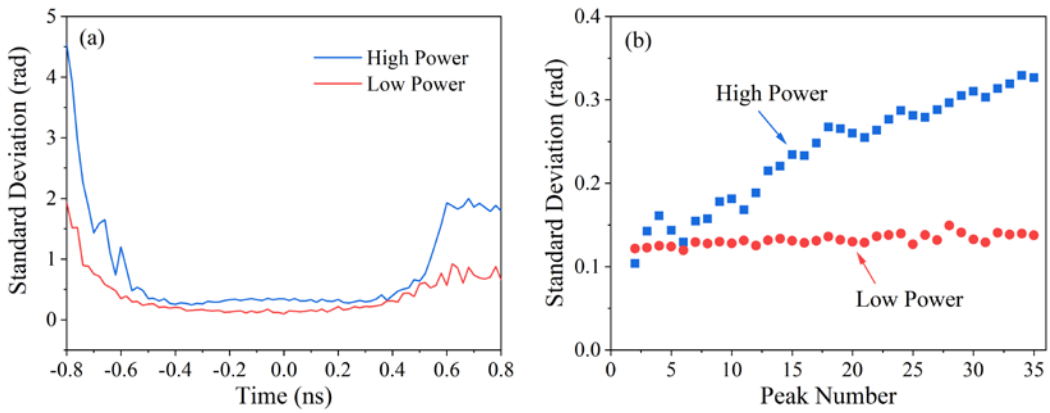


Figure 4.5: (a) Std of the relative phase for the last pulse within the burst and (b) std for each pulse in 100 bursts for relative phase in peak value at high and low power.

## 4.4 Single-shot amplitude and phase measurement and fluctuation analysis for cascaded fibre amplifiers

In the previous results, amplitude and phase characterizations of pulse bursts in a single fibre amplifier in relatively low nonlinear and slightly saturated regime were successfully achieved. In practice, systems with cascaded fibre amplifiers are more common cases for the ambition of obtaining higher extracted pulse energy. In other words, the pulse bursts would have higher peak power and thus suffer more significant nonlinearities and saturation. The phase measurement and retrieval of these systems are more interesting but also more challenging, since a valid and accurate measurement is restricted by the equipment bandwidth.

In this section, I demonstrated DPA in a YDFA chain in the regime of transform-limited seed pulses, formed by a single-frequency diode laser externally modulated to bursts of 35 1-ns Gaussian-like pulses (~0.44 GHz transform-limited bandwidth). I characterized the amplitude and phase at high extracted energy with a single-shot homodyne method, which I describe. Given a measurement bandwidth of ~12.5 GHz , this method can handle such pulses with $B$ ≤50 rad. The maximum extracted energy was 30.7 μJ (*vs.* 25 μJ saturation energy) and the maximum phase distortion was 21.2 rad. The $B$-integral difference between the burst's first and last pulse was then 12.8 rad. The burst-to-burst fluctuation of individual pulses was measured to <6% (std) in instantaneous power and 0.6 rad (std) in phase. This is still within suggested phase tolerances ($\lambda/10$) for stacking. I did not stack the amplified pulses, but note that 0.6 rad (std) phase fluctuations allow for 91% of maximum stacking efficiency.

### 4.4.1 Experimental setup and method

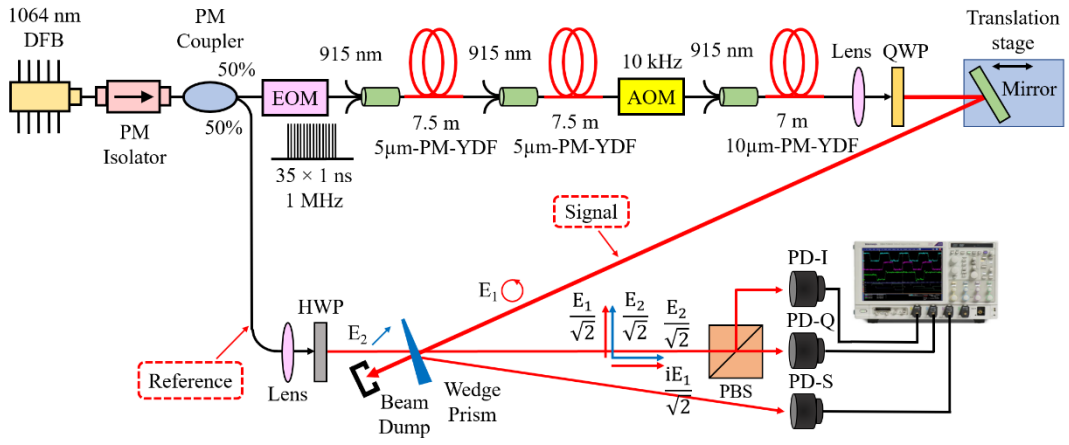


Figure 4.6: Schematic of the pulse-burst fibre amplifiers and measurement system. Pump diodes: JDSU 6397-L3 Series diode laser (915 nm), Pump diode drivers: Laser

Driver Inc. Model LDI-820 (1st amplifier), SDL-822 (2nd amplifier), TDK-Lambda, GEN40-38 (3rd amplifier).

Figure 4.6 shows the Yb-doped fibre DPA together with the measurement system and bears some similarities with the setup described in Section 4.3. The fibre amplifiers are the same, while the seed was replaced by a single-frequency CW DFB diode laser (II-VI CMDFB1064A) with <1 MHz linewidth. A same 90° optical hybrid phase measurement method was applied, except that half of the seed power was tapped off to serve as a CW reference. To obtain a pronounced interference signal between the amplified burst signal and the CW reference, the coherence length of the seed source should be at least as long as the path-length difference (i.e. ~40 m) of the two arms. Thus, a substituted diode laser with a linewidth of <1 MHz was used in this setup to meet this requirement. Besides, a valid interference signal can only be acquired when the amplitude level of two combined amplified burst signal and CW reference are comparable. It means that only a part of the amplified burst signal power will be used for measuement due to a limited power of CW reference. Furthermore, the separation of the pulses within the burst was adjusted to 10 ns for two reasons: first, to avoid the detrimental SBS, whose response time is governed by the acoustical phonon lifetime of ~10 ns. Second, to avoid any temporal overlap, so that no cross-phase modulation (XPM) coupling is observed at high *B*-integral. Amplified by two pre-ampflifiers, the output bursts from the AOM had energy of 0.13 μJ, temporal contrast of 36 dB, and ~1% (std) fluctuations in the peak power of the leading pulse. Finally, the bursts were amplified by a 10-μm-core YDFA comprising 7 m of Nufern PLMA-YDF-10/125-VIII.

The instantaneous power of the amplified burst signal $\mathrm{I}_1(\mathrm{t}) = |E_1(t)|^2$ and, following interference with the CW reference $\mathrm{I}_2 = |E_2|^2$, its in-phase $\mathrm{I}_I(\mathrm{t})$ and quadrature $\mathrm{I}_Q(\mathrm{t})$ homodyne signals were detected by biased photodiodes PD-I, PD-Q, and PD-S. Compared to the previous phase measuement setup, the first advantage is that no optical delay line is needed to synchronize the signal and reference beams. Another is for sure that a release of one detected signal further simplifies the measurement system. The details of the signals calibration and measuement will be discussed in Section 4.4.2. Equations (4.1) – (4.3) will still be used to retrieve the temporal phase, only with a substitution of $\mathrm{I}_2(\mathrm{t})$ into $\mathrm{I}_2$. The presented results are also based on data from 100 bursts acquired within 30 s which were averaged and used for fluctuation analysis. I did not evaluate errors directly, but our measurements suggest that our system can keep random errors within 0.2 rad in regions of adequate power. Besides, the measurement of fluctuation as low as 0.1 rad (std) have been successfully realized in Section 4.3. Simulations showed that the maximum *B*-integral for which the phase profile could be retrieved, with 12.5 GHz bandwidth and 1-ns Gaussian pulses, was ~50 rad under ideal

conditions. Noise, jitter and pulse irregularities may reduce this value.

### 4.4.2 Three-channel phase measurement software system

Retrieving the targeted temporal individual pulse phase within the bursts requires an accurate control of the output beams' polarisation, spatial overlap and power level detected by the photodiodes. It would be important and efficient to timely acquire the measured phase informations and evaluate their validity for each measurement. A remote communication was built between the oscilloscope and a PC via GPIB interface. Then through the MATLAB App Designer, a graphical user interface (GUI) combined with programmed behaviors was developed as a user-friendly three-channel phase measurement system. Therefore, for each measurement, the data can be acquired and analysed on the computer.

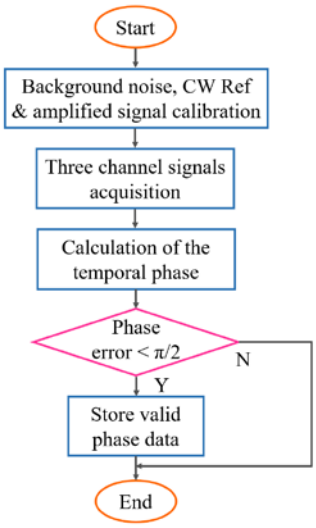


Figure 4.7: Flowchart for valid temporal phase measurement and retrieval.

The accomplishment of a valid phase measurement and retireval is shown in the flowchart in Figure 4.7. With an optical alignment optimized measurement system, firstly, the background noises of three detectors, CW reference and the amplified burst signal were seperately measured for initial calibration. Then the data of in-phase $I_I(t)$ and quadrature $I_Q(t)$ homodyne signals along with the amplified burst signal $I_S(t)$ were acquired and stored for phase retrieval. Next step, these stored data were automatically processed to obtain the corresponding phase data through a piece of algorithm code which is writen on the basis of equations (4.1) − (4.3). It is noted that an 'unwrap' function was executed to correct the radian phase angles when absolute jumps between consecutive elements of the data storage matrix are greater than or equal to the default jump tolerance of π radians. Then phase profiles were rebuilt according to a polynomial curve fitting of the retrieved phase data. Moreover, a valid phase profile was testified only when it has an error (between data and fitted curve) of less

than $\pi/2$ radians. Finally, these valid phase profiles of a burst will be stored for further analysis.

To realize the above functional flowchart, two blocks including system calibration and phase measurement were designed. Figure 4.8 shows the panel of the system calibration block. The process of fulfilling an accurate system calibration before executing a single-shot phase measurement can be presented as three steps. (a): Block both the amplified burst signal and the reference output beams, measure and save the background noise level. (b): Block the amplified burst signal output beam (main), measure and save the reference (CW) level. (c): Block the reference output beam (CW), measure and save the first-pulse centre position and width of the amplified burst signal hit on PD-S (CH3), and the time delay of signals on PD-I (CH1) and PD-Q (CH2) relative to CH3, as well as the signal amplitude ratios of CH1 *vs*. CH3 and CH2 *vs*. CH3. The calibration operation also confirms that the amplified signal as well as the measurement system is running properly. A lamp will indicate the working status for each calibraion step. A green illumination indicates a passed calibration while the calibration is failed with a red illumination. The 'finish lamp' would change to green only when all three calibration steps have been successfully finished.

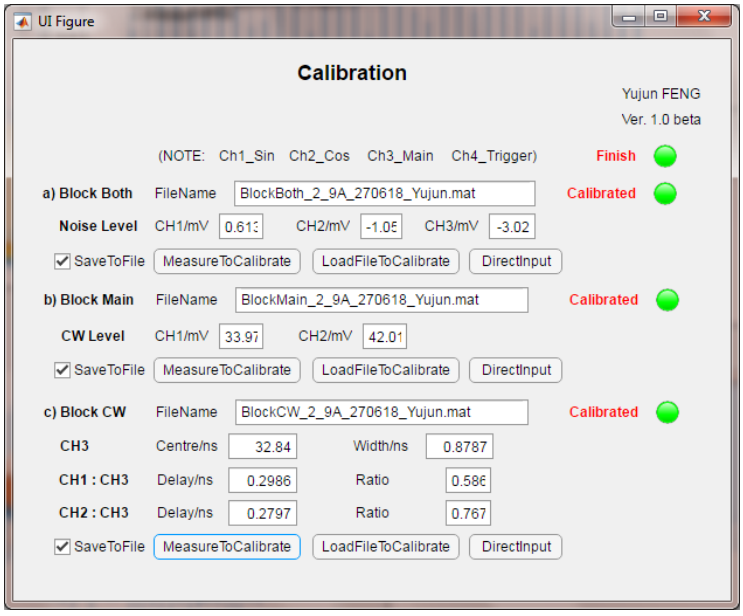


Figure 4.8: The panel of the system calibration block.

The panel of the phase measurement block is shown in Figure 4.9. The acquired burst number should be input ('Acquire No.' edit field) before executing the data acquisition. Two different data acquisitions (Normal & FastFrame) can be chosen for comparing the slow and fast burst-to-burst fluctuations. The 'Acquire' button executes the measurement while the 'reset' button can clear all the acquired data and make the system ready for the next measurement. An 'Auto Validation' check box can be ticked to automatically acquire valid data, whose phase errors satisfy the setting condition, as described before. It is also able to manually judge the validities

of the data and to choose the ‘Valid’ or ‘Invalid’ button. The number of valid burst for each acquisition can be shown in the ‘Validated Burst No.’ field. For each valid acquisition, the corresponding informations are graphically shown in four subplots. The phase profiles for individual pulses within the burst are shown in the last subplot. In particular, it is convenient to check the phase detail for a specific pulse through editing the ‘Peak No.’ value. Finally, all these valid phase data can be saved by clicking the ‘Save’ button.

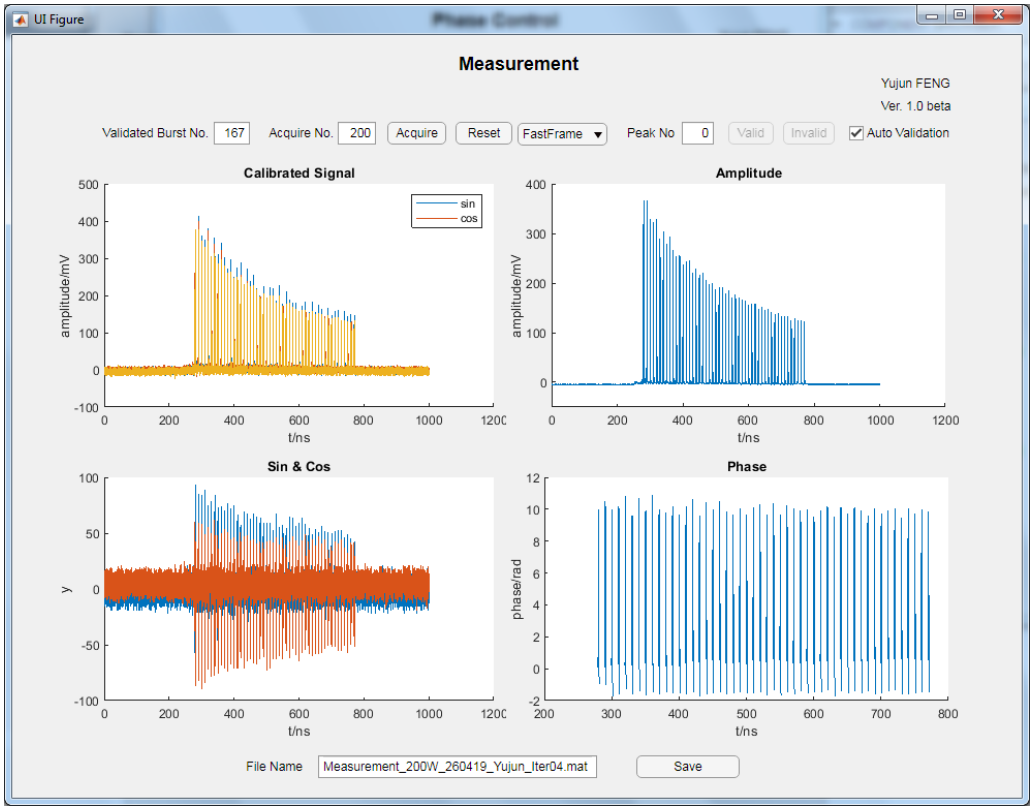


Figure 4.9: The panel of the phase measurement block.

### 4.4.3 Experimental results and analysis

The instantaneous power profiles are shown in Figure 4.10. Two different pump powers were adopted for the final YDFA, resulting in output burst energies of 11.5 μJ and 30.7 μJ, which can be compared to the saturation energy of 25 μJ calculated from the fibre parameters. In Figure 4.10 (a), both bursts show a characteristic quasi-exponential decay of the power envelope, caused by gain compression as energy is extracted from the amplifier. The first and last pulse within the bursts are shown in Figure 4.10 (b) with an enlarged and shifted time scale. Due to different amounts of gain saturation, the amplitudes of the first pulse were 2.85 and 1.67 times as high as for the last pulse for the HP and LP outputs, respectively. For comparison, the gain compression values expected from the extracted energy became 3.36 and 1.57, respectively.

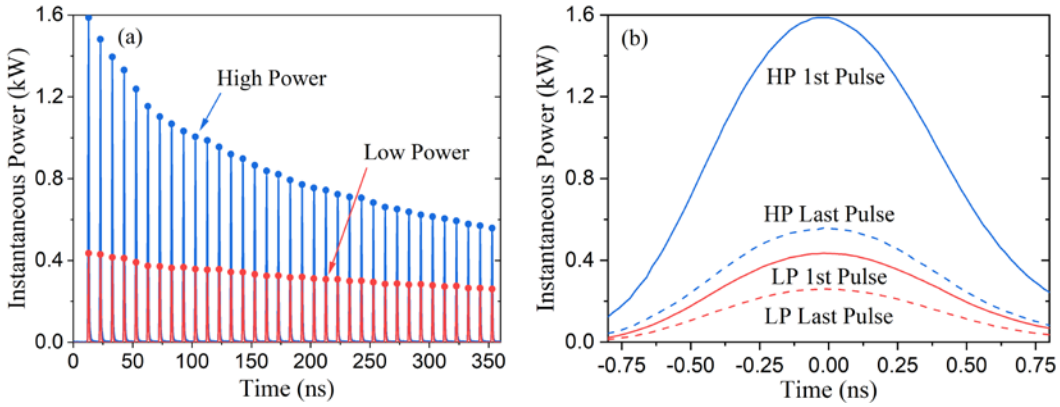


Figure 4.10: Instantaneous output power averaged over 100 bursts for high and low power (a) for the whole burst and (b) the first and last pulse.

The change in peak power within a burst can be problematic, but the seed can be pre-compensated to equalise the peak output power or the *B*-integral [25]. CPSA also works with varying pulse peak power within the burst [9, 26]. However, there are also fast burst-to-burst fluctuations in how the pulse amplitude evolves within a burst. These cannot be pre-compensated. Figure 4.11 shows the std and the corresponding fluctuation in the peak power of each of the 35 pulses, evaluated for 100 bursts. The std varied in a similar way as the peaks in Figure 4.10 (a), and was between 4.5% and 6% of the peaks in the LP case and between 3.5% and 4.5% of the peaks in the HP case. The std remained similar over the central 0.5 ns of the pulses and was considerably larger than the 1% (std) pulse peak fluctuation at the input to the final YDFA.

The energy gain grows exponentially with stored energy in the unsaturated regime, but approximately linearly when saturated. This may explain why the relative fluctuations were smaller at high power. A std in the instantaneous power of 6% degraded the stacking efficiency by 0.09% in case of 35 pulses. For more pulses the degradation was smaller [27].

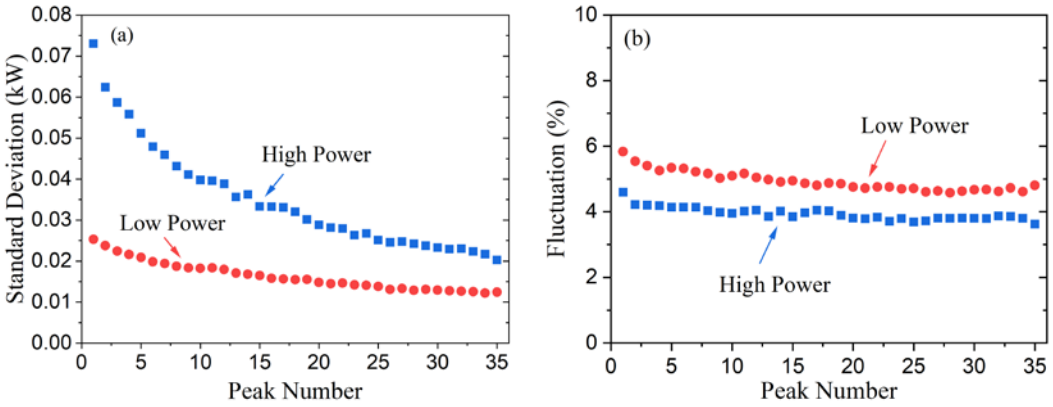


Figure 4.11: (a) Std and (b) fluctuation in pulse peak power calculated for 100 bursts for each of the 35 pulses.

There will also be variations in the phase, e.g., because of SPM, K-K and thermal effects. Figure 4.12 shows the instantaneous phase calculated according to Equation (4.3), for the whole burst and enlarged for the first and last pulses. Pulse stacking does not depend on the absolute phase, so I have added a constant to make the peak phase of the first pulse in the burst to 0 rad. The phase was then evaluated for the range of each pulse where the instantaneous power was large enough to yield meaningful results. Typically, this was over the central 1.6 ns. The phase varied over several waves, and was therefore unwrapped. The procedure was then repeated for the next pulse. Since the instantaneous phase is not available continuously between pulses, I adjusted the peak phase by integer factors of $2\pi$ to make the change from the previous peak the smallest possible. This was in all cases negative with magnitude <1 rad.

Within a pulse, Figure 4.12 (b) shows that for the first pulse, the phase varied by 10.6 rad (HP) and by 3.3 rad (LP) within the central 1 ns. The variations in the last pulse were only 4.4 rad and 2.2 rad. The difference in phase profile between the first and last pulse was in both cases much larger than the acceptable $\lambda/10$, so the instantaneous phase would have to be corrected across the pulses for efficient combination. The phase profiles were similar to the instantaneous-power profiles, which suggests that SPM dominates the phase distortion. This was also seen in simulations in Ref. [16]. The full variations in phase, if dominated by SPM, are expected to be approximately twice as large as the variations over the FWHM duration, since those only correspond to power variations from 50% to 100% of the peak power. Thus, for the whole pulse, the phase variations of the first pulse may reach 21.2 rad (HP) and 6.6 rad (LP). These values are approximately equal to the *B*-integral and are well within the estimated 50-rad limit. The first HP pulse had a maximum deviation of the instantaneous frequency of 4.3 GHz and a linewidth of 10 GHz (23 times the transform limit) as calculated from the measured phase $\varphi(t)$. According to calculations of the pulse evolution through the amplifiers. the peak power of the first pulse becomes 1.6 kW (0.4 kW) in the HP (LP) case, and the *B*-integral becomes 18.6 rad (4.4 rad) in the main amplifier and 20.8 rad (6.4 rad) in the whole amplifier chain. Thus, the measured phase differences are in fair agreement with the *B*-integral calculations. Besides, the ratios of the measured intra-pulse phase variations between the first and the last pulse were 2.5 (HP) and 1.5 (LP), which is also matched to the aforementioned ratios in peak power.

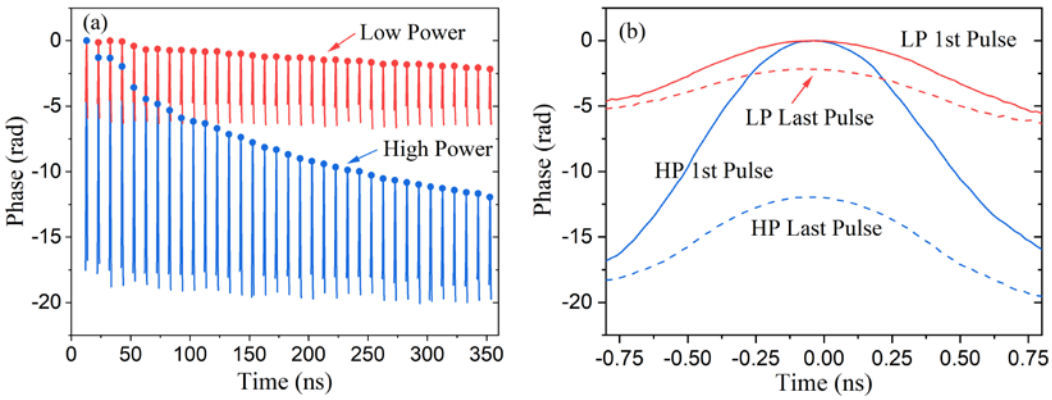


Figure 4.12: (a) High- and low-power phase profiles for (a) bursts and (b) the first and last pulses. The curves are averaged over 100 bursts.

However, the phase in the trailing edge of the pulses was smaller than that in the leading edge, by an amount of between 0.6 and 1.3 rad at 0.5 ns. This asymmetry may be caused by energy-related phase effects, which build up during the pulse [1]. In contrast to these experiments, the simulations in [16] showed larger phase in the trailing edge than in the leading edge. This suggests that the refractive index decreases through the combined effect of energy extraction from the Yb-ions and heat deposition. There is also a suggestion that the asymmetry is stronger towards the end of the burst, which indicates that the time constant for at least a part of this energy-dependent phase effect is slower than the pulse separation of 10 ns. The phase asymmetry of 1.3 rad may already be significant, and is furthermore expected to increase for higher extracted energy per pulse. Note also that in contrast to SPM, this phase distortion is not expected to become smaller in shorter fibres.

CPSA requires that burst-to-burst variations in the instantaneous phase are similar for each pulses (simplest is that they are small). Figure 4.13 (a) shows the std of the relative phase for the last pulse, which is defined as the phase difference between the last and the first pulse within a burst. The std was below 0.6 rad (HP) and (0.3 rad) (LP) at the peaks at 0 ns, and nearly constant over the central 1 ns of the pulses. The std was larger in the pulse edges, but there, the energy and instantaneous power were small, and there may well be larger measurement errors caused by noise. The same analysis of the instantaneous phase of the central parts of other pulses, relative to that of the first pulse, gave similar std-values, as shown in Figure 4.13 (b). The std appeared to increase towards higher pulse numbers, but the trend was not clear. Whereas the average effects in Figure 4.10 (a) and Figure 4.12 (a) are possible to compensate for with amplitude and phase controllers, the fluctuations (std) in Figure 4.11 and Figure 4.13 are more difficult to handle. However, the 0.6 rad (std) of fluctuation still allows for 91% of stacking efficiency.

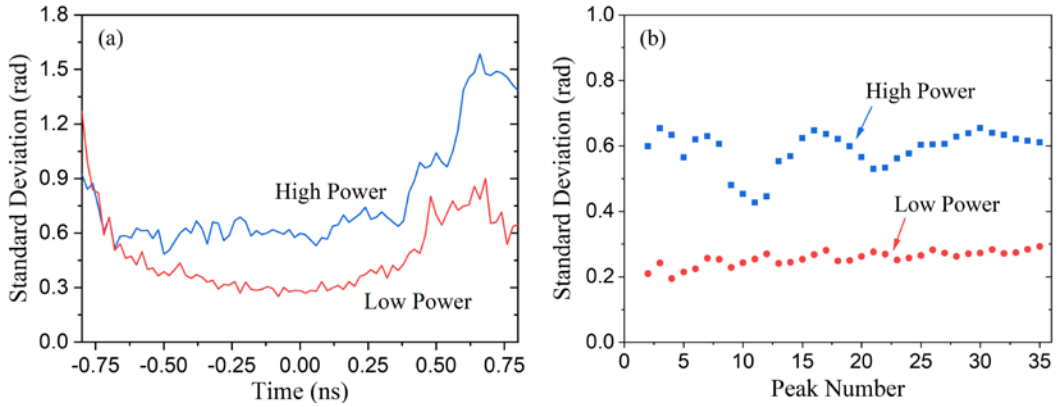


Figure 4.13: Std of the instantaneous phase of (a) the last pulse and (b) other pulses within the burst relative to that of the first pulse at high and low power.

## 4.5 Conclusion

I have demonstrated single-shot high-speed phase measurements of spectrally narrow pulses. The maximum phase distortion reached 21.2 rad in a burst of 35 1-ns Gaussian-like pulses at 1063 nm from an Yb-doped fibre amplifier chain through mixing with a continuous-wave reference. In this highly nonlinear saturated regime, the differences in phase profile between pulses within a burst were so large that the intra-pulse phase profile needs to be corrected if the pulses are to be temporally recombined (stacked) into a single pulse. In addition, 6% (std) amplitude fluctuation and 0.6 rad (std) (i.e., $\lambda/10$) phase fluctuation between bursts were also diagnosed. The fluctuations arise primarily in the final YDFA. They cannot be corrected, but are not so large that they preclude efficient pulse stacking. Simulations showed that with the used pulse shape and duration, a measurement bandwidth of ~12.5 GHz allows for *B*-integral up to ~50 rad, which exceeds the value expected in CPSA systems. It is noted that these results are also relevant for chirped- and divided-pulse amplification (CDPA) systems for fs pulses. These can also be directly characterized with a similar approach by the use of a chirped-pulse reference pathlength-matched to within 1 mm to avoid excessive beat frequencies.

## References

[1]. J. Limpert, F. Roser, D. N. Schimpf, E. Seise, T. Eidam, S. Hädrich, J. Rothhardt, C. J. Misas, and A. Tünnermann, “High Repetition Rate Gigawatt Peak Power Fiber Laser Systems: Challenges, Design, and Experiment”, IEEE J. Sel. Top. Quantum Electron. **15**, 159 (2009).

[2]. E. Seise, A. Klenke, J. Limpert, and A. Tünnerman, “Coherent addition of fiber-amplified ultrashort laser pulses”, Opt. Express **18**, 27827 (2010).

[3]. T. Zhou, T. Sano, and R. Wilcox, “Coherent combination of ultrashort pulse beams using two diffractive optics”, Opt. Lett. **42**, 4422 (2017).

[4]. S. Zhou, F. W. Wise, and D. G. Ouzounov, “Divided-pulse amplification of ultrashort pulses”, Opt. Lett. **32**, 87 (2007).

[5]. M. Kienel, M. Müller, A. Klenke, J. Limpert, and A. Tünnermann, “12 mJ and 1 kW Ultrafast Fiber-Laser System using Spatial and Temporal Coherent Pulse Addition”, in Advanced Solid State Lasers (Optical Society of America, 2016), paper AM4A.3.

[6]. L. Daniault, M. Hanna, D. N. Papadopoulos, Y. Zaouter, E. Mottay, F. Druon, and P. Georges, “Passive coherent beam combining of two femtosecond fiber chirped-pulse amplifiers”, Opt. Lett. **36**, 4023 (2011).

[7]. M. Kienel, A. Klenke, T. Eidam, S. Hädrich, J. Limpert, and A. Tünnermann, “Energy scaling of femtosecond amplifiers using actively controlled divided-pulse amplification”, Opt. Lett. **39**, 1049 (2014).

[8]. H. Stark, M. Müller, M. Kienel, A. Klenke, J. Limpert, and A. Tünnermann, “Electro-optically controlled divided-pulse amplification”, Opt. Express **25**, 13494 (2017).

[9]. T. Zhou, J. Ruppe, C. Zhu, I. Hu, J. Nees, and A. Galvanauskas, “Coherent pulse stacking amplification using low-finesse Gires-Tournois interferometers”, Opt. Express **23**, 7442 (2015).

[10]. F. Guichard, Y. Zaouter, M. Hanna, K. Mai, F. Morin, C. Hönninger, E. Mottay, and P. Georges, “High-energy chirped- and divided-pulse Sagnac femtosecond fiber amplifier”, Opt. Lett. **40**, 89 (2015).

[11]. M. Kienel, A. Klenke, T. Eidam, M. Baumgartl, C. Jauregui, J. Limpert, and A. Tünnermann, “Analysis of passively combined divided-pulse amplification as an energy-scaling concept”, Opt. Express **21**, 29031 (2013).

[12]. A. Klenke, E. Seise, J. Limpert, and A. Tünnermann, “Basic considerations on coherent combining of ultrashort laser pulses”, Opt. Express **19**, 25379 (2011).

[13]. F. Guichard, L. Lavenu, M. Hanna, Y. Zaouter, and P. Georges, “Coherent combining efficiency in strongly saturated divided-pulse amplification systems”, Opt. Express **24**, 25329 (2016).

[14]. Y. Feng, B. M. Zhang, and J. Nilsson, “Photodarkening-induced phase distortions and their

effects in single-channel and coherently combined Yb-doped fiber chirped pulse amplification systems", J. Lightwave Technol. **36**, 5521 (2018).

[15]. S. Palese, E. Cheung, G. Goodno, C. Shih, F. D. Teodoro, T. McComb, and M. Weber, "Coherent combining of pulsed fiber amplifiers in the nonlinear chirp regime with intra-pulse phase control", Opt. Express **20**, 7422 (2012).

[16]. Y. Feng, H. Lin, and J. Nilsson, "Single-shot phase measurement and fluctuation analysis of Yb-doped fiber amplifier for nanosecond pulses", in Conference on Lasers and Electro-Optics (Optical Society of America, 2018), paper SM2K.7.

[17]. C. Dorrer, "Interferometric Techniques for the Characterization of Temporal Modulators", IEEE Photon. Technol. Lett. **17**, 2688 (2005).

[18]. Y. Feng, B. M. Zhang, A. Harish, and J. Nilsson, "Thermally Induced Distortions of the Temporal Phase Of Optical Pulses In Phosphorous-doped Silica Fibers", in Advanced Solid State Lasers (Optical Society of America, 2015), paper AM5A.19.

[19]. W. R. Leeb, "Realization of 90° and 180° hybrids for optical frequencies", Electron. and Commun. **37**, 203 (1983).

[20]. L. G. Kazovsky, L. Curtis, W. C. Young, and N. K. Cheung, "All-fiber 90 optical hybrid for coherent communications", Appl. Opt. **26**, 437 (1987).

[21]. R. Garreis, "90° optical hybrid for coherent receivers", in Proceedings of SPIE 1522, Optical Space Communication II 1991, paper 210.

[22]. Z. Wang, L. Zhang, S. Wang, N. Xue, F. Peng, M. Fan, W. Sun, X. Qian, J. Rao, and Y. Rao, "Coherent Φ-OTDR based on I/Q demodulation and homodyne detection", Opt. Express **24**, 853 (2016).

[23]. L. G. Kazovsky, L. Curtis, W. C. Young, and N. K. Cheung, "All-fiber 90° optical hybrid for coherent communications", Appl. Opt. **26**, 437 (1987).

[24]. A. Brignon, "Coherent Laser Beam Combining", Germany: Wiley, 2013.

[25]. J. Ruppe, S. Chen, M. Sheikhsofla, R. Wilcox, J. Nees, and A. Galvanauskas, "Multiplexed Coherent Pulse Stacking of 27 Pulses in a 4+1 GTI Resonator Sequence", in Advanced Solid State Lasers (Optical Society of America, 2016), paper AM4A.6.

[26]. I. Astrauskas, E. Kaksis, T. Flöry, G. Andriukaitis, A. Pugžlys, A. Baltuška, J. Ruppe, S. Chen, A. Galvanauskas, and T. Balčiūnas, "High-energy pulse stacking via regenerative pulse-burst amplification", Opt. Lett. **42**, 2201 (2017).

[27]. G. D. Goodno, C. Shih, and J. E. Rothenberg, "Perturbative analysis of coherent combining efficiency with mismatched lasers", Opt. Express **18**, 25403 (2010).

# Chapter 5
# Active instantaneous-phase equalisation and amplitude control of pulse-bursts in a narrow-linewidth divided-pulse Yb-doped fibre amplification system

## 5.1 Overview

From the work described in Chapter 4, I have established an effective way to precisely retrieve the temporal phase and analyse the fluctuation of the ns-scale pulse-bursts. On that basis, in this chapter, I aim to optimize the coherent combining efficiency when pulses within the burst are temporally stacked, through actively controlling the pulse amplitudes and instantaneous-phases to compensate the relevant distortions. Here, an employment of fast amplitude and phase EOMs which are controlled via a phase optimization algorithm were utilized to realize an efficient output. Section 5.2 briefly introduces the research results and necessity to actively control the phase distortions between pulse-burst for an efficient combination. In Section 5.3, static numerical simulations were established to explore the influence of different effects on the coherent combining efficiency. Then the practical experimental setup and designed software system are described in Section 5.4. Section 5.5 shows the results in the optimization process of equalising the instantaneous-phase and controlling the amplitude. Finally, the achievement is summarized in Section 5.6.

## 5.2 Introduction

Generally, the primary limitations for extracting energy from fibre amplifiers in pulses of ns-scale duration are nonlinearities and fibre facet damage. In mitigation, divided-pulse amplification (DPA) followed by CPS has been proposed to extend the effective pulse duration and reduce the pulse peak power [1]. Although DPA-CPS systems with dozens of sub-pulses have been demonstrated to work well with low-nonlinearity pulses (a *B*-integral of ~π), this requires scaling to around 100 sub-pulses to extract the bulk of the energy available in the gain fibre [2]. This poses major practical issues. For instance, an excessive burst duration degrades the stability of the stacking cavity, and the complexity of stacking cavities and their control increases with the number of sub-pulses [2]. This suggests the use of fewer sub-pulses with higher energy, which however increases the nonlinearity and induced phase distortions [3],

and is complicated by gain-saturation-induced sub-pulse reshaping and variations in the effective length [3] when the extracted energy is comparable to, or larger than, the saturation energy.

Researchers have widely investigated physical effects that limit the combining efficiency in highly nonlinear and strongly saturated DPA systems. Degradations can be induced by nonlinear interactions between sub-pulses if they are not sufficiently separated in time domain [4]. Input slight intensity difference among sub-pulses will be turned into phase shifts through SPM and thus degrades the efficiency [5]. However, the dominating effect would be saturation-induced gain difference between the sub-pulses in strongly saturated regime [6, 7]. It has been studied with a simple yet insightful analytical model in [7], in the context of passive DPA systems. Further, in another numerical study [3], Kramers-Kronig-relevant phase shifts, intra-pulse temporal and spectral reshaping effects due to gain saturation were also considered.

In this chapter, I demonstrated narrow-linewidth DPA of bursts of 50 pulses in Yb-doped fibre amplifiers working in the high-nonlinearity (*B*-integral >10 rad) energy-saturated region (1.15-mJ extracted *vs.* 0.7-mJ saturation energy). Using fast EOMs for amplitude and phase, I precisely controlled both the pulse peak amplitude and the intra-pulse instantaneous phase throughout the burst to reach a calculated 90% coherent pulse stacking efficiency.

## 5.3 Influence analysis of amplitude- and phase-difference, and fluctuation on combining process

As discussed before, in strongly saturated and highly nonlinear DPA-CPS systems, active amplitude and phase controls are essential for achieving an efficient pulse stacking. Here, I studied the influence of amplitude-difference, phase-difference, and amplitude fluctuation on the combining process. A static numerical analysis was carried out based on parameters of the established DPA-CPS system. To simplify the calculation, only one amplifier was considered in the simulation model, which can still provide qualitative suggestions on designing my scheme. Throughout the simulation, numerical values for the parameters were set based on the non-PM low-NA LMA Yb-doped fibre (DB01216) as follows: the saturation energy is $E_{sat}$ = 0.7 mJ, the small signal absorption is $g_0$ = 4 dB/m, the nonlinear parameter is $\gamma = 6\times10^{-5}$ $m^{-1}$ $W^{-1}$ and the fibre length is 5 m. Besides, the lasing wavelength is 1064 nm and all the instantaneous-power and temporal phase profiles are assumed to be identically Gaussian-shaped.

The gain saturation effect in the amplifier was analysed according to the Frantz-Nodvik-

Equations. The relationship between the time-dependent output intensity profile of the pulse and the input pulse intensity profile is described by Equation (3.1) and (3.2). Then the *B*-integral can be estimated through the Equation (2.10). Finally, based on the acquired data of temporal sub-pulse intensity and phase, the combining efficiency can be calculated by Equations (4.4) and (4.5).

### 5.3.1 Influence of *B*-integral difference on combining process

It is noted that initial amplitude fluctuation among the input pulse-bursts was not considered in simulation results of Section 5.3.1 and Section 5.3.2. In this section, I investigated the case that the output pulse amplitudes are equalised, which can be done by an amplitude pre-compensation of the input pulse-bursts. In this case, the accumulated nonlinear phase shifts (*B*-integral) in the trailing pulses are greater than that in the leading pulses. Thus, the influence of *B*-integral difference between pulses on the combining efficiency can be clearly revealed. Firstly, the input burst energy was set as a 0.1-time saturation energy (0.1-$E_{sat}$) and the number of pulses was 50. Figure 5.1 (a) shows the calculated results on the combining efficiency of 50 pulses as a function of the *B*-integral (maximum value). The different curves correspond to output with different energies/amplifier gains. An output burst energy normalized to 4.5-time the saturation energy corresponds to a ~30 dB gain, which is a maximum achievable gain in a typical amplifier. The results clearly illustrated that the combining efficiency degrades with increasing *B*-integral. Specifically, at low-energy output (0.5-$E_{sat}$), the combining efficiency dropped moderately to 86% with a 10-rad *B*-integral, while only 18% for the high-energy output (4.5-$E_{sat}$). In the high-energy output case, a larger accumulated nonlinear phase difference between pulses further reduced the combining efficiency. Besides, in the 4-$E_{sat}$ and 4.5-$E_{sat}$ output results, the degradation of combining efficiency became 'saturated' and maintained at ~18% since the phase difference is getting more comparable to the *B*-integral. When a higher input burst energy 0.5-$E_{sat}$ was set, the corresponding calculation results are shown in Figure 5.1 (b). I found that the dependency of combining efficiency on the *B*-integral remained the same, which means that the combining efficiency is independent of the input burst energy. These results well agree that the phase difference between pulses has a significant impact on the combining efficiency. To achieve 90% combining efficiency with 50 combined pulses, the maximum *B*-integral should be less than 4 rad under only 1-$E_{sat}$ output. Therefore, this approach via equalising the output pulse amplitude cannot ensure an efficient combination in highly nonlinear and saturated regimes.

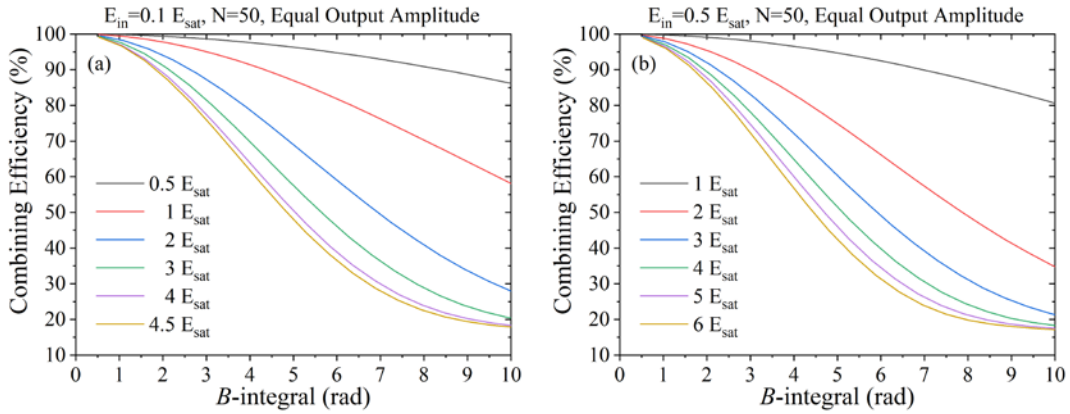


Figure 5.1: Dependency of the combining efficiency on the value of the *B*-integral with (a) 0.1-$E_{sat}$ and (b) 0.5-$E_{sat}$ input pulse energies, in the case that the output pulse amplitudes are equal (50 pulses), if no fluctuation of the input pulse amplitudes is introduced.

### 5.3.2 Influence of amplitude difference on combining process

Similarly, through pre-compensating the amplitude of input pulse-bursts, an output burst with equal *B*-integrals among pulses can also be realized. Then the influence of amplitude difference on combining efficiency can be investigated. With an initial input of 0.1-$E_{sat}$ burst energy and 50 pulses within a burst, the calculation results on the combining efficiency of 50 pulses as a function of the pulse *B*-integral are shown in Figure 5.2 (a). The results clearly revealed that the combining efficiency drops with increasing output burst energy, while >95% can still be maintained with a low *B*-integral output in the highly saturated regime (4.5-$E_{sat}$). The combining efficiency degradation can be attributed to the amplitude difference between pulses. Compared to the *B*-integral difference, the influence on combining efficiency caused by the amplitude difference is negligible. Meanwhile, at <2-$E_{sat}$ burst energy output, the combining efficiency remained nearly constant with increasing *B*-integral even up to 50 rad. However, with increasing output burst energy, the degradation of combining efficiency on the increase of *B*-integral is getting increasingly rapid. The combining efficiency degraded from 95.8% to 93.5% when the output burst energy reaches 4.5-$E_{sat}$. I attributed this rapid degradation to the intra-saturation-induced phase distortion. Besides, the calculation results in terms of a higher input burst energy (0.5-$E_{sat}$) are shown in Figure 5.2 (b). The variation trend of combining efficiency on the *B*-integral is unchanged. To maintain a 30-dB amplifier gain, the output burst energy reached 6.5-$E_{sat}$. In this strongly saturated regime, the combining efficiency dropped dramatically down to ~85% when reaching a 50-rad *B*-integral. This agrees with that the intra-pulse saturation effect is becoming increasingly significant when operating in a stronger saturated regime. Furthermore, it should be noted that a higher input burst energy

is beneficial to achieve a more efficient combination for a specific output burst energy.

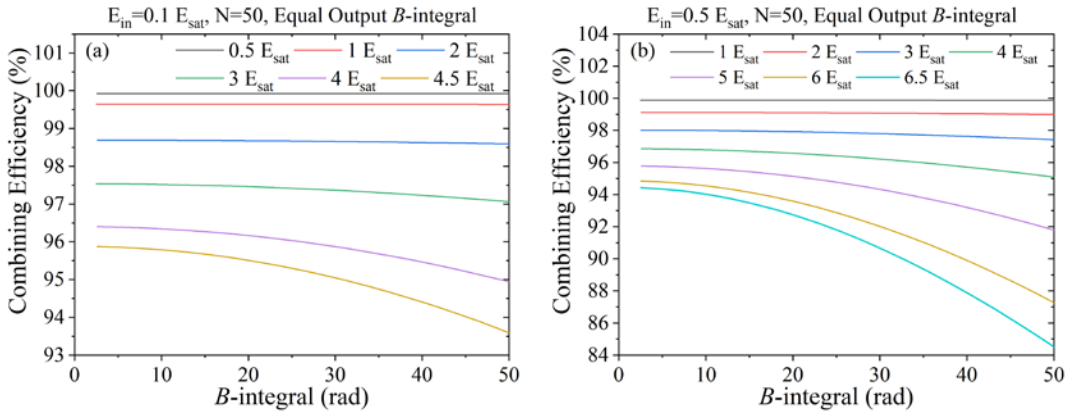


Figure 5.2: Dependency of the combining efficiency on the value of the *B*-integral, with (a) 0.1-$E_{sat}$ and (b) 0.5-$E_{sat}$ input pulse energies, in the case that the output pulse *B*-integrals are equal (50 pulses), if no fluctuation of the input pulse amplitudes is introduced.

Moreover, I have also investigated the influence coming from the setting input pulse number. Herein, the input pulse number was doubled to 100 while the burst energy remained 0.1-$E_{sat}$. In other words, the input individual pulse energy is only half of the setting used for achieving results in Figure 5.2 (a). The relevant calculation results are depicted in Figure 5.3 (a). Compared to results shown in Figure 5.2 (a), the combining efficiency is hardly changed at different output burst energies when the *B*-integral is small, due to an unchanged ratio between amplitude difference and output amplitude. However, with a same amplifier gain output, the corresponding output individual pulse energy also reduced to a half. Therefore, the effect of intra-pulse gain saturation becomes less effective. This was confirmed by a slower decline of the combining efficiency with increasing *B*-integral at higher burst energy outputs. At 4.5-$E_{sat}$ output with a 50-rad *B*-integral, the combining efficiency improved from 93.5% to 95.3%. At the same time, the calculation results in terms of a 0.5-$E_{sat}$ input burst energy and 100 pulses are shown in Figure 5.3 (b). Due to a weak intra-pulse phase distortion, the combining efficiency enhanced to ~92% at a 50-rad *B*-integral and 30-dB amplifier gain.

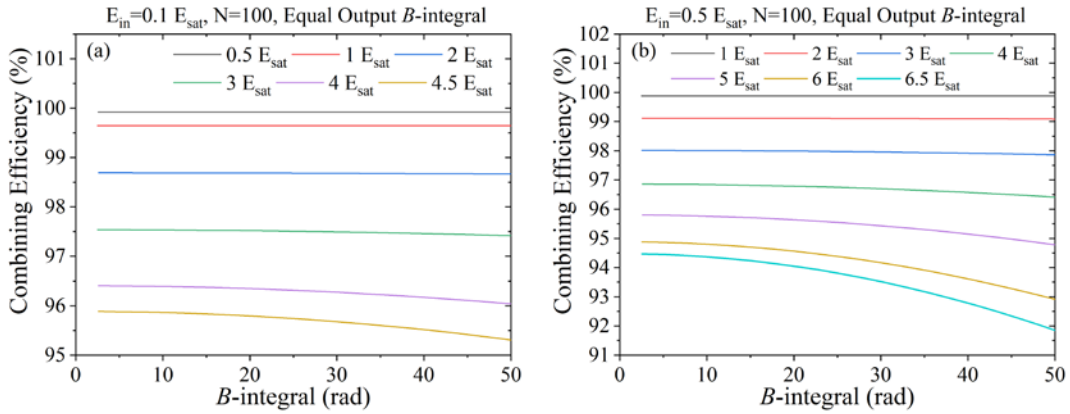


Figure 5.3: Dependency of the combining efficiency on the value of the *B*-integral, with (a) 0.1-$E_{sat}$ and (b) 0.5-$E_{sat}$ input pulse energies, in the case that the output pulse *B*-integrals are equal (100 pulses), if no fluctuation of the input pulse amplitudes is introduced.

### 5.3.3 Influence of input pulse amplitude fluctuation on combining process

According to the above calculation results, it can be known that the amplitude difference between pulses contributes negligible effect on the combining efficiency. However, it is of great interest to investigate the influence induced by the input pulse amplitude fluctuation. In this section, I have done some numerical simulations to reveal its contribution. Firstly, a 1% of amplitude fluctuation was introduced within the input pulses and the relevant calculation results are shown in Figure 5.4 (a)-(d). Figure 5.4 (a) shows that the combining efficiency remained almost the same with low *B*-integral, e.g., ~95% *vs*. ~96% (without amplitude fluctuation) at 4.5-$E_{sat}$ output. However, the combining efficiency dropped dramatically with the increase of *B*-integral. With a 50-rad *B*-integral, the combining efficiency of a 4.5-$E_{sat}$ output burst was down to ~82%, while a ~93% for the counterpart without an input fluctuation. It can be explained that these small portions of amplitude fluctuation are turned into large phase shifts, particularly in highly nonlinear regimes. Consequently, these induced larger *B*-integral differences between pulses would significantly degrade the combining efficiency. It can also be confirmed from other results with different input burst energies and pulse numbers while with a same 1% amplitude fluctuation. Totally, in terms of all cases, the combining efficiency declines increasingly quickly with the increase of *B*-integral. When the burst was amplified by 30-dB and operated with a 50-rad *B*-integral, the achieved combining efficiencies were ~74% ($E_{in}$=0.5-$E_{sat}$, N=50), ~83% ($E_{in}$=0.1-$E_{sat}$, N=100) and ~80% ($E_{in}$=0.5-$E_{sat}$, N=100), respectively.

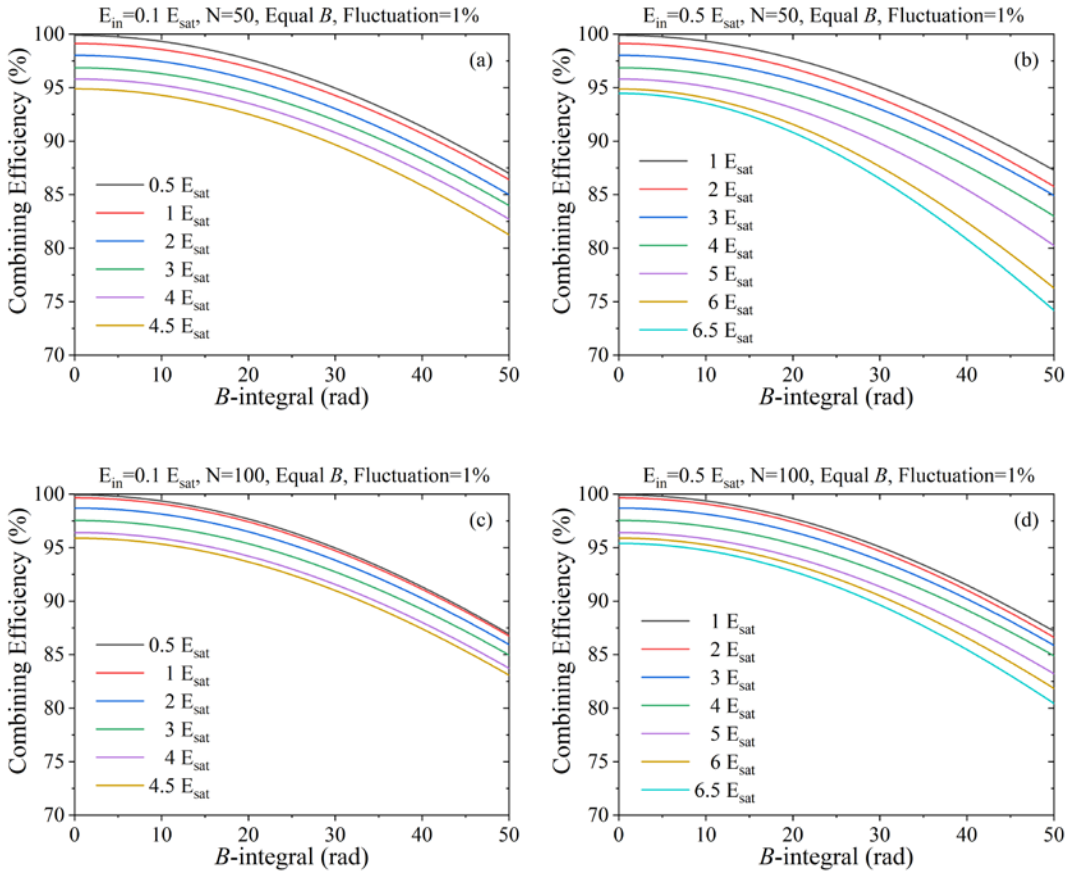


Figure 5.4: Dependency of the combining efficiency on the value of the *B*-integral, with input pulse energy and pulse number of (a) 0.1-$E_{sat}$ and 50, (b) 0.1-$E_{sat}$ and 100, (c) 0.5-$E_{sat}$ and 50, (d) 0.5-$E_{sat}$ and 100, respectively, in the case that the output pulse *B*-integrals are equal and 1% fluctuation of the input pulse amplitudes is introduced.

Regarding to input bursts with 3% amplitude fluctuation, the calculation results in terms of 50 pulses case are shown in Figure 5.5 (a). The combining efficiency dramatically reduced to ~36% at 50-rad *B*-integral and 4.5-$E_{sat}$ burst energy. In order to achieve >80% combining efficiency, the *B*-integral should be less than 20-rad. In comparison, in the case with a 5% amplitude fluctuation, a worse decline occurred as shown in Figure 5.5 (b). The combining efficiency dropped to less than 20% as the *B*-integral reaches 50-rad. Only working in a much lower nonlinear regime can a high combining efficiency be achieved. Based on these results, it is concluded that an efficient combination in the high *B*-integral regime requires a stable input burst.

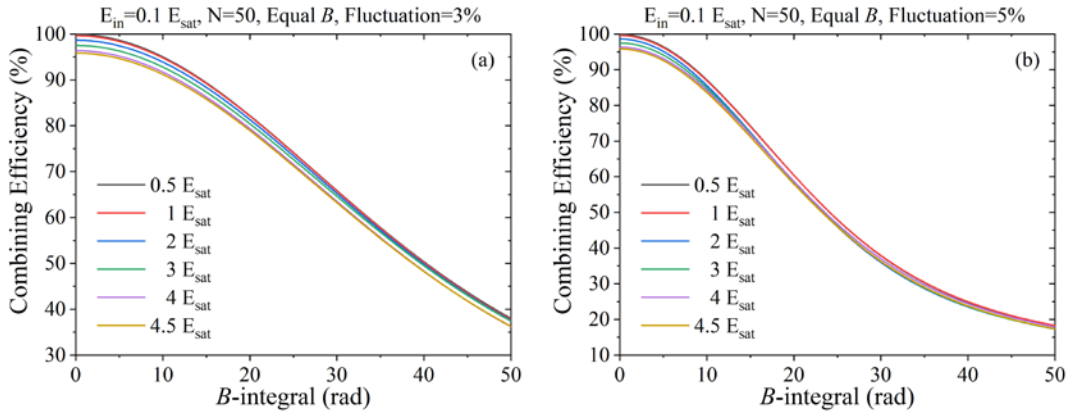


Figure 5.5: Dependency of the combining efficiency on the value of the *B*-integral, with input pulse energy, pulse number and input amplitude fluctuation of (a) 0.1-$E_{sat}$, 50 and 3% (b) 0.1-$E_{sat}$, 50 and 5%, respectively, in the case that the output pulse *B*-integrals are equal.

From these numerical simulation results and analysis, I can confirm that equalising the *B*-integral difference between pulses combined with an appropriate amplitude control would be an effective route towards a higher combining efficiency. These inter-pulse amplitude and phase differences can be effectively compensated for by fast EOAMs. Besides, the results also show that the intra-pulse phase distortions will occur when operating in the highly nonlinear regime. In practice, the well-known phase effects related to K-K-relation and photodarkening which I do not consider would cause an intra-phase distortion as well [8, 9]. The compensation of these intra-phase distortions will rely on the assistance of fast EOPMs. Furthermore, the increasing of pulse number will not only weaken the intra-pulse phase distortions to some extent, but also complicate the combining system with a higher stability requirement. Thus, it is a trade-off for a designer to choose an appropriate pulse number according to the practical requirements. Last but not at least, a stable input pulse-burst is a precondition for achieving an efficient combination in the highly nonlinear regime.

## 5.4 Experimental setup and software designed blocks

### 5.4.1 Experimental setup and control procedures

Based on the analysis of numerical simulation results, I introduced fast EOMs for amplitude and phase to precisely control both the pulse peak amplitude and the intra-pulse instantaneous phase throughout the burst aiming for an efficient combination. The narrow-linewidth pulse-burst fibre amplifiers combined with the amplitude and phase measurement system illustrated in Figure 5.6 have been described in the previous sections. A difference is that a lower output burst energy (1.15-mJ) was used in the investigation of this chapter. Here, I will mainly

introduce the fulfillment of the control system. The inter-phase adjustment was realized through an amplitude controlling of the existing EOAM. A followed EOPM (Photonline, PM-0S5-20-PFU-PFU-106, 20 GHz/s sampling rate, 2.5-V half-wave voltage) was used to control the intra-phase within sub-pulses. It was also driven by the AWG (Tektronix AWG7122B, 12 GS/s sampling rate, 10-bits vertical resolution) followed a RF amplifier (ZX60-14012L, 300 kHz to 14 GHz bandwidth). The AWG has a maximum amplitude of 1 $V_{p-p}$ with a 3.5 GHz analog bandwidth. Limited by this maximum amplitude setting and low gain of the RF amplifier, the maximum achievable $V_{p-p}$ from the RF amplifier was ~2.6 V, which means a ~π-rad maximum phase change can be realized.

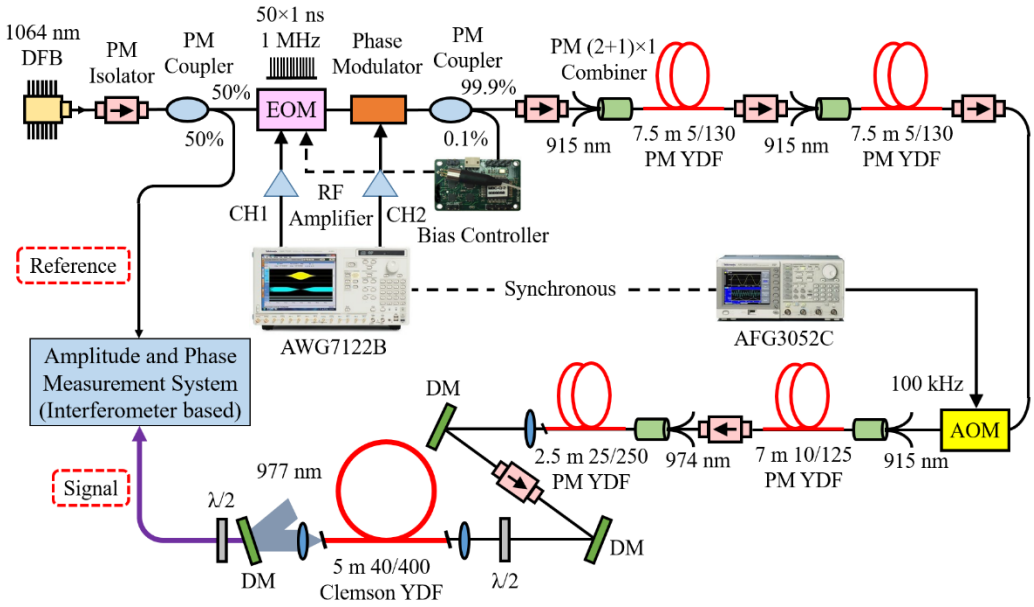


Figure 5.6: Schematic of the narrow-linewidth pulse-burst fibre amplifiers combined with the amplitude and phase measurement and control system.

The technical route of amplitude and phase measurement and control were carried out in following procedures. Firstly, I measured the amplitude and phase (through homodyning) of bursts without any compensations. Secondly, I used the EOAM to adjust the amplitude of individual pulses within the burst to minimize the inter-phase difference (*B*-integral difference) among pulses within a burst. This also reduces the amplitude variations. Then, based on subsequently measured amplitude and phase data, the intra-pulse instantaneous-phase profiles was equalised between the pulses by the EOPM. Finally, the measured amplitude and phase results were utilized for the pulse stacking analysis. It is noted that the pulse combining efficiency is strongly influenced by the difference in instantaneous phase between pulses while the impact of amplitude differences is much smaller. This makes bursts with a small difference in instantaneous phase between pulses our primary aim, while I ignore variations in the pulse envelope.

In principle, there is another technical route that may go towards to the same achievement. That is to firstly control the EOAM to achieve an output pulse-burst with equalised amplitude and then compensate the phase differences between pulses through the EOPM. However, a much higher RF signal applied on the EOPM will be required for adjusting a much larger phase difference induced by the gain saturation.

### 5.4.2 Software block design and function structure

The functions of calibration and phase measurement blocks have been introduced in Section 4.4.2. In this section, the phase (including the inter-pulse and intra-pulse) control designed blocks and their relevant functions will be introduced. Figure 5.7 shows the panel of the phase control block. First, there are two options (‘inter’ and ‘intra’ buttons) can be chosen for executing a corresponding inter-phase or intra-phase operation. Here, an inter-phase control is taken as an example. To start a phase control, a file contains measured information of the pulse bursts needed to be loaded via the ‘Load’ button. The measured amplitude profiles and retrieved phase profiles for each individual pulse within a burst, the time scale, the central time of the first pulse, the setting time separation between pulses, the pulse duration and the pulse number are all included. It is noted that the *B*-integral value was evaulated by retrieving the phase with a temporal range of 1.8 ns. Then this data will be read and processed, and the phase differences between the *B*-integral value of each pulse and the average *B*-integral value of all pulses will be calculated and showed in the first subplot. The corresponding std of these phase difference values was evaluated and showed in the second subplot for each data loading operation. As mentioned before, the inter-phase optimization is completed through adjusting the pulse amplitudes. To reduce the multiple iterations, a PID algorithm was employed to compensate these inter-phase differences. A correction based on the proportional, integral and derivative terms related to the phase difference (error) was applied. In other words, an optimized output will be reached when a minimum phase difference was achieved. The measured amplitude peak values (cross mark) and setting values (circle mark) after correction will be shown in the third subplot. After acquiring the setting amplitude information, the correction can be finished by clicking the ‘Set Amp’ button. With a new setting, then the measurement block is used to acquire the data again and load it for the next correction. The ‘Reset’ button can clear all the corrected data and make the phase correction ready to execute with the loaded data. For the ‘Set Test Phase’ button, it can be used to load an external phase information for checking without influencing out correction procedure. The value in the ‘Peak No.’ field shows the interation number that has been executed. Finally, the data of each correction can be automatically saved if the ‘Save’ button has been ticked. In terms of the intra-phase control, a same correction precedure and a similar PID algorithm was applied. The

'Set Phase' button was utilized to execute each correction.

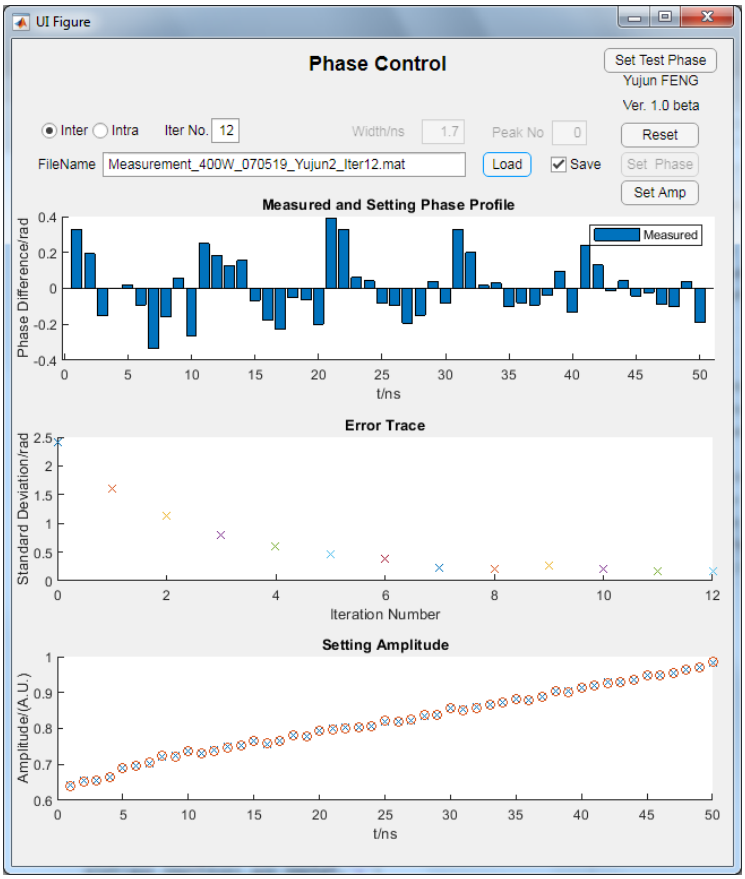


Figure 5.7: The panel of the phase (inter- and intra-) control block.

## 5.5 Instantaneous-phase equalisation and amplitude control results

Figure 5.8 shows the setting input pulse peak amplitude, measured temporal normalized amplitude and phase profiles of the output pulse-burst without any compensations. As can be seen in Figure 5.8 (a), the peak amplitudes of all 50 input pulses are equal and normalized (only 1 $V_{p-p}$). After amplification, the output burst energy was estimated to 1.15 mJ. The pulse-burst had a gain compression of ~6.3, which is greater than the calculated value of 4.8 since the input pulse-burst is slightly saturated. From the acquired phase profiles shown in Figure 5.8 (b), the corresponding *B*-integral was retrieved as I described in Chapter 4. Its value degraded from 16.2 rad in the leading pulse to 7.4 rad in the trailing pulse. As revealed by the simulation, the amplitude fluctuation will be turned into phase fluctuation in the output which will further degrade the combining efficiency. From the measured data, the std of relative phase in peak, i.e., *B*-integral was ~3%. The difference in the *B*-integral for all pulses from the average *B*-integral (10.3 rad) of all pulses is also shown in Figure 5.9 (a). The std of the phase

difference among 50 pulses was calculated to 2.01 rad. Figure 5.9 (b) shows the corresponding difference in instantaneous phase profile for selected pulses. The remaining large phase difference (a maximum of 8.8-rad) and the further potential phase distortions between pulses will significantly affect the pulse combining (stacking) efficiency. In this case, only a calculated 14% combining efficiency was achieved.

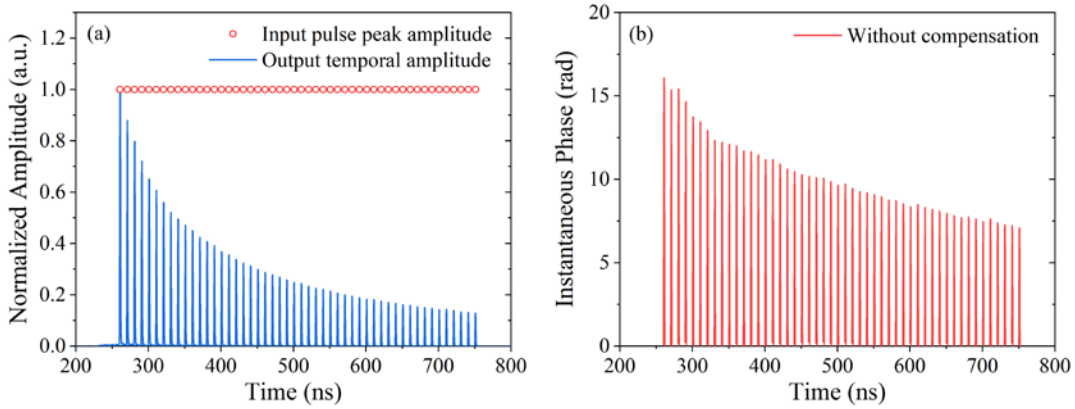


Figure 5.8: (a) Input pulse peak amplitude profile and output pulse-burst temporal normalized amplitude and (b) output instantaneous phase profiles without any compensations.

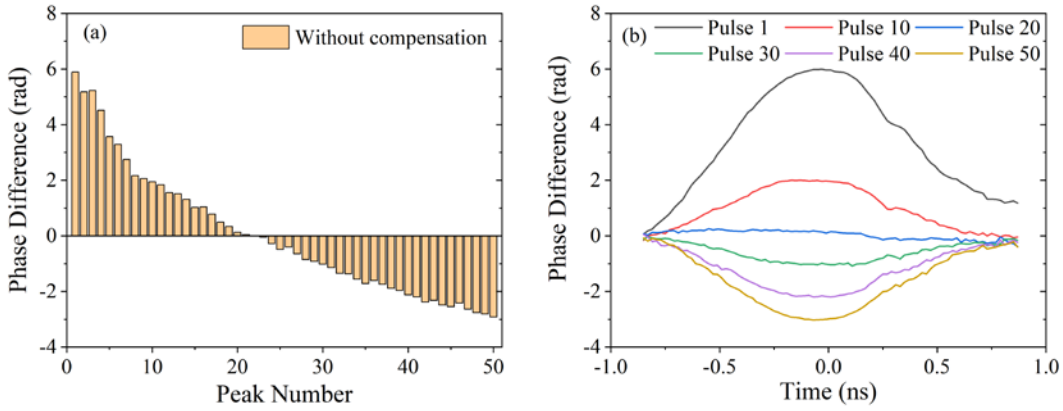


Figure 5.9: (a) Difference in the *B*-integral for all pulses from the average *B*-integral of all pulses and (b) difference in the instantaneous phase for selected pulses from the average phase profile of all pulses without any compensations.

The previous simulation has revealed that the phase difference plays a dominant influence on the pulse coherent combining efficiency while the effect from the amplitude is negligible. To calculate the input pulse-burst amplitude profile producing a target pulse-burst with equal *B*-integral output at a same 1.15 mJ output pulse energy amplifier, I determined the parameters from optimizations with a series of iteration operations. Based on the std analysis on the output *B*-integral of the pulses, an input pulse-burst with optimized peak amplitude profile was reproduced, as shown in Figure 5.10 (a). Then, the profile was loaded into the AWG that drives

the EOM. The input pulse-burst had a variant normalized amplitude among pulses, which escalates from 0.66 of the leading pulse to 0.97 of the trailing pulse. Limited by the maximum $V_{p-p}$, the output power from the EOM was reduced with the reduction of setting input amplitude (0.66–0.97 $V_{p-p}$). The measured temporal normalized amplitude and phase profiles of the output pulse-burst with an amplitude compensation are also shown in Figure 5.10. After amplitude adjustment, the gain compression of the amplified pulse-burst amplitude prolife reduced from ~6.3 to ~4.5. As shown in Figure 5.10 (b), the inter-pulse amplitude compensation basically equalised the *B*-integral to ~11.4 rad. The std of relative *B*-integral was reduced to less than 2%. Compared to the result in Figure 5.9 (a), the difference in the *B*-integral for all pulses from the average *B*-integral of all pulses is much smaller, as shown in Figure 5.11 (a). The std of the phase difference among 50 pulses was calculated to only 0.11 rad. From the selected instantaneous phase profiles shown in Figure 5.11 (b), it can be seen that even with inter-pulse amplitude compensation, the intra phase of the pulses still varied in a range of ~1.1 rad and with different phase profiles. Though greatly improved from the original 14%, only an 80% combining efficiency was calculated due to the remaining intra-phase difference between pulses.

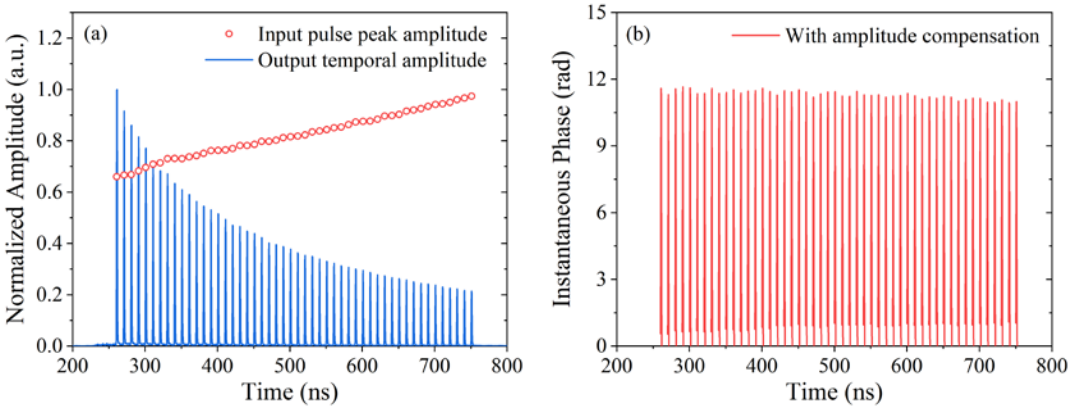


Figure 5.10: (a) Input pulse peak amplitude profile and output pulse-burst temporal normalized amplitude and (b) output instantaneous phase profiles with amplitude-only compensation.

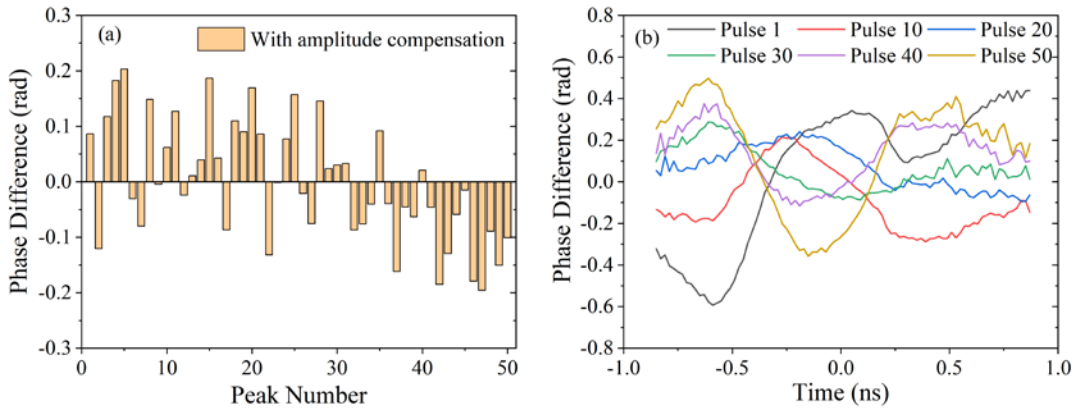


Figure 5.11: (a) Difference in the *B*-integral for all pulses from the average *B*-integral of all pulses and (b) difference in the instantaneous phase for selected pulses from the average phase profile of all pulses with amplitude-only compensation.

To further improve the coherent combining efficiency, an essential intra-pulse phase compensation was performed. Figure 5.12 (a) shows the input pulse peak amplitude profile and the output temporal amplitude which are the same as the results shown in Figure 5.10 (a). Then the iteration operation was executed by adjusting the intra-phase information of each pulse imprinted on the EOPM to achieve an optimized input individual phase profile. As shown in Figure 5.12 (b), the phase profiles were further equalised due to an optimized input phase profile. The std of the relative *B*-integral was nearly 1%. Revealed in Figure 5.13 (a), the difference in the *B*-integral still maintained within a ±0.2 rad range without a further diminishment. This is coincided with the phase measurement limit as mentioned in Chapter 4. However, the resulting phase differences within pulses were diminished, as shown in Figure 5.13 (b). The phase difference profiles of each pulse were nearly identical and only varied in a 0.6-rad range, which finally guaranteed a 90% achievable combining efficiency.

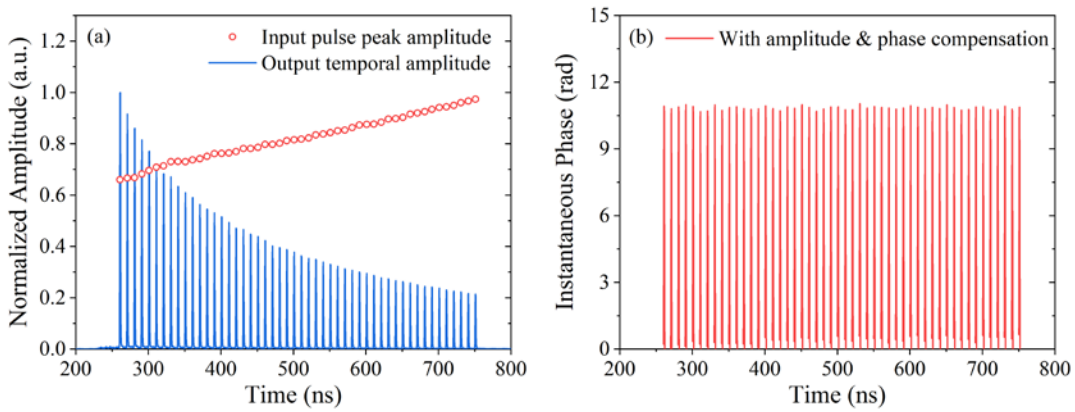


Figure 5.12: (a) Input pulse peak amplitude profile and output pulse-burst temporal normalized amplitude and (b) output instantaneous phase profiles with both amplitude and phase compensation.

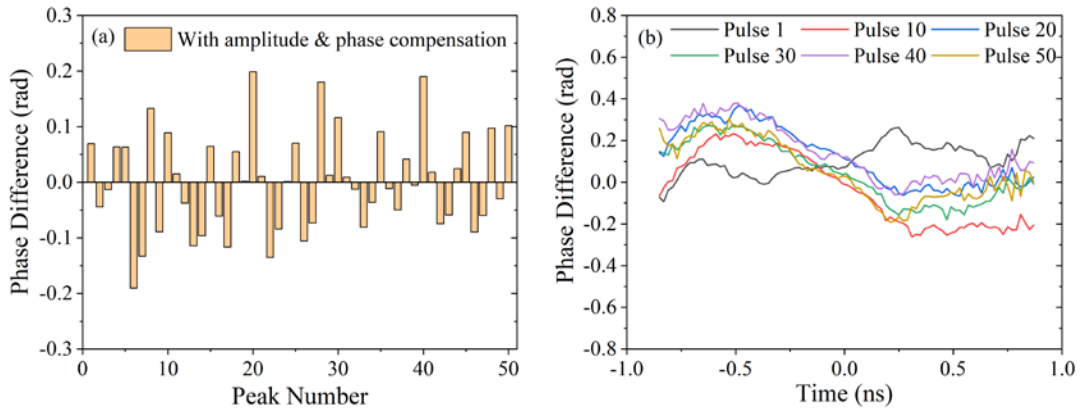


Figure 5.13: (a) Difference in the *B*-integral for all pulses from the average *B*-integral of all pulses and (b) difference in the instantaneous phase for selected pulses from the average phase profile of all pulses with both amplitude and phase compensations.

## 5.6 Conclusion

In conclusion, I have investigated the influence of amplitude difference, *B*-integral difference and input amplitude fluctuation between pulse-burst on the coherent combining efficiency. Based on the calculation results, I designed an optimized inter-pulse amplitude compensation and intra-pulse instantaneous-phase equalisation using fast EOMs. Finally, I demonstrated that a 90% coherent pulse stacking efficiency can be theoretically achieved in a high-nonlinear (*B*-integral >10 rad) and energy-saturated (1.15 mJ) narrow-linewidth linearly-polarised DPA system. It should/may be possible to equalise the phase also with *B*-integral much larger than 10 rad. Further, the measurement system automation and feedback control open up for compensation of aging-induced [9] and power-induced phase distortions in narrow-line and chirped-pulse amplification systems.

## References

[1]. T. Zhou, J. Ruppe, C. Zhu, I-N. Hu, J. Nees, and A. Galvanauskas, “Coherent pulse stacking amplification using low-finesse Gires-Tournois interferometers”, Opt. Express **26**, 7442 (2015).

[2]. J. Ruppe, “Theoretical and experimental foundations of coherent pulse stacking amplification”, Ph.D. thesis (University of Michigan, 2017).

[3]. F. Guichard, L. Lavenu, M. Hanna, Y. Zaouter, and P. Georges, “Coherent combining efficiency in strongly saturated divided-pulse amplification systems”, Opt. Express **24**, 25329 (2016).

[4]. A. Klenke, M. Kienel, T. Eidam, S. Hädrich, J. Limpert, and A. Tünnermann, “Divided-pulse nonlinear compression”, Opt. Lett. **38**, 4593 (2013).

[5]. F. Guichard, M. Hanna, Y. Zaouter, D. N. Papadopoulos, F. Druon, and P. Georges, “Analysis of Limitations in Divided-Pulse Nonlinear Compression and Amplification”, IEEE J. Sel. Top. Quantum Electron. **20**, 7600405 (2014).

[6]. M. Kienel, A. Klenke, T. Eidam, M. Baumgartl, C. Jauregui, J. Limpert, and A. Tünnermann, “Analysis of passively combined divided-pulse amplification as an energy-scaling concept”, Opt. Express **21**, 29031 (2013).

[7]. Y. Zaouter, F. Guichard, L. Daniault, M. Hanna, F. Morin, C. Hönninger, E. Mottay, F. Druon, and P. Georges, “Femtosecond fiber chirped- and divided-pulse amplification system”, Opt. Lett. **38**, 106 (2013).

[8]. F. Guichard, L. Lavenu, M. Hanna, Y. Zaouter, and P. Georges, “Coherent combining efficiency in strongly saturated divided-pulse amplification systems”, Opt. Express **24**, 25329 (2016).

[9]. Y. Feng, B. M. Zhang, and J. Nilsson, “Photodarkening-Induced Phase Distortions and Their Effects in Single-Channel and Coherently Combined Yb-Doped Fiber Chirped Pulse Amplification Systems”, J. Lightwave Technol. **36**, 5521 (2018).

# Chapter 6
# Passive coherent beam combination in an ultrafast pulse twin-core fibre amplifier in the highly nonlinear regime

## 6.1 Overview

In principle, for the work done in Chapter 4 and 5, the motivation is to characterize and control the induced phase distortions between pulses in the highly nonlinear regime and then realize an efficient coherent combination in the DPA-CPS systems. Though no practical experiment of a coherent combining has been implemented, theoretical calculations have confirmed that a 90% of combining efficiency can be achieved at a *B*-integral of >10 rad with a corrected phase result. In this chapter, I experimentally demonstrated that a 90% combining efficiency can be achieved in an ultrafast parabolic-pulse twin-core fibre amplifier at a *B*-integral of 29 rad without using any active phase controls. Section 6.2 briefly introduces the previous research on ultrafast pulse coherent combination in the highly nonlinear regimes through different combining techniques. The details of a self-designed and in-house fabricated twin-core double-clad PM Yb-doped fibre which was used in the coherent combination experiments are given in Section 6.3. Then an experiment on coherently combining two ultrafast parabolic-pulses in the twin-core Yb-doped fibre amplifier has been implemented. The relevant experimental setup, achieved results, and analysis are included in Section 6.4. Finally, the conclusions are given in Section 6.5.

## 6.2 Introduction

It has been revealed that SPM (quantified by *B*-integral) has an inevitable impact on multi-channel ultrafast pulse coherent combination. As analysed in Ref. [1], when reaching an average *B*-integral of 25 rad, the relative *B*-integral deviation among the amplifiers should be less than 2% for a >90% efficiency. A number of decent results on ultrafast pulse combination have been demonstrated. Typically, SPM-induced phase differences between different channels can be eliminated via passive or active phase locking methods. Through passive combining of two femtosecond fibre CPAs, a combining efficiency of 84% was achieved at a *B*-integral of 12 rad [2] and a 91.5% efficiency was realized at a 7-rad *B*-integral [3]. To the best of our knowledge, in an active phase stabilization scheme, the highest reported operating

*B*-integral is 12 rad, where an 89% efficiency has been obtained in a fibre CPA system consisting of two coherently combined fibre amplifiers [4]. Recently, 3.5 kW average output power was achieved from four combined femtosecond Yb-doped fibre amplifiers with an 88.2% combining efficiency at a *B*-integral of 11 rad [5]. In configurations of combining ultrafast pulses from distinct fibre amplifiers, including but not limited to fibre length mismatch, *B*-integral differential and different pump contributed phase noise amounts necessitate a higher requirement of active phase control for efficient combination. However, multicore fibre would be an alternative solution which offers an attractive possibility for ultrafast pulse coherent combination with less components, simpler phase stabilization scheme and a more compact footprint. Successful ultrafast pulse combinations have been demonstrated in 4-core [6], 7-core [7, 8], 12-core [9], 16-core [10], and even 49-core [11] fibres. In these systems, microlens arrays or segmented mirror splitters were used to match the beam into the cores. Active phase controllers (e.g., spatial light modulator) were also applied for phase stabilization. Again, these multicore ultrafast pulse fibre amplifiers operate in a relatively low *B*-integral regime (<8 rad). For higher energy extraction potential consideration, it is of great interest to explore the coherent beam combination of ultrafast pulses in a higher nonlinear regime.

Here, I report the demonstration of a passive coherent beam combination in an ultrafast twin-core fibre amplifier in the highly nonlinear regime. To realize that, a single-mode, PM twin-core double-clad Yb-doped fibre with carefully equalised cores was designed and fabricated. A Dammann grating was applied to match the beam into two cores. To the best of our knowledge, it is the first experimental realization of a 90% coherent combining efficiency in an ultrafast parabolic pulse twin-core fibre amplifier with a *B*-integral as high as 29 rad. Even without any active phase controls, the equalisation and proximity of the cores diminished the phase differences induced by SPM as well as other effects (e.g., thermal) between the two cores and thereby guaranteed a high combining efficiency. It verified that an integrated multicore fibre is suitable for a compact and efficient coherent beam combination.

## 6.3 PM twin-core double-clad Yb-doped fibre

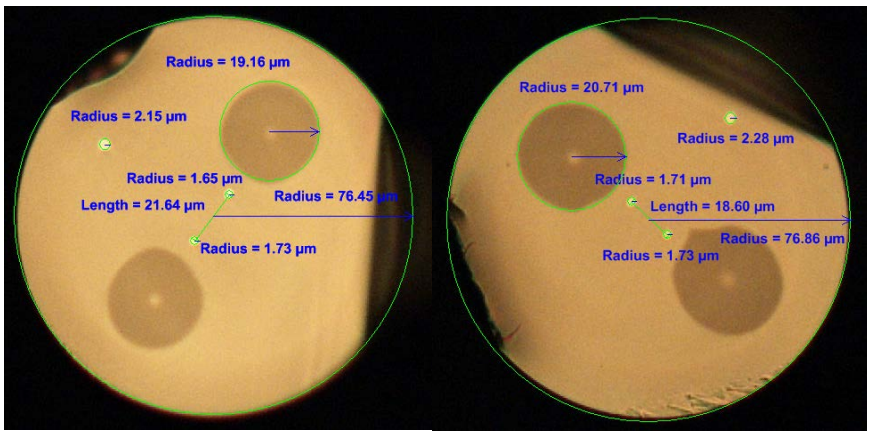


Figure 6.1: Images of the PM twin-core Yb-doped fibre start and end facets.

To investigate the ultrafast pulse coherent combination in the highly *B*-integral regime, a PM twin-core double-clad Yb-doped phosphosilicate fibre (A1214-L10596-L10469) was designed and fabricated. Images of the PM twin-core double-clad Yb-doped fibre start and end facets are shown in Figure 6.1. The fibre consisted of two active cores and a passive core. The active core preform (L10596) was fabricated by the standard MCVD and solution doping technique. Its refractive index profile is presented in Figure 6.2, the core NA was estimated to be ~0.28 though having a large dip in the refractive index at the centre of the core. As seen in Figure 6.1, both active cores had a diameter of ~3.4 µm. The equalisation of these two cores was achieved by fabricating them from adjacent sections from the same core preform. This overcomes potential non-uniformity in the core preform. Note that this special approach does not scale well to large cores (which use more core material) and more than two cores, since then not all core preform sections can be adjacent to each other. The pitch between the active core centres was 21.6 µm at the start facet while 18.6 µm for the end facet for a 150-m length of fibre. Based on the simulation, the coupling between two cores becomes negligible when reaching a 17-µm spacing. Thus, these two cores can act as two isolated waveguides. In terms of the embedded passive core, it was designed for other purposes but not considered in this investigation. It had a ~4.4-µm core diameter and a 0.16 core NA. Additionally, two stress rods placed adjacent to the cores with a suitable spacing were used to induce stress birefringence and thus polarisation-maintenance. The inner-cladding had a diameter of 153 µm with a nominal NA of 0.48. The cladding pump absorption was measured to 4 dB/m at 975 nm.

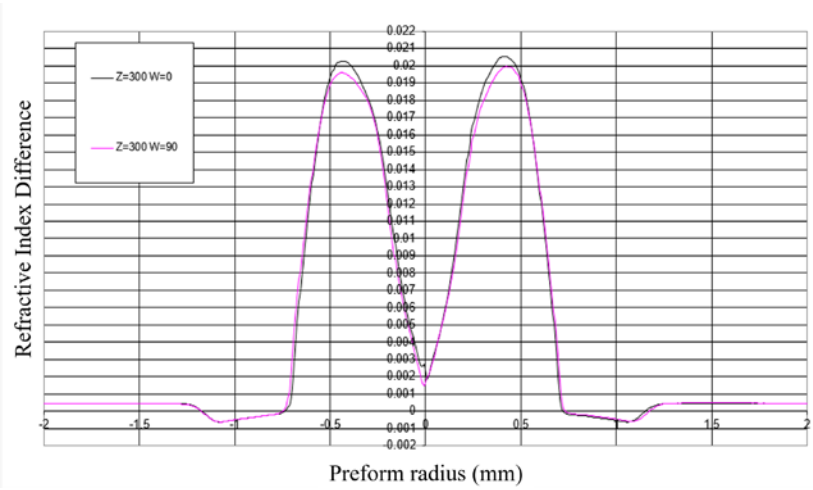


Figure 6.2 Refractive index profile of the active core preform (L10596).

## 6.4 Coherently combined ultrafast twin-core fibre amplifier

### 6.4.1 Experimental setup and combination evaluation

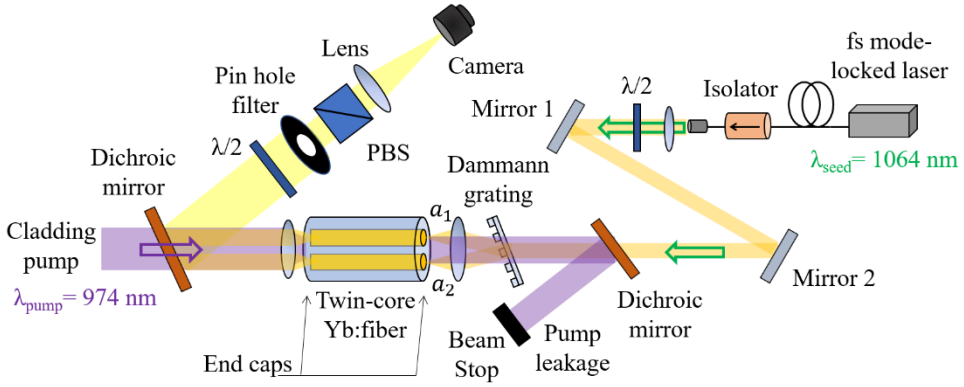


Figure 6.3: Schematic of the twin-core Yb-doped fibre amplifier and beam combination measurement setup.

The twin-core Yb-doped fibre amplifier, beam combination and measurement setup are schematically shown in Figure 6.3. A 3-m-length of the PM twin-core double-clad Yb-doped fibre served as the gain medium. It was loosely coiled at ~20 cm diameter and fixed on the optical table with scotch tape. Both fibre ends were spliced to two appropriate lengths of 400-μm coreless fibres, which were angle-cleaved and served as endcaps to prevent optical damage of the fibre facets. Typically, an ultrafast pulse with a 10-nm spectral bandwidth has a coherence length of approximate 50 μm. In our case, the OPLD between the paths through the two cores imposed by those small cleaved-angle deviations was much smaller than the coherence length. Thus, a pronounced interference pattern can be obtained when combining two beams. In the amplifier, the 1064 nm signal was provided by a commercial femtosecond

fibre source (Fianium FemtoPower 1060-2-FS) operating at a 50 MHz repetition rate and a pulse duration of ~470 fs at a full power (~2 W) output. The signal was collimated and coupled into two fibre cores through a number of mirrors, a Dammann grating [12] and a coupled lens. Herein, the Dammann grating acts as a beam splitter and deliveries two divided beams to both cores not only improve the signal coupling efficiency but also distribute equal power into the two cores. The principle and operation of the Dammann grating are fully explained and illustrated in Ref. [13]. In our practical operation, a weak ASE beam generated by the twin-core fibre cavity itself was initially utilized for the Dammann grating alignment. The fibre was counter-pumped by focusing the light from a 974-nm diode laser into the inner cladding. At the pump end, a DM was used to transmit the input pump light while reflecting the output signal. Meanwhile, another DM separated the unabsorbed pump light from the transmitted signal light at the signal input end. Spatial profile outputs from two cores were measured by a CMOS camera (Thorlabs DCC1545M, 1280×1024 pixels of 1/2" size).

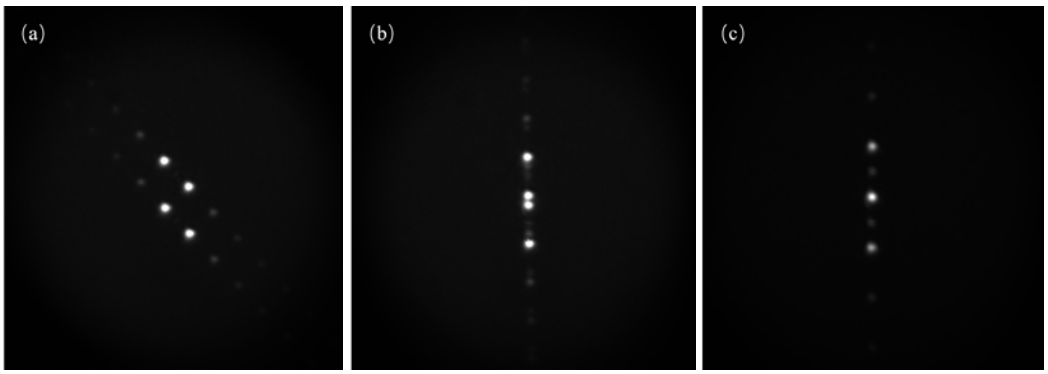


Figure 6.4: The output image of the ASE after passing through a lens and a Dammann grating (a) with random position, (b) with matched rolling angle, and (c) with both matched rolling and yawing angles.

The coupling of the signal into two cores was realized by the Dammann grating in a series of steps. Firstly, the fibre was placed on a V-groove and rolled until both two cores are lying in the horizontal plane, confirmed by the output ASE image on the camera. Figure 6.4 (a) shows the output image of the ASE after passing through a lens and an unaligned Dammann grating. The output beam from each core was split into multiple orders which are spatially distributed with equal spacing. Then the Dammann grating was rotated until the plane of the two cores is perpendicular to the grating direction. The relevant output image is shown in Figure 6.4 (b). It can be seen that two sets of multiple order output beams from two cores were located exactly along a line. However, there is still a spatial deviation between the +1 order beam from one core and the −1 order beam from another core. This can be optimized by adjusting the yawing angle of the Dammann grating. With a suitable yawing angle, the +1 order beam was finally overlapped with the −1 order beam, as shown in Figure 6.4 (c). Reciprocally, an on-axis order

input beam, i.e., the central spot, can be split and coupled into the two cores accurately. After that initial alignment operation, the input signal can be coupled into two cores by finely adjusting mirror 1 and mirror 2.

At the output end, a size-matched pinhole spatial filter was inserted to block signal light emerging from the cladding, caused by an imperfect launch. However, the cladding light emerging between two cores was not eliminated and may have an impact on the combination evaluation. Furthermore, a half-wave plate and a PBS were used to stabilize the output mode polarisation. The PER was measured to be 16 dB. Eventually, the beams from two cores were spatially combined through a lens with a focal length of 300 mm. In this combination configuration, no active phase controls were applied. The interference pattern of the combined beam was measured by the camera with attenuated signal intensity. The fringe visibility $V$ of the interference pattern can be expressed as

$$V = \frac{I_{max} - I_{min}}{I_{max} + I_{min}}, \tag{6.1}$$

where $I_{max}$ and $I_{min}$ are the maximum and minimum intensities along the fringe central cross section. To determine the coherent combining efficiency, a parameter called degree of coherence $\gamma$ was introduced. The relationship between the visibility and the degree of coherence is given by

$$V = \frac{2\sqrt{I_1 I_2}}{I_1 + I_2}|\gamma|, \tag{6.2}$$

where $I_1$ and $I_2$ are the two core intensities. Then, the coherent combining efficiency can be evaluated as

$$\eta = \frac{I_1 + I_2 + 2\sqrt{I_1 I_2}|\gamma|}{(\sqrt{I_1} + \sqrt{I_2})^2}. \tag{6.3}$$

For better visibility all the measured intensity distributions were normalized.

### 6.4.2 Experimental results and analysis

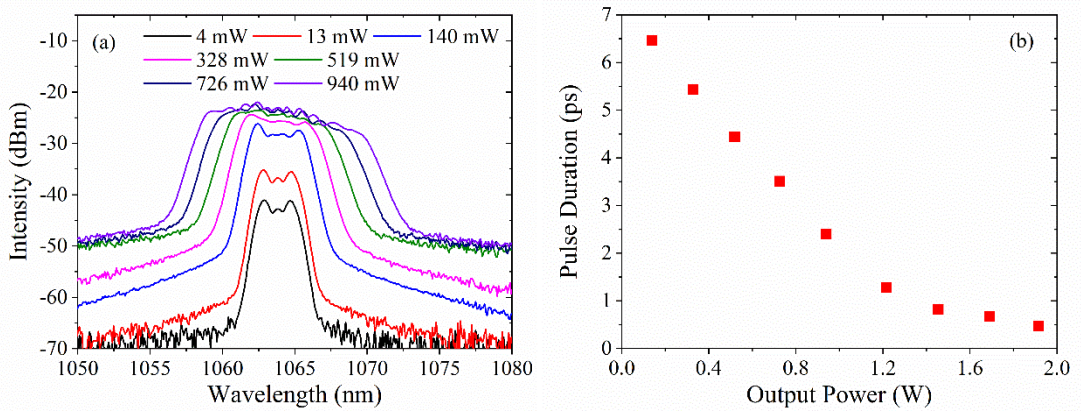


Figure 6.5: Femtosecond seed source (a) output spectrum characteristic, resolution: 0.05 nm and (b) pulse duration *vs*. output power.

First, the output of the seed source was characterized. The output spectra of the femtosecond seed source at different output powers are plotted in Figure 6.5 (a). The 20-dB spectral bandwidth (full-width at 1% of the maximum intensity) increased from 5-nm to 15-nm with increasing output power. It is noticeable that the flat-top spectral profile can be maintained when experiencing a spectral broadening, which is a typical characteristic of the parabolic pulse evolution. The output pulse duration was characterized by an auto-correlator (Femtochrome FR-103MN) and the results are shown in Figure 6.5 (b). The pulse duration gradually decreased from 6.5 ps to 2.4 ps with an output power from 140 mW to 940 mW.

A seed signal with a 140-mW output power and a 6.5-ps pulse duration was initially utilized for the investigation. Mainly due to a large insertion loss of the Dammann grating and a low coupling efficiency, only an estimated 6-mW of power was launched into two cores, i.e., 3-mW in each core. After amplification, the total output signal power from two cores as a function of absorbed pump power is shown in Figure 6.6 (a). The output power increased linearly with the absorbed pump power and reached a maximum power of ~830 mW, which is limited by the available pump power. A 21-dB gain was obtained in this amplifier. It can also be confirmed that the beams from two cores have a same intensity, as the captured output beam image shown in Figure 6.6 (a) inset. Figure 6.6 (b) shows the output signal spectrum as a function of output signal power. With the growth of signal power, the output spectrum was broadened due to SPM. The 20-dB spectral bandwidth of the seed (passing through the fibre without amplification) was estimated to be ~5 nm. It was further broadened to ~13 nm at maximum output power. The autocorrelation traces of the amplified pulse under different output powers have also been measured. The signal pulse duration increased to 8 ps after passing through the twin-core fibre. With the growth of output power, the pulse duration

broadened gradually and reaching a maximum value of 10 ps. These pulse broadenings are well-matched to the calculated chromatic dispersion. Besides, the signal PER remained 14.5 dB at maximum output.

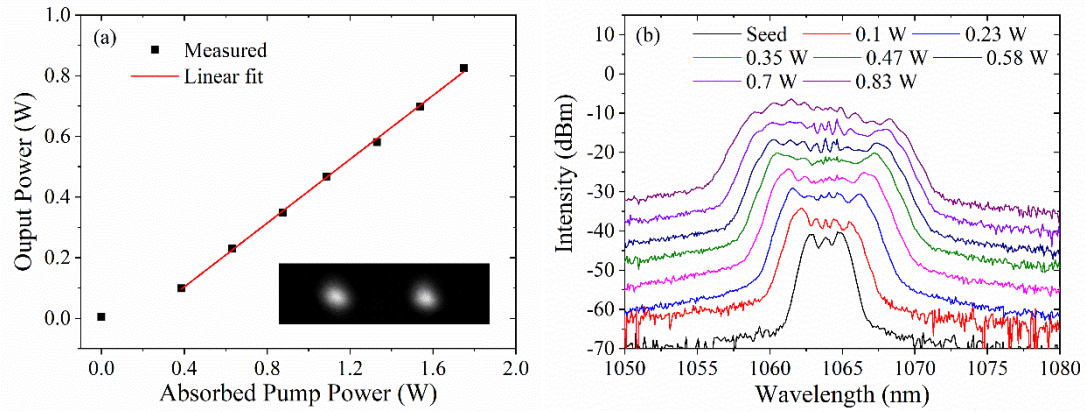


Figure 6.6: (a) The output signal power characteristic of the amplifier and (b) output signal spectra at different pump powers, resolution: 0.05 nm.

Based on the measured input signal duration and power, and the output signal durations and powers under different pump-levels, the peak power distribution along the fibre length can be retrieved in a backward-pumped fibre amplifier model. Then according to Equation (2.10), the *B*-integral can be calculated. The results are shown in Figure 6.7 (a), where the *B*-integral increased linearly with the output power and reached a maximum value of 16.7 rad. The corresponding fringe patterns were recorded by the camera. Based on Equations (6.1) – (6.3), the retrieved visibility and combining efficiency as a function of *B*-integral are plotted in Figure 6.7 (b). With the growth of *B*-integral, the visibility increased from 0.93 to 0.95 and then gradually degraded to 0.89 at a maximum output power. It is noted that the values of degree of coherence and visibility are the same since two cores are of equal intensity. Consequently, it is seen that the combining efficiency had a maximum value of 97.5% at a *B*-integral of 8.8 rad and decreased to 94.5% at a *B*-integral of 16.7 rad. At the low output power, the small portions of signal emerging from the cladding slightly degraded the visibility and thus the combining efficiency to 96.6%. At the high *B*-integral value, a *B*-integral difference between two amplifier channels induced a slight drop in combining efficiency.

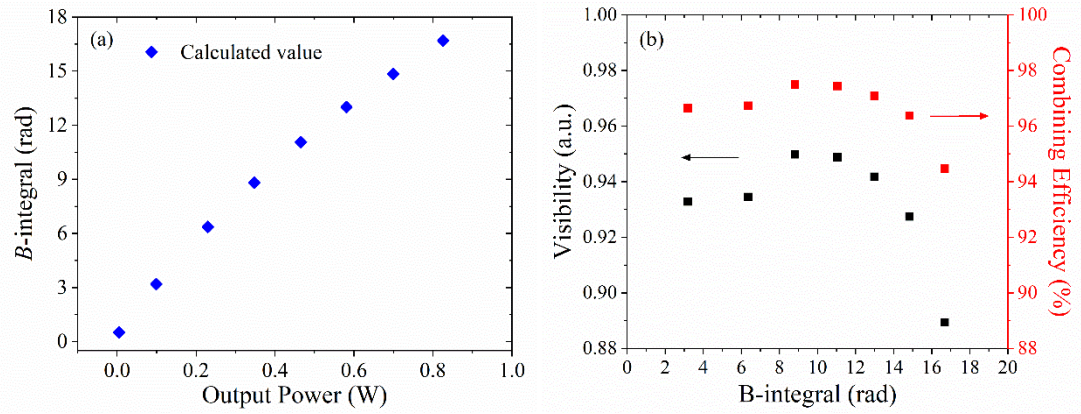


Figure 6.7: (a) *B*-integral *vs.* output power and (b) visibility and combining efficiency *vs. B*-integral.

Two selected results on retrieved intensity distributions along the central cross section of the fringe pattern are plotted in Figure 6.8. The inset shows the measured intensity distributions of the whole combined beam profiles. The result illustrated in Figure 6.8 (a) corresponds to the output with the highest visibility (0.95), while the counterpart at a maximum 16.7-rad *B*-integral is shown in Figure 6.8 (b). Furthermore, it can be confirmed from the recorded image that the fraction of cladding light is negligible with a spatial filter. It is clear that the visibility of the fringe pattern will be degraded accompanied with an appropriate amount of cladding light.

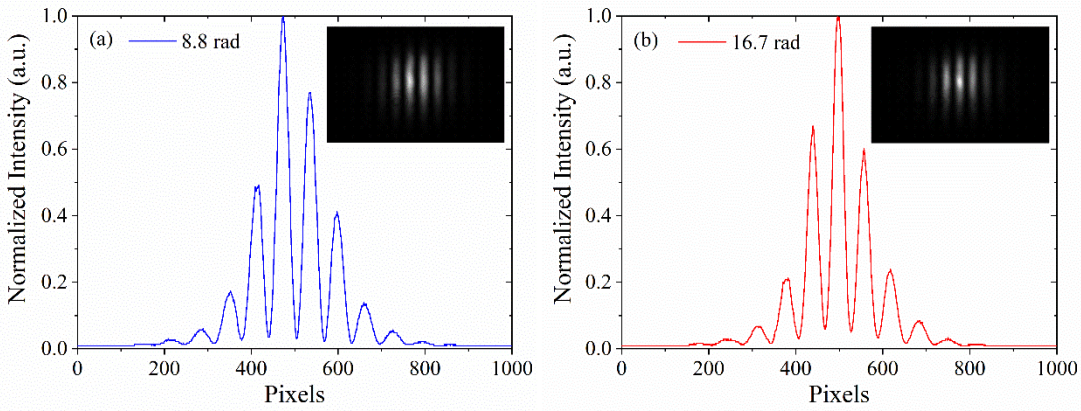


Figure 6.8: Intensity distributions along the central cross section of the combined beam profile at a *B*-integral of (a) 8.8 rad and (b) 16.7 rad. Inset: measured combined beam profiles.

Typically, a 90% combining efficiency would be an acceptable level. From the above results, a combining efficiency of 94.5% was achieved when the amplifier reaches a *B*-integral of 16.7 rad. Therefore, the *B*-integral in the amplifier can be further increased while maintaining at least 90% combining efficiency. Then, a seed signal with an output power of 519 mW and a pulse duration of 4.5 ps was used to push the amplifier to higher *B*-values. The launched

power in each core was estimated to be ~10 mW. After amplification, the total output signal power from two cores as a function of absorbed pump power is shown in Figure 6.9 (a). The output power increased linearly with the absorbed pump power and reached a maximum output power of 1.03 W. It is again limited by the available pump power. A reasonable 17-dB gain was obtained in this amplifier. The beams from two cores have the same intensity. Figure 6.9 (b) shows the output signal spectrum as a function of output signal power. With the growth of signal power, the output spectrum was broadened and accompanied by an oscillatory structure. The 20-dB spectral bandwidths were ~11 nm and ~27 nm for the initial input signal and the signal with maximum output power, respectively. The pulse duration increased from 6 ps to 8 ps with increasing output signal power, which matches the chromatic dispersion well. At the maximum output, the signal had a 15-dB PER.

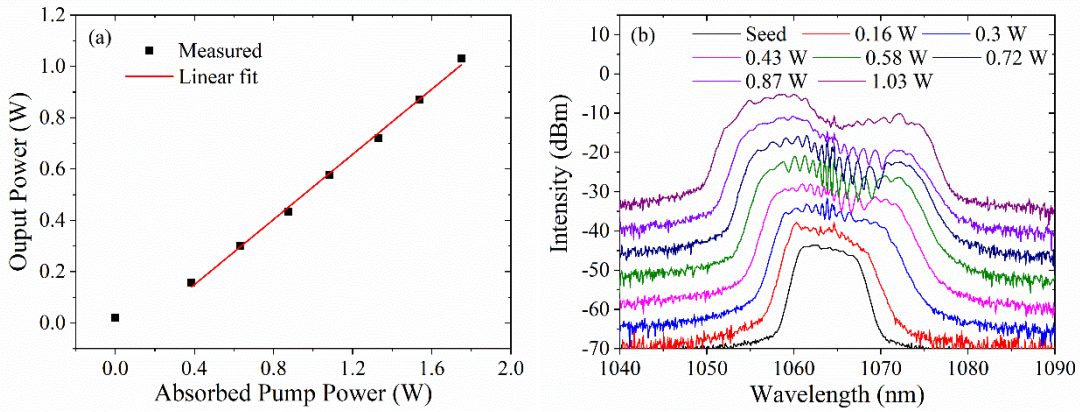


Figure 6.9: (a) The signal output power characteristic of the amplifier and (b) output signal spectra at different pump powers, resolution: 0.05 nm.

The calculated *B*-integral is shown in Figure 6.10 (a). It increased linearly with the output power and reached a maximum value of 30.2 rad because of a higher output power and a shorter pulse duration. The acquired visibility and combining efficiency as a function of *B*-integral are plotted in Figure 6.10 (b). The visibility had a maximum value of 0.93, which is slightly smaller than the 0.95 obtained in the previous result. This degradation may be caused by an increased portion of signal in the cladding. At the maximum output power of 1.03 W, the visibility dropped to only 0.77. Correspondingly, the combining efficiency had a maximum value of 96.5% at a *B*-integral of 12.2 rad. However, the combining efficiency finally decreased to only 88.5%, presumably due to a large quantity of nonlinear phase shift in the amplifier. In the higher nonlinear regime, any tiny pulse fluctuations can induce larger *B*-integral differential between two amplifier channels, thus degrading the combination efficiency. From the combining efficiency trend shown in Figure 6.11 (b), I estimated that a 90% combining efficiency can be achieved at a *B*-integral of ~29 rad.

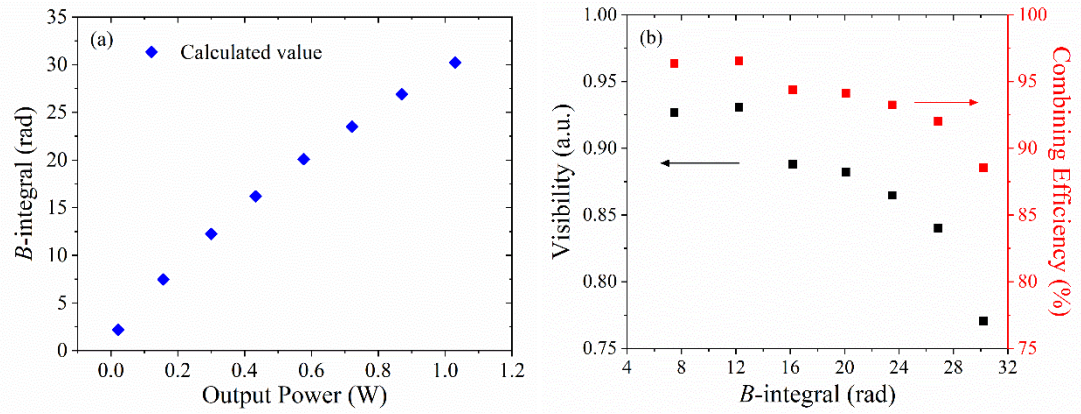


Figure 6.10: (a) *B*-integral *vs.* output power and (b) visibility and combining efficiency *vs. B*-integral.

Two selected results on retrieved intensity distributions along the central cross section of the fringe pattern are plotted in Figure 6.11. The inset shows the measured intensity distributions of the whole combined beam profiles. The result at the highest visibility (i.e., 0.93) output is illustrated in Figure 6.11 (a) and the counterpart with a maximum *B*-integral (i.e., 30.2-rad) is shown in Figure 6.11 (b). As before, the fraction of cladding light is negligible.

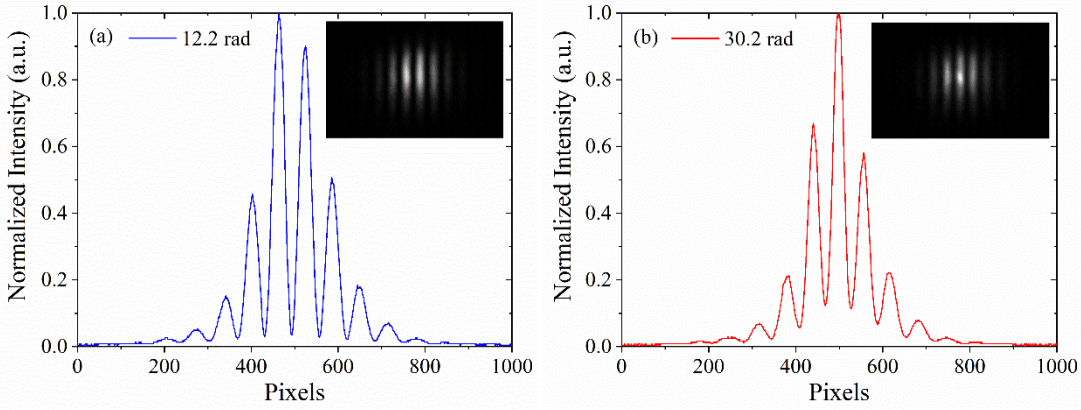


Figure 6.11: Intensity distributions along the central cross section of the combined beam profile at a *B*-integral of (a) 12.2 rad and (b) 30.2 rad. Insets: measured combined beam profiles.

## 6.5 Conclusion

In conclusion, I have experimentally demonstrated passive coherent beam combination in an ultrafast parabolic-pulse twin-core Yb-doped fibre amplifier in the highly nonlinear regime. A 90% coherent combining efficiency was achieved though the amplifier has a *B*-integral of ~29 rad in a single core. The core proximity provided a great tolerance of SPM-induced phase difference between two cores and finally guaranteed a high combining efficiency. It provides a proof of the applicability of the passive coherent combination in an integrated multicore

dopant fibre with a relatively high-nonlinearity due to SPM. These results would benefit the coherent beam combination community with advantages on system compactness and efficiency.

## References

[1]. S. Jiang, M. Hanna, F. Druon, and P. Georges, “Impact of self-phase modulation on coherently combined fiber chirped-pulse amplifiers”, Opt. Lett. **35**, 1293 (2010).

[2]. L. Daniault, M. Hanna, D. N. Papadopoulos, Y. Zaouter, E. Mottay, F. Druon, and P. Georges, “Passive coherent beam combining of two femtosecond fiber chirped-pulse amplifiers”, Opt. Lett. **36**, 4023 (2011).

[3]. Y. Zaouter, L. Daniault, M. Hanna, D. N. Papadopoulos, F. Morin, C. Hönninger, F. Druon, E. Mottay, and P. Georges, “Passive coherent combination of two ultrafast rod type fiber chirped pulse amplifiers”, Opt. Lett. **37**, 1460 (2012).

[4]. A. Klenke, E. Seise, S. Demmler, J. Rothhardt, S. Breitkopf, J. Limpert, and A. Tünnermann, “Coherently-combined two channel femtosecond fiber CPA system producing 3 mJ pulse energy”, Opt. Express **19**, 24280 (2011).

[5]. M. Müller, A. Klenke, A. Steinkopff, H. Stark, A. Tünnermann, and J. Limpert, “3.5 kW coherently combined ultrafast fiber laser”, Opt. Lett. **43**, 6037 (2018).

[6]. A. Klenke, M. Wojdyr, M. Müller, M. Kienel, T. Eidam, H. Otto, F. Stutzki, F. Jansen, J. Limpert, and A. Tünnermann, “Large-pitch Multicore Fiber for Coherent Combination of Ultrashort Pulses”, in 2015 European Conference on Lasers and Electro-Optics/European Quantum Electronics Conference (Optical Society of America, 2015), paper CJ_1_2.

[7]. I. Hartl, A. Marcinkevičius, H. A. McKay, L. Dong, and M. E. Fermann, “Coherent beam combination using multi-core leakage-channel fibers”, in Advanced Solid-State Photonics (Optical Society of America, 2009), paper TuA6.

[8]. L. P. Ramirez, M. Hanna, G. Bouwmans, H. E. Hamzaoui, M. Bouazaoui, D. Labat, K. Delplace, J. Pouysegur, F. Guichard, P. Rigaud, V. Kermène, A. Desfarges-Berthelemot, A. Barthélémy, F. Prévost, L. Lombard, Y. Zaouter, F. Druon, and P. Georges, “Coherent beam combining with an ultrafast multicore Yb-doped fiber amplifier”, Opt. Express **23**, 5406 (2015).

[9]. P. Rigaud, V. Kermene, G. Bouwmans, L. Bigot, A. Desfarges-Berthelemot, D. Labat, A. Le Rouge, T. Mansuryan, and A. Barthélémy, “Spatially dispersive amplification in a 12-core fiber and femtosecond pulse synthesis by coherent spectral combining”, Opt. Express **21**, 13555 (2013).

[10]. A. Klenke, M. Müller, H. Stark, F. Stutzki, C. Hupel, T. Schreiber, A. Tünnermann, and J. Limpert, “Coherently combined 16-channel multicore fiber laser system”, Opt. Lett. **43**, 1519 (2018).

[11]. J. Lhermite, E. Suran, V. Kermene, F. Louradour, A. Desfarges-Berthelemot, and A. Barthélémy, “Coherent combining of 49 laser beams from a multiple core optical fiber by a spatial light modulator”, Opt. Express **18**, 4783 (2010).

[12]. H. Dammann and E. Klotz, “Coherent optical generation and inspection of two-

dimensional periodic structures", Opt. Acta **24**, 505 (1977).

[13]. W. M. Kunkel and J. R. Leger, "Gain dependent self-phasing in a two-core coherently combined fiber laser", Opt. Express **26**, 9373 (2018).

# Chapter 7
# Bendable non-circular core large-mode-area Yb-doped fibre

## 7.1 Overview

As presented in Chapters 3–6, the advanced techniques for pulse-burst temporal phase measurements and the corresponding active phase and amplitude controls, as well as the passive ultrafast pulse coherent combining in a twin-core YDFA are all investigated in pulsed systems which are operating in the highly nonlinear regime. These investigations provide potential solutions for understanding and managing the nonlinear phase distortions and thus develop high-energy pulsed fibre systems suitable for coherent combination. Although I used small cores to more easily reach the highly nonlinear regime, real systems (whether at high or low nonlinearity) will use fibres with large mode areas. Therefore, so-called LMA fibres and their operation is also of interest within the context of this thesis. A concern is that with increasing mode area, there are increasing bending distortions when fibres are bent in practical applications.

This chapter presents the investigation on the mode-area-scaling and bending performance of an Yb-doped large-mode-area fibre with an elongated non-circular core. Such a fibre can be bent in the plane of its short axis to suppress bending effects, such as mode area reduction and mode profile distortion. Meanwhile, the orthogonal long axis can be stretched for mode area scaling, to reduce nonlinear phase distortions and increase energy storage, and thus improve CPA and beam combination performance. The content of this chapter is organized as follows. Recent research on scaling the fundamental mode area and alleviating detrimental bending effects is described in Section 7.2. Section 7.3 theoretically studies bending effects and mode scaling and its limitations in bent fibres with non-circular cores. Section 7.4 describes our studies on selective-doping and tandem-pumping in proposed fibres. Both techniques can facilitate fundamental-mode operation, according to simulations. The details of the fabricated fibre and the experimental results with this fibre are given in Section 7.5 and Section 7.6, respectively. Conclusions are given in Section 7.7.

## 7.2 Introduction

As introduced in Chapter 2, several fibre designs have been developed for scaling the fibre

mode area and thus increasing the nonlinear thresholds, while maintaining single mode output. However, fibre bending often compromises the mode area and the effects of bending are recognized as an important limiting factor for mode area scaling [1]. A compact system using a short straight fibre (e.g. shorter than a meter) can sacrifice the fibre flexibility, since it can be kept straight. However, for scaling of average power, a fibre length of 10 m is more commonly used to cope with the heat generated in the multi-kW regime, and avoid coating damage and thermally induced mode degradation. Bending is difficult to avoid for such a long fibre. Bending a fibre not only squeezes the effective mode area and consequently reduces the threshold powers for nonlinear scattering and material breakdown, which become severe effects in ultrafast amplification, but also shifts the mode profile toward the cladding, and alters the mode overlap with the doped gain area. This can deteriorate the gain ratio between FM and HOMs. Hence, it is necessary to develop bendable LMA fibres for applications including but not limited to high power/energy scaling in CPA and beam combination systems.

There are several approaches that alleviate at least some of the detrimental bending effects. One example is a parabolic refractive index profile with modified cladding index structure with mode area of 1,000 $\mu m^2$ or higher [2]. In addition, an all-solid photonic bandgap fibre is reported to be bendable up to an effective area of 920 $\mu m^2$ [3]. Alternatively, an asymmetric core was investigated as a bendable LMA design. The semi-guiding high-aspect-ratio core (SHARC) is another proposed bendable LMA design [4]. One disadvantage with this approach is that the fibre has two sets of core-cladding boundaries and uses a very high aspect ratio (AR) (>30:1). This makes fabrication very challenging. More recently, a ribbon core fibre combining 13 small circular cores, parallel in a line, was fabricated through a stack-and-draw technique. The fibre was used to amplify a single HOM [5] for power scaling, and FM operation was demonstrated through external mode selection [6]. This improves the beam quality. The ribbon fibre is a type of multicore fibres in which the cores are coupled and placed in a line (“ribbon”) so that bending effects are negligible along a certain axis.

Here, we investigate mode area scaling and bending performances of a non-circular core fibre with a simpler structure than SHARC fibres and ribbon fibres. Our non-circular core fibres are similar to conventional double-clad fibres except that the cores are elongated instead of circular shapes. The shorter axis of the core is defined to suppress bending distortion at a desired maximum bending curvature. Here, we consider the bending radius of 25 cm (or bending curvature of 4 $m^{-1}$), which is useful for many applications and compatible with industrial packages. Bending effects can be greatly suppressed as long as the short core axis is in the bending plane. Meanwhile, there is a degree of freedom to stretch the orthogonal axis and scale the mode area by forming an elongated core resilient to bending distortion. We found

that the mode scaling of such fibres is limited by the beat length (BL) between the FM and HOMs. Still, in a fibre bent to 25 cm radius, according to simulations and within relevant assumptions, the fundamental mode area can be scaled to about 3000 μm$^2$ with a workable BL. Furthermore, we investigated the performance of such fibres incorporating also other techniques, i.e., confined doping and tandem-pumping [7] in our simulations. As shown in Ref. [7], tandem-pumping helps to ensure that most pump power is converted to the fundamental mode rather than HOMs, and therefore, a good beam quality at the output. By contrast, confined doping can be less effective in circular LMA fibres due to bending-induced shifts of the beam centre, if we rule out complicated pre-compensated refractive index profiles [8]. We focused on obtaining large mode areas in bent fibres.

Based on our analysis, a double-clad non-circular core fibre doped with Yb ions was fabricated with the conventional modified chemical vapor deposition (MCVD) process. The fibre was tested in a linear cavity pumped by a 975-nm LD. The highest signal power obtained was 191 W at 296 W of launched pump power. The corresponding slope efficiency was 67.2% with respect to the launched pump power. The measured $M^2$-factors were ~1.56 and 3.11 respectively, along the short and long core axis. The slightly worse $M^2$-factors along the long core axis is at least in part due to a deviation of the short axis from the bending plane.

## 7.3 Theoretical investigation of bending effects in asymmetric core

In a bent fibre, the mode distribution shifts toward the edge of the waveguide structure, and the corresponding mode area shrinks by an amount determined by the bending radius and fibre parameters [1]. The influence of bending on the FM effective area for rectangular cores with different aspect ratios (ARs) together with a circular core is presented in Figure 7.1. The core area is 10,200 μm$^2$, and the wavelength is 1080 nm in all cases. The core NA is assumed to be 0.06, which is achievable with MCVD with good yield and is commonly found in LMA fibres. The modes are calculated with COMSOL, using standard conformal mapping to treat the bending [9]. The FM areas of all fibres are slightly over 5,000 μm$^2$ when straight (e.g. 5,300 μm$^2$ in the circular core). The effective mode areas in the bent fibres are scaled by their straight-fibre values. The mode profiles in cores with ARs of one and ten are shown as well.

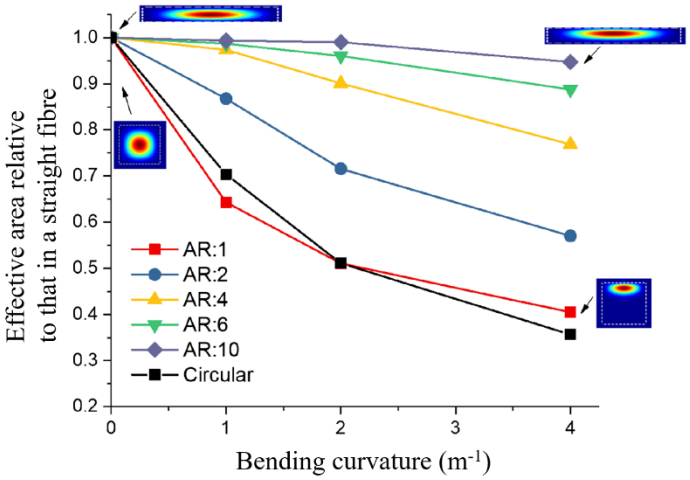


Figure 7.1: Dependence on bending (in the direction of the short axis) of the effective areas of the FM in fibres with different ARs. FM profiles for selected straight and bent fibre are also shown. A circular core with the same size is also plotted for comparison.

Similarly to the same size circular core, the mode area in the square core, i.e., with AR of one, quickly shrinks in the bent fibre. Figure 7.1 shows that at 4 $m^{-1}$ bending curvature, the effective area becomes only 41% of its straight counterpart. As the AR increases, the mode area shrinks less. In the fibres with the AR of six or above, the FM-area remains larger than 90% of the straight-fibre value at 4 $m^{-1}$ bending curvature. In addition to the mode-area shrinkage, the shift of the mode profile will change its overlap with the gain region, and degrade the gain of the FM relative to other modes. In the square core, the FM's intensity peak shifts about 37% relative to the core size. This makes mode-selection through confined doping ineffective. By contrast, the peak only moves 12% of the core at AR of 10, and 20% at AR of 6. We also note that if the fibre is bent in the orthogonal direction, i.e., with the long axis of the core in the bending plane, then the fibre with higher aspect ratio is more sensitive to the bending.

The core with AR of six has 41 μm short-axis height in Figure 7.1. As the bending performance is determined by the short axis when bent in the short axis plane, it is anticipated that the bending distortions and their impact would remain at the same level regardless of the long-axis size, or the ARs. In other words, the mode shrinkage and its peak shift should be invariant as long as the short axis is fixed at 41 μm and the bending radius at 25 cm. This is investigated in Figure 7.2 for AR in the range of 1–50 with a fixed short axis size of 41 μm. The mode shrinkage is indeed maintained around 10% for all ARs, including the square core. Furthermore, the mode peak shift is kept below 20% relative to the core height. The mode intensity profiles along the short axis at all ARs are shown in the inset of Figure 7.2. They all overlap and cannot be differentiated.

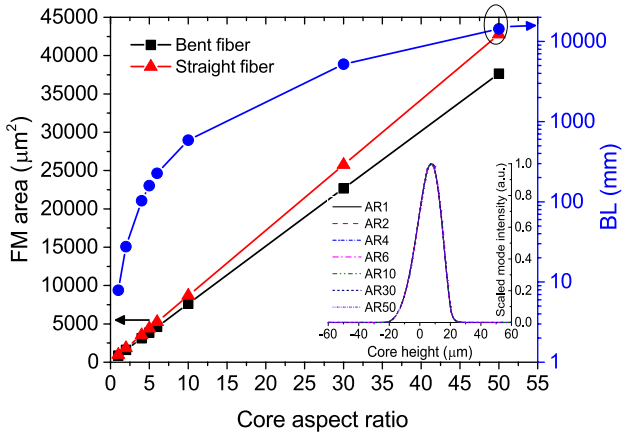


Figure 7.2: Mode area scalability of a rectangular core fibre with 41 μm core height in the short axis at different ARs. The bent fibre has a curvature of 4 $m^{-1}$. The beat length between the FM and the first HOM is also shown. Inset: mode intensity profiles at the investigated ARs along the short axis for bent fibre.

As shown in Figure 7.2, the mode area scales linearly with core AR at a fixed short axis. However, the increased AR also increases the BL between the FM and the first HOM as shown in Figure 7.2. The BL reaches even 1 m for the AR of 30. A BL of 1 m corresponds to modal index difference of $10^{-6}$. Then, eventually the modes are effectively degenerate, and coupling unavoidable in practice. Hence, mode area scaling in a rectangular core should consider beat length as well as the bending effects for robust FM operation. We will assume that a BL of ~100 mm is workable for single mode operation. A BL which we estimate is ~100 mm has been demonstrated in a straight LPF with 26 mJ output pulse energy, 100 W average power and nearly diffraction-limited output beam [10]. In another experiment with a coiled step-index fibre with a BL that we estimate to ~126 mm, the output beam was multimoded with measured $M^2$ of ~6.5 [11]. However, the beam can be improved, perhaps even to diffraction-limited quality, through techniques such as tandem pumping and confined doping to be discussed in the next section. Therefore, we target a similar BL, i.e., 100 mm, in our bent non-circular core fibres. This then limits the AR to 4, corresponding to a FM area slightly above 3,000 $\mu m^2$ at 1080 nm in a bent fibre. We note that this BL does not guarantee FM operation, but rather reduces coupling between modes so that the FM mode (as well as HOMs) are more distinguishable and easier to maintain. Then, confined doping promotes FM operation as discussed in the subsequent section. Selective bending loss [12, 13] would add further modal discrimination but is somewhat limited at the considered BL [11].

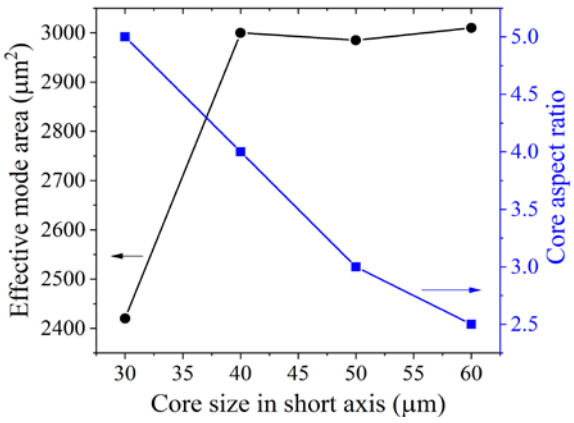


Figure 7.3: Achievable mode area at different short-axis core sizes. The core aspect ratio required for the mode area is presented as well. The fibre is bent at 4 $m^{-1}$ bending curvature.

We investigated mode area scalability in various short-axis lengths within the 100-mm BL constraint as presented in Figure 7.3. With increasing short axis lengths, the allowed core AR within the BL constraint is reduced. Furthermore, there is no significant benefit in enlarging the short axis above 40 μm in terms of mode area scaling. Instead, a larger short axis core experiences larger bending distortions at the target bending curvature. For instance, a 50 μm short axis core suffers 23% of mode shrinkage and 24% of peak shift which are worse than the 41 μm short axis core. Consequently, a core with 41 μm short axis with an AR of 4 well represents the achievable mode area at the bending curvature of 4 $m^{-1}$.

## 7.4 Fundamental mode selection by confined doping and tandem pumping

The low bend-distortion in a rectangular core facilitates the use of confined doping to preferentially amplify the FM. It is also known that tandem pumping can reduce HOM gain when the FM gain is saturated [7]. We theoretically study the benefit of confined doping and tandem pumping in the rectangular core fibre. We follow the theoretical analysis in [7] to investigate the modal gain ratio when the FM gain is assumed saturated with an average Yb excitation level across the signal mode of 3%. For the high-power devices we consider, the pump and stimulated-emission rates dominate over the spontaneous-emission rate. ASE and spontaneous emission are assumed not to influence the ion excitation, which is instead determined by only the pump and signal power. In this case, if the ratio $P_s/P_p$ is constant along the fibre, the excitation level will not change along the fibre. This situation is a good approximation of a saturated amplifier with counter-propagating pump and signals, if the operating pump absorption and signal gain are approximately equal. Then, in the absence of

loss, the number of pump photons will be equal the number of signal photons in each cross-section of the fibre.

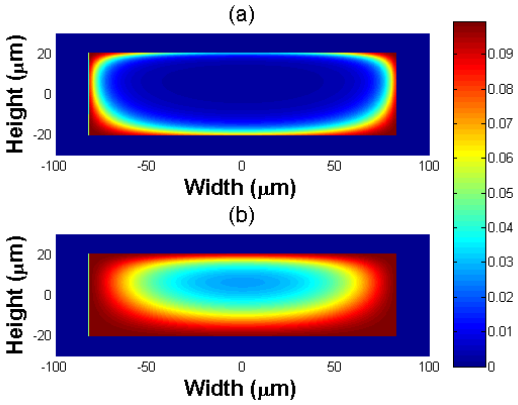


Figure 7.4: Fractional Yb excitation level inside uniformly doped fibre core at 4 $m^{-1}$ bending curvature. The core height is 41 μm. Pump wavelength (a) 915 nm and (b) 1020 nm. The core aspect ratio is 4:1 with 41 μm core height. White lines indicate the core boundary.

Figure 7.4 shows the excitation level in a rectangular core fibre, uniformly Yb-doped throughout the core, when pumped at two typical wavelengths, i.e. 915 nm for diode laser pumping, and 1020 nm for tandem pumping. The signal wavelength is assumed at 1080 nm. The cladding area is adjusted for an average fractional excitation of 0.03. It leads to 0.96 dB/m of pump absorption corresponding to Yb ion concentration of 2% by weight in a P-doped silica core. In a P:Yb silica fibre, photodarkening can be negligible [14]. The same pump absorption level is obtainable in other host materials, e.g. alumino-silicate glass, by controlling the doping level and cladding size. In accordance with the analysis in Section 7.3, the fibre core has a 0.06 NA, a 4:1 AR, and a 41 μm short axis length. The white lines in Figure 7.4 show the edge of the core. The fibre is bent to 4 $m^{-1}$ curvature. As expected from [7], the Yb ion inversion is more uniformly distributed across the core under 1020 nm pumping compared to that with diode-pumping at 915 nm. The inversion in the edge under 915 nm pumping would be up to 24 times larger than the average inversion level, which can result in unwanted high gain in HOMs. On the other hand, under 1020 nm pumping, the highest edge inversion is only three times higher than the average inversion. Hence, in a uniformly doped rectangular core, tandem pumping can help avoid undesired high gain in HOMs.

The ratio between the highest gain in HOMs and the FM gain is calculated for different fractional doping areas, with LD-pumping at 915 and 975 nm, and tandem-pumping at 1020 and 1030 nm. The same core parameters and the same bending are assumed as in Figure 7.4. The results are shown in Figure 7.5. It is clear that confined doping works well, and the gain ratio is improved by reducing the confined doping ratio at all investigated pumping

wavelengths. The FM gain becomes higher than that of any HOM for doping area ratios in the range of 0.1–0.4 for both tandem-pumping and diode-pumping. For larger doped areas, the HOM gain exceeds the FM gain in all pumping schemes. Nonetheless, tandem-pumping has a more favourable, lower gain ratio. In the uniformly doped core, the highest HOM gain is only 1.7 and 2.3 times larger than the saturated FM gain of 0.96 dB/m for 1030-nm and 1020-nm pumping, respectively.

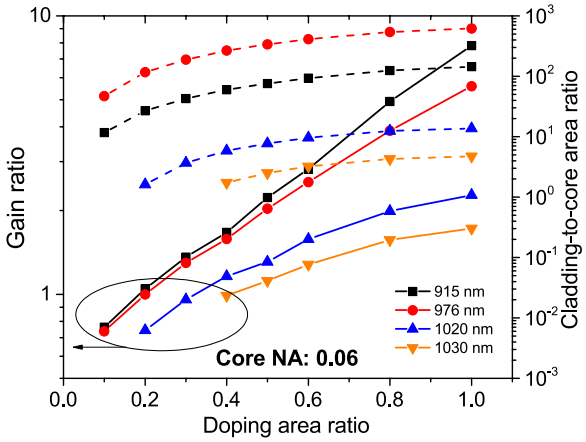


Figure 7.5: Calculated gain ratio between the HOM with highest gain and the FM at different doping area ratios for different pumping wavelengths. The core NA is 0.06. Bent fibre with 0.25 $m^{-1}$ curvature is assumed. The required cladding-to-core area ratio is also plotted for the assumed 0.03 inversion level.

We note that the tandem pumping should be accompanied with a small cladding-to-core area ratio as shown in Figure 7.5. This requirement can be fulfilled with high brightness pumping sources such as fibre laser. The calculation stops when the required cladding-to-core area ratio becomes smaller than one because it is unachievable. The pump area is adjusted to different doping ratios to keep the same average excitation level of 3% for all cases. When the doping ratio becomes smaller, a smaller cladding-to-core area ratio is necessary.

We now consider the benefit and practicability of confined doping together with diode laser pumping. The gain ratio improves nearly an order of magnitude with confined doping as shown in Figure 7.5. With 0.1 doping area ratio, the FM sees the highest gain among the supported modes. However, this requires cladding-to-core area ratio of 10 at 915 nm pumping or 50 at 976 nm pumping to reach 0.96 dB/m gain. With a doping area ratio of 0.2, the FM gain is still higher than HOMs under 976 nm pumping, and its required cladding-to-core area ratio is 110, which is practical for aspects of fabrication as well as available pump brightness [15].

We next extend our investigation to a larger core NA to see if rectangular cores with confined

doping is useful for highly doped fibres. It is worth noting that in addition to the Yb-doped fibres considered here, Tm-doped fibres are often highly doped to allow efficient 2-for-1 cross-relaxation [16]. The highly doped core inevitably raises a refractive index, which subsequently requires compensation of the raised index to control beam quality. A pedestal design [17] and an equi-molar Al:P [18] core were proposed in prior works. Confined doping could be an alternative option for controlling the beam quality in a raised refractive index. To investigate this possibility, a core NA of 0.15 is chosen, which allows us to increase the short-axis size to 45 μm without significant bending distortion. This short-axis core size keeps the FM distortion small, i.e. 87% of the mode area is preserved and the mode peak shift is only 12% of the short-axis core size. With the core AR of 4, the beat length becomes 119 mm, and further area scaling is not considered. The same bending curvature as in Figure 7.4 is assumed.

The gain ratio calculated for the fibre with core NA 0.15 is presented in Figure 7.6. For the AR of 4, the FM area is 3,330 $\mu m^2$. It is found that confined doping is effective for controlling the gain ratio when the fibre is bent. Similar to Figure 7.5, under the diode laser pumping, the gain ratio is improved by an order of magnitude when the doping changes from uniform throughout the core to 0.1 doping area ratio. Again, tandem pumping improves the gain ratio in the high NA core as observed in the 0.06 core NA.

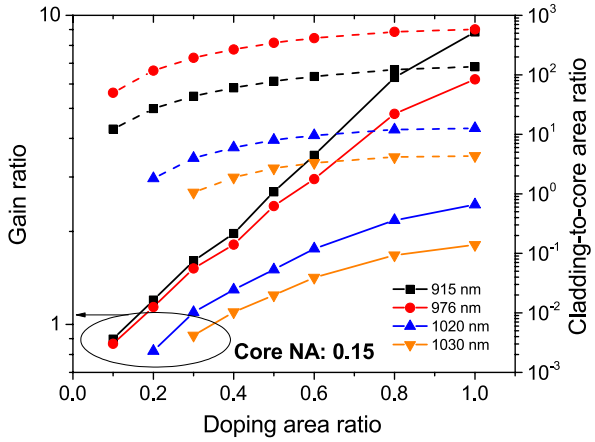


Figure 7.6: Calculated gain ratio between the HOM with highest gain and the FM at different doping area ratios under various pumping wavelengths. The core NA is 0.15. Bent fibre with 0.25 $m^{-1}$ curvature is assumed. A required cladding-to-core area ratio is also plotted for the assumed 0.03 inversion level.

The confined doping looks promising as long as the fibre bends in the intended plane of the shorter axis. It is interesting to see its performance when the bending plane deviates from the intended. The effect of the bending orientation offset is investigated at 915 and 1020 nm pumping. Figure 7.7 shows the calculated bending distortion with the offset angle between the bending plane and the core short axis. The fibre parameters are the same as in Figure 7.5. The

performance is notably affected by the orientation deviation. The FM area reduces to 67% of its original value for an angle of 3°. The gain ratio is also impaired by the angle offset, although the impact becomes weaker with tandem-pumping than with LD-pumping. With a doping area ratio of 0.2, the gain ratio becomes 3.9 times at 915 nm pumping with a 3° offset, compared to 1.5 times at 1020 nm pumping. In the uniformly doped core, the gain ratio becomes less sensitive to the bending angle offset although its gain ratio is always larger than in the confined doping case.

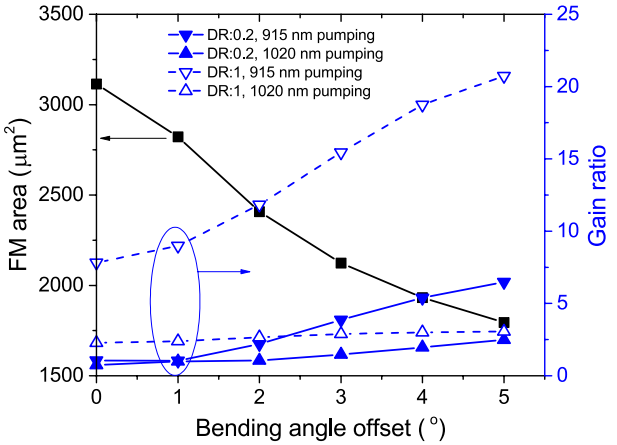


Figure 7.7: Bending performance against bending angle offset. The fibre parameters are the same as in Figure 7.4. DR: Doping area ratio.

## 7.5 Fibre characterization

According to the design suggested by simulations in the previous two sections, a bendable non-circular core LMA YDF was fabricated at NTU with a laterally stretched core and confined doping. Figure 7.8 represents the refractive index profile (RIP) of the preform before core shaping. The Yb ions are doped only in the centre of the core as indicated by the shaded area. The doping area ratio is 0.2. The core refractive index is raised, the corresponding core NA reaches 0.066. We noticed a slight refractive index deviation of 0.0003 between the doped and the undoped region in the core. The slight deviation could be further reduced through MCVD process optimization. A slight refractive index dip in the core's centre helps to compensate the index deviation. A stretched-core fibre was drawn to 41 and 120 μm short and long core axis lengths, respectively. The fibre was coated with a low refractive index polymer to form a pump waveguide in the cladding with nominal NA of 0.45. The cladding was milled to double D-shape to improve pump absorption as well as control the bending axis. Its cladding long axis and short axis were 760 μm and 585 μm, respectively. When bent, the double D-shaped fibre naturally bends in the intended shorter axis plane as the fibre is thinner along the shorter axis.

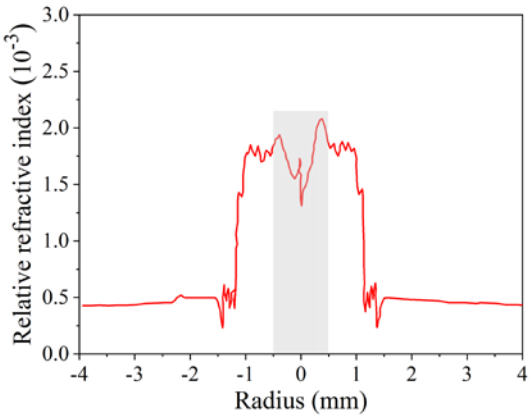


Figure 7.8: Refractive index profile of confined doping fibre preform. The shaded area indicates the Yb doped region. Its doping area ratio is 0.2.

With the 41 μm short axis, the fibre is designed to be bent to a radius of up to 25 cm. Also, as evident from Figure 7.2, with the core AR of 3, the fabricated fibre has BL between FM and close HOM of around 58 mm, shorter than 100 mm. The FM mode area is estimated to 2,571 $\mu m^2$. With the fabricated area doping ratio of 0.2, and the cladding-to-core area ratio of about 100, the FM is expected to see higher gain than HOMs if pumped by 915 nm LDs as shown in Figure 7.5. A microscope image of the fibre is shown in Figure 7.9. The small-signal absorption in the pump waveguide was measured to 1 dB/m at 976 nm. The Yb concentration is estimated to 0.2% by weight.

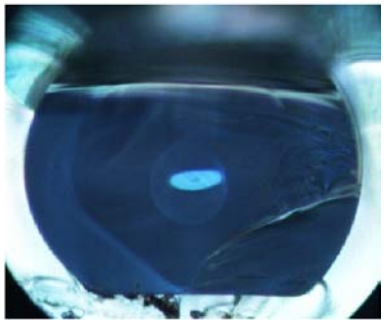

Figure 7.9: Fabricated stretched core fibres with a core aspect ratio of 1:3 with 41:120 μm.

Ideally, the milled edge of the cladding should be parallel to the longer core axis. However, for the fabricated fibre, the longer core axis is not perfectly parallel to the milled edge of the cladding, which induces an orientation between the intended and actual bending planes. The deviation angle for the fibre used in the experiment is estimated to be ~3º. As discussed in the previous section, the angle deviation can cause beam distortions and therefore degrade the output beam quality. Our laser experiments described in the next section explore this.

## 7.6 Laser experiment

Figure 7.10 shows the schematic diagram of the experimental setup for the laser slope efficiency and beam quality measurements. A 976-nm pump-LD was free-space coupled into a 20-m-long fibre through a dichroic mirror (DM). Both ends of the fibre were perpendicularly polished to work as laser cavity mirrors through 4% Fresnel reflections. Thus, the laser output was bi-directional. Wedges were used to sample the forward signal for beam quality measurement, following reflection in another DM. Both DMs have high transmission around 975 nm and high reflection around 1.06 μm.

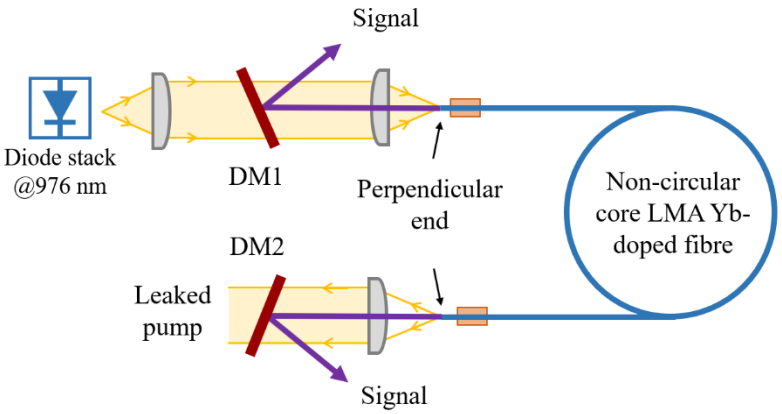


Figure 7.10: Schematic of the experimental setup for laser slope efficiency and beam quality measurements. DM: dichroic mirror.

Firstly, the laser output power (black squares) and pump residual power (red circles) were characterized with the increase of the pump power as shown in Figure 7.11. During the measurements, the fibre was bent along its short axis with the bending diameter of 95 cm. As shown in Figure 7.11 (a), the signal power increases nearly linearly with the pump power. The highest power of the signal was 191 W, obtained at 296 W launched pump power. The output power is only limited by the available pump power. There is no sign of the onset of nonlinear effects to limit the output signal power. This is confirmed with the laser output spectrum measurement at full power, which is given in Figure 7.11 (b). The lasing spectrum extends from 1040 nm to 1090 nm. With higher pump power, the output signal power can be expected to be further increased. The slope efficiency against the launched pump power is 67.2%. Note that the leaked pump power dropped, and the slope efficiency increased, when the launched pump power exceeded 150 W. This is because the pump wavelength drifts to longer wavelengths with higher absorption when the pump power increases.

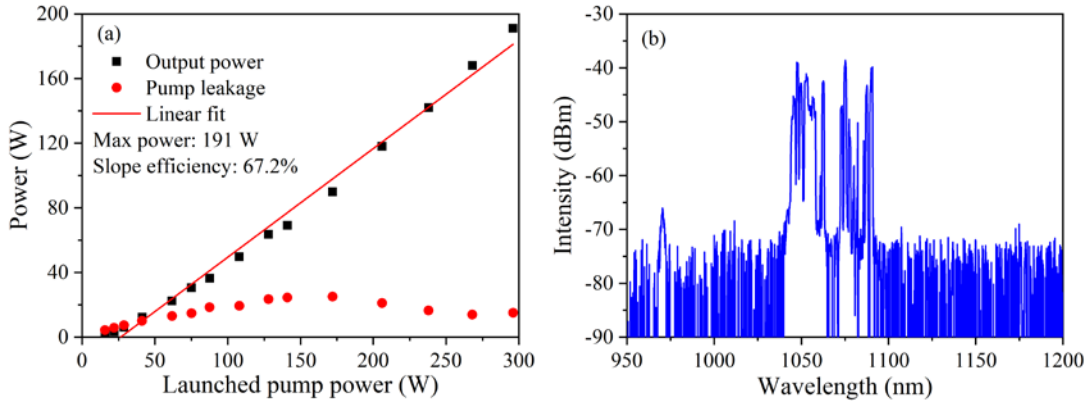


Figure 7.11: (a) Output powers of signal and residual pump *vs.* launched pump power and (b) laser output spectrum at 191 W signal power with 1.0 nm resolution.

We also measured the beam quality of the output signal with a scanning-slit beam profiler (Thorlabs BP104-IR), adopting the 4σ method and the hyperbolic fit algorithm of the profiler. The fibre was bent along its short axis with 90-cm bending diameter. Figure 7.12 shows the measured results of the $M^2$-factors at different launched pump powers. The average values of $M^2$-factors along short axis (or x-axis) and long axis (or y-axis) are 1.56 and 3.11, respectively. As the $M^2$ fitting curve shown in Figure 7.12 (b), I found that the beam widths in the fibre x and y are 67 μm and 60 μm, respectively. This proximity can be attributed to the confined doping area deviation, though the fibre has a core AR of 3. For a step-index fibre, the relationships between fibre parameters, normalized frequency, $V$ and $M^2$-factor are given by the following two equations if all core modes are equally excited and mutually incoherent:

$$V_{x(y)} = \frac{2\pi r_{x(y)} \cdot NA}{\lambda}, \tag{7.1}$$

$$M^2_{x(y)} = \frac{V_{x(y)}}{2}, \tag{7.2}$$

where $r$ and $NA$ are radius and numerical aperture of the fibre core, respectively, and $\lambda$ is the wavelength. The $M_x^2$ and $M_y^2$ of the fibre core are estimated to be 7.99 and 22.21, respectively. Compared to these theoretical values, the measured $M^2$-factors are much smaller. The HOMs are well suppressed, which we attribute at least in part to the confined doping. Therefore, the beam qualities are better than the values given by Equations (7.1) and (7.2) in the case that all modes are equally excited. Even better beam qualities are expected if there is no misalignment between the longer core axis and the milled edge of the cladding.

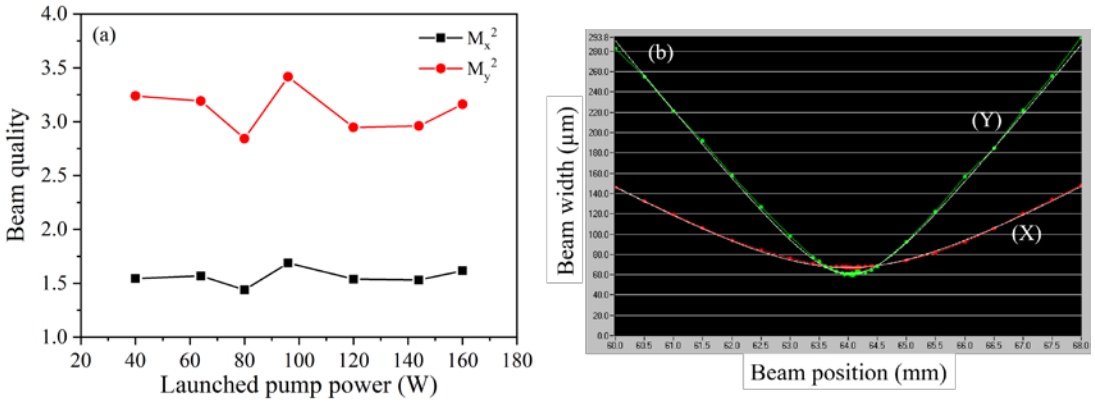


Figure 7.12: (a) Measured beam quality $M^2$-factors at different pump powers and (b) $M^2$ fitting curve at the maximum power.

The beam qualities were also measured at 60 cm and 110 cm bending diameters to further verify whether the designed fibre is capable of suppressing the bending effects. The measured $M^2$-factor results with different bending diameters (60 cm, 90 cm and 110 cm) are plotted in Figure 7.13. Once again, when the bending diameter is fixed, the beam quality factors along both x and y axes remained almost the same with the increase of launched pump power. The $M^2$-factors are very close to each other at 90 cm and 110 cm bending diameters. At the same laser output power, the beam quality with 110 cm bending diameter is slightly better than that with 90 cm bending diameter. When the fibre was tightly bent at 60 cm bending diameter, the beam qualities became worse. For example, $M^2$-factors along x-axis and y-axis degraded from 1.753 to 2.116 and from 3.442 to 4.449 with a bending diameter reduced from 110 cm to 60 cm. The 60-cm bending diameter is close to the designed minimum bending diameter, i.e., 50 cm.

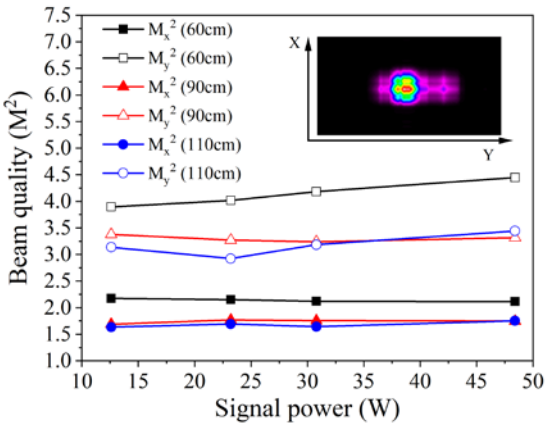


Figure 7.13: Beam quality $M^2$-factors with different bending diameters (60 cm, 90 cm and 110 cm) at different signal powers.

The non-circular core fibre is designed to bend along the short axis, and deviations from this can induce considerable bending distortion. The effect of the bending distortion with the deviation has been simulated and is given in Figure 7.7. It shows that the FM area with 3º

angular error is reduced to 67% of its mode area bent in short axis plane. The misalignment angle between the core and short axis is estimated to be 3º. The inset of Figure 7.13 shows the mode distribution at the maximum output power with 90 cm bending diameter. That means the misalignment between the core and the cladding axes of this fibre sample will enlarge the bending distortions. With even smaller bending diameter, e.g., 60 cm, more power will be seen in the side lobe. The beam quality along the long core axis will further degrade. This bending-induced distortion might also explain the somewhat limited slope efficiency in Figure 3.11 (a). The post-processing introduced a slight twist of core in a preform, and this could not be recovered. However, we believe that employing 3D computer numerical control (CNC) machining for the D-shaping can minimize the misalignment between the core and cladding. CNC can allow the preform to be shaped precisely to the core axis along the preform. We also note that the asymmetric core may induce a polarisation effect, particularly for HOMs [19]. This could be examined in other contexts.

## 7.7 Conclusion

Non-circular elongated-core fibres are investigated as a bendable LMA design. We propose a design approach to reach the maximum achievable mode area at a desired bending curvature, under the constraint of a maximum beat length between FM and HOM. According to simulations, a mode area of 3,000 $\mu m^2$ is found achievable at 4 $m^{-1}$ of bending curvature within 100 mm beat length. Selective doping in the rectangular core is found effective to promote single mode operation in the 3,000 $\mu m^2$ mode area. Preferential gain for the FM is achieved at diode laser pumping as well as tandem pumping. This approach is also effective in high core NA fibre with high rare-earth concentration.

The fabricated fibre exhibited efficient laser performance with 67% of slope efficiency and nearly 200 W output power, only limited by the available pump power. Its beam quality factor was measured about 1.5 and 3.1, respectively along short axis and long axis, indicating HOM excitation during the laser operation. We attributed this HOM excitation to the offset bending angle. Better beam quality factor should be achievable if this deviation-induced bending distortion is avoided. However, we believe that this initial result also provides a proof of the applicability of this bendable non-circular core LMA fibre in single-mode, high-energy ultrafast pulse amplification.

## References


[1]. J. M. Fini, “Bend-resistant design of conventional and microstructure fibers with very large mode area”, Opt. Express **14**, 69 (2006).

[2]. J. Fini and J. Nicholson, “Bend compensated large-mode-area fibers: achieving robust single-modedness with transformation optics”, Opt. Express **21**, 19173 (2013).

[3]. F. Kong, K. Saitoh, D. Mcclane, T. Hawkins, P. Foy, G. Gu, and L. Dong, “Mode area scaling with all-solid photonic bandgap fiber”, Opt. Express **20**, 26363 (2012).

[4]. J. R. Marciante, V. V. Shkunov, and D. A. Rockwell, “Semi-guiding high-aspect-ratio core (SHARC) fiber amplifiers with ultra-large core area for single-mode kW operation in a compact coilable package”, Opt. Express **20**, 20238 (2012).

[5]. D. Drachenberg, M. Messerly, P. Pax, A. Sridharan, J. Tassano, and J. Dawson, “First multi-watt ribbon fiber oscillator in a high order mode”, Opt. Express **21**, 18089 (2013).

[6]. B. Anderson, G. Venus, D. Ott, I. Divliansky, J. W. Dawson, D. R. Drachenberg, M. J. Messerly, P. H. Pax, J. B. Tassano, and L. B. Glebov, “Fundamental mode operation of a ribbon fiber laser by way of volume Bragg gratings”, Opt. Lett. **39**, 6498 (2014).

[7]. C. A. Codemard, J. K. Sahu, and J. Nilsson, “Tandem cladding-pumping for control of excess gain in ytterbium-doped fiber amplifiers”, IEEE J. Quantum Electron. **46**, 1860 (2010).

[8]. J. Fini, “Design of large-mode-area amplifier fibers resistant to bend-induced distortion”, J. Opt. Soc. Am. B **24**, 1669 (2007).

[9]. D. Marcuse, “Influence of curvature on the losses of doubly clad fibers”, Appl. Opt. **21**, 4208 (1982).

[10]. F. Stutzki, F. Jansen, A. Liem, C. Jauregui, J. Limpert, and A. Tünnermann, “26 mJ, 130 W Q-switched fiber-laser system with near-diffraction-limited beam quality”, Opt. Lett. **37**, 1073 (2012).

[11]. M.-Y. Cheng, Y.-C. Chang, A. Galvanauskas, P. Mamidipudi, R. Changkakoti, and P. Gatchell, “High energy and high peak power nanosecond pulse generation with beam quality control in 200-μm core highly multimode Yb-doped fiber amplifiers”, Opt. Lett. **30**, 358 (2005).

[12]. J. P. Koplow, D. A. Kliner, and L. Goldberg, “Single-mode operation of a coiled multimode fiber amplifier”, Opt. Lett. **25**, 442 (2000).

[13]. Y. Jeong, J. K. Sahu, D. N. Payne, and J. Nilsson, “Ytterbium-doped large-core fiber laser with 1.36 kW continuous-wave output power”, Opt. Express **12**, 6088 (2004).

[14]. J. K. Sahu, S. Yoo, A. Boyland, C. Basu, M. Kalita, A. Webb, C. L. Sones, J. Nilsson, and D. N. Payne, “488 nm irradiation induced photodarkening study of Yb-doped aluminosilicate and phosphosilicate fibers”, in Conference on Lasers and Electro-Optics/Quantum Electronics and Laser Science Conference and Photonic Applications

Systems Technologies (Optical Society of America, 2008), paper JTuA27.

[15]. Y. Feng, P. G. R. Hernández, S. Zhu, J. Wang, Y. Feng, H. Lin, O. Nilsson, J. Sun, and J. Nilsson, “Pump absorption, laser amplification, and effective length in double-clad ytterbium-doped fibers with small area ratio”, Opt. Express **27**, 26821 (2019).

[16]. P. F. Moulton, G. A. Rines, E. V. Slobodtchikov, K. F. Wall, G. Frith, B. Samson, and A. L. G. Carter, “Tm-Doped Fiber Lasers: Fundamentals and Power Scaling”, IEEE J. Sel. Top. Quantum Electron. **15**, 85 (2009).

[17]. S. Yoo, A. S. Webb, A. J. Boyland, R. J. Standish, A. Dhar, and J. K. Sahu, “Linearly polarised ytterbium-doped fiber laser in a pedestal design with aluminosilicate inner cladding”, Laser Phys. Lett. **8**, 453 (2011).

[18]. J. K. Sahu, S. Yoo, A. J. Boyland, A. Webb, C. Codemard, R. J. Standish, and J. Nilsson, “Ytterbium-doped low-NA P-Al-silicate large-mode-area fiber for high power applications”, in Conference on Lasers and Electro-Optics/Quantum Electronics and Laser Science Conference and Photonic Applications Systems Technologies (Optical Society of America, 2010), paper CTuP3.

[19]. A. W. Snyder and W. R. Young, “Modes of optical waveguides”, J. Opt. Soc. Am. **68**, 297 (1978).

# Chapter 8
# Power-scaling of erbium-doped fibre lasers

## 8.1 Overview

The phase distortions including their size and temporal response have been investigated in narrow-line pulsed, chirped pulse, and broad bandwidth YDFAs at 1.0–1.1 μm. We believe that it is also of interest to consider them at other wavelengths (e.g., 1.5–1.6 μm) for several reasons. On the one hand, the nonlinearities and phase errors are wavelength dependent, which means that the nonlinear phase error becomes smaller at longer wavelengths. In other words, it would be easier to do pulse phasing at longer wavelengths. Meanwhile, it should be noted that other nonlinear phase distortion effects, e.g., quantum-defect induce heating might be more significant. In addition, certain applications require longer wavelengths. For example, the high harmonic generation (HHG) is better driven at longer wavelengths [1]. Furthermore, with the development of power-scaling in YDFs, TMI is receiving considerable attention but not in EDFs. Here, we have explored EDFs in power-scaling (experimentally CW) and assessed their potential performance theoretically.

This chapter is divided into two major parts. The first part describes a record power large-core Er-doped fibre laser, as detailed in Section 8.2. A brief review of the development and relevant limitations of high-power erbium-doped fibre lasers is firstly introduced, followed by a description of the fibre fabrication and characterization parameters, and the laser experiment. The experimental result, discussion and further analysis are also presented in this section. In another part (Section 8.3), it shows our effort on an Er-nanoparticle-doped Yb-free fibre, which is fabricated with a high-concentration nanoparticle doping method. In this section, I review the nanoparticle doping technique and its advantages compared to the traditional solution doping technique. Based on this nanoparticle doping method, a fibre was designed and fabricated to explore its potential high-power operation. Finally, the achieved results and findings on further power scaling potential are summarized in Section 8.4.

## 8.2 Record power large-core Er-doped fibre laser

### 8.2.1 Introduction

Recent years have seen significant progress in the power of cladding-pumped ytterbium-doped fibre lasers operating at 1.0–1.1 μm [2]. There is also great interest in high-power erbium-

doped fibre lasers emitting at 1.5–1.6 μm, due to their relative eye-safety and the atmospheric transparency [3]. Pumping of mid-infrared laser sources is another application, and they may also be useful for high harmonic generation. However, owing to spectroscopic differences between Er and Yb ions, the power of EDFLs has lagged far behind that of Yb-doped ones. Specifically, it is difficult to cladding-pump EDFLs, since the small absorption cross-section and concentration quenching [4] make it difficult to reach adequate pump absorption. One approach to overcoming this is to co-dope ("sensitize") with Yb, which absorbs the pump energy before it is transferred to the Er-ions. Such Er:Yb co-doped fibre lasers (EYDFLs) can be cladding-pumped by efficient 0.9–1 μm diode lasers and have been scaled to 297 W of output power [5], which is the highest power reported to date. However, the onset of parasitic Yb-lasing at 1–1.1 μm as well as a high thermal load impede further power scaling. Furthermore, to promote efficiency, the host glass is doped with high concentrations of rare earth and phosphorus [6]. This leads to high NA, which degrades the beam quality. However, CPA and CPSA require single-mode operation. High-efficiency in-band cladding-pumping of Er-doped fibres with 1535-nm EYDFLs is an alternative approach. This way, an output power of 264 W was obtained [7]. Although the 264-W laser was also co-doped with Yb, this played no part in the laser cycle. Indeed, the approach has also been used with Yb-free EDFLs, pumped by 1535-nm EYDFLs as well as by 1480-nm fibre Raman lasers. The high pump brightness of this so-called tandem-pumping approach [8], in which a fibre laser pumps another fibre laser, allows for a small inner cladding, which increases the pump absorption. Even core-pumping is possible, through which over 100 W of output power has been generated [9]. However, tandem-pumping significantly increases system cost and complexity.

Therefore, although challenging, cladding-pumping directly with diode lasers remains an attractive alternative for Er-doped Yb-free fibre lasers. This approach has been pursued with 1.5-μm pump diodes, which offer a low thermal load in the EDFL as one attraction. Unfortunately, however, multimode 1.5-μm pump diodes lag their 0.9–1-μm counterparts in power as well as efficiency. Thus, the highest output power of 88 W from an EDFL in-band-pumped by diodes was limited by the available diode laser power at 1.53 μm [10]. In addition, despite the high optical-to-optical efficiency that can be achieved with in-band pumping, the overall efficiency suffers from the low efficiency of 1.5-μm pump sources. As a result, the overall electrical-to-optical efficiency may well be below 15% [11].

Alternatively, it is also possible to cladding-pump Yb-free EDFLs with diode lasers at 0.98 μm. This was investigated in the 1990's by Minelly *et al.* [12] and has since then reached 103 W of output power [13]. Furthermore, 0.98-μm pump diodes can reach several kW of power, which opens up for kW-level EDFLs. However, to accommodate such pump sources requires

a relatively large inner cladding. An option for maintaining adequate pump absorption is then to also scale the core size. Indeed, an Er-doped fibre with core diameters as large as 73 μm has been reported [14], focusing on scaling of pulse energy rather than of average power. Such large cores are expected to degrade the beam quality, which needs to be rectified for CPA and CPSA, but this may still be acceptable for some applications, e.g., pumping of Tm-doped fibre sources, including ultrafast pulse sources, emitting at ~2 μm.

In this section, I present an Er-doped Yb-free fibre laser cladding-pumped by 0.98-μm diode lasers, with record-breaking output power from any Er-doped fibre source. For this, a tailored Er-doped fibre with 0.7-mm inner cladding has been designed and fabricated to suit our pump source, a modest Er-concentration to avoid quenching, a large 146-μm-diameter core to improve the pump absorption, and a 36-m length to absorb the pump and distribute the thermal load. I used a simple bi-directionally end-pumped configuration with up to 1910 W of launched pump power and reached 656 W of output power centred at 1601 nm with 35.6% slope efficiency *vs.* launched pump power. There was no roll-off and the output power was only limited by the available pump power.

### 8.2.2 Fibre characterization and experimental setup

An Er:Al doped silica preform was designed and fabricated in-house by the standard modified chemical-vapor deposition (MCVD) and solution doping technique [6]. Figure 8.1 shows the refractive index profile of its 1.6-mm diameter core. The preform was milled to 5.7% of the diameter into a “D-shape” in order to improve the pump absorption and then drawn to a fibre (A1028-L10552) with a core diameter of 146 μm and a numerical aperture (NA) of 0.08 (V = 23 at 1.6 μm). The inner cladding had a diameter of 660 μm (round-to-flat) and 700 μm (round-to-round) to suit the pump source. The pump brightness was estimated to ~0.008 W/μm$^2$·sr, which is much lower than that of a state-of-the-art commercial diode laser with 200 W from a 105/125 μm fibre pigtail and 95% of the power within 0.15 NA (~0.3 W/μm$^2$·sr). The fibre facet images at the beginning of the pull are shown in Figure 8.2. The fibre was coated with a low-refractive-index polymer which provides a nominal inner-cladding NA of 0.48. The inner-cladding small-signal absorption was measured to ~0.45 dB/m at the 979-nm peak. Based on these data, the $Er^{3+}$-concentration was estimated to $1.2\times10^{25}$ ions/m$^3$.

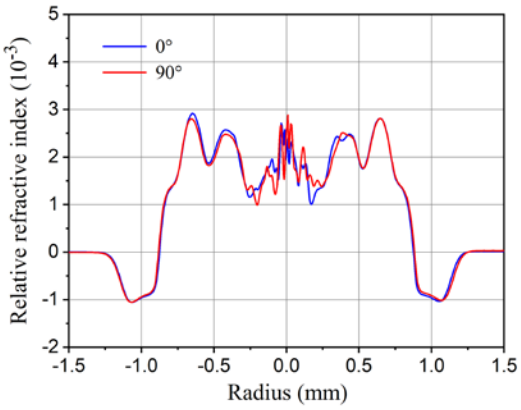


Figure 8.1: Refractive index of the Er:Al doped preform (measured in orthogonal directions, 0 and 90 degrees).

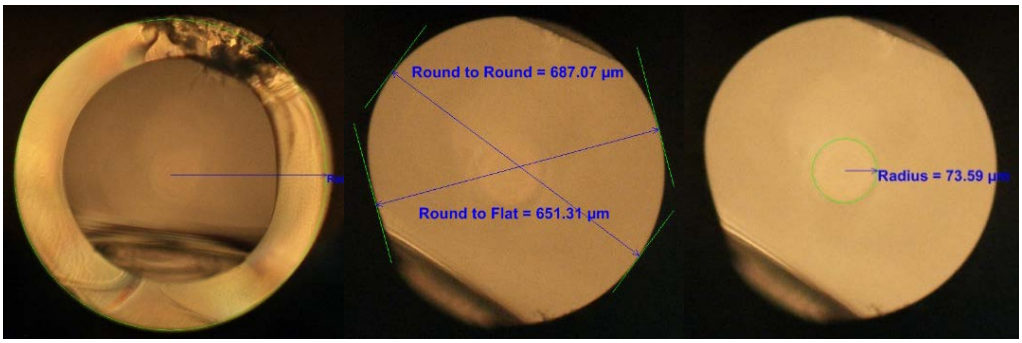


Figure 8.2: Fibre facet images at the beginning of the pull.

The experimental laser configuration is depicted in Figure 8.3. Although the fibre was 36-m long, the operating pump absorption was initially only ~5 dB, which I attribute to the relatively modest "D-shaping" of the inner cladding. Therefore, I coiled the fibre into a figure-eight shape with diameter ~23 cm to scramble the pump-modes, which improved the pump absorption to ~11 dB (92%). I used three 1.1-kW diode-laser-stack-based sources (Laserline LDL 80-1000) centred at 977 nm and with 3-dB linewidth of 4 nm to pump the fibre through both of its ends, via a combination of lenses and dichroic mirrors. In one end of the fibre, two of the pump sources were spatially beam-combined (incoherently) into one beam. In each pump pathway, an aperture with suitable size was arranged to filter out pump light with excessive NA and thus prevent potential coating failure. The launch efficiency was ~73% in the beam-combined end and ~87% in the other end for a total pump launch of up to 1.91 kW. Both ends were polished perpendicularly to the fibre axis. At the end of the laser cavity with a single pump source, high-reflectivity feedback was provided by a pair of dichroic mirrors having high transmission for the pump and high reflection for the signal. The laser output coupler was formed by the 3.5%-reflecting facet in the other end of the fibre. The out-coupled signal was separated from the pump beam by another dichroic mirror having the same characteristics as the feedback mirrors. Both fibre ends were held in temperature-controlled

metallic V-grooves, matched to the fibre size and designed to prevent thermal damage to the fibre coating by any non-guided pump or signal power, or by the heat generated in the laser cycle. Furthermore, the bulk of the fibre was coiled on metal cylinders and air-cooled by fans, albeit with a total of ~1 m of the fibre between the v-grooves and metal cylinders suspended in air.

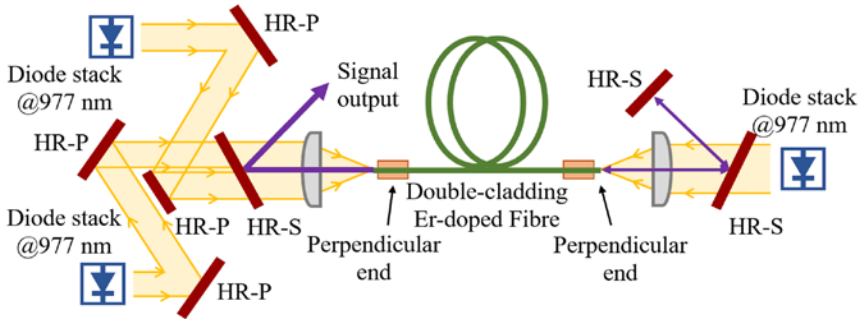


Figure 8.3: Schematic of the Er-doped fibre laser. HR-P: high reflectivity for pump, HR-S: high reflectivity for signal.

### 8.2.3 Experimental results and discussions

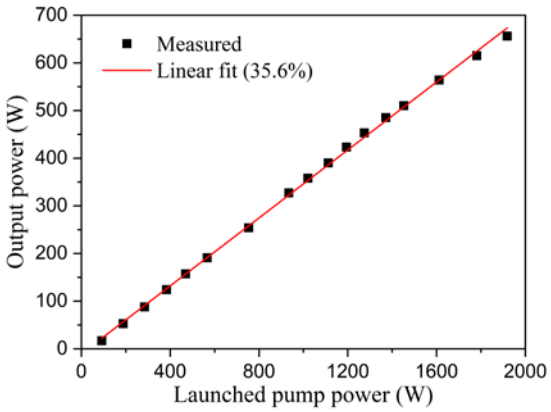


Figure 8.4: Laser output power *vs.* launched pump power.

The laser output power as a function of the launched pump power is shown in Figure 8.4. The maximum output power was 656 W with slope efficiency 38.7% with respect to absorbed pump power and 35.6% with respect to launched pump power. The output power increased linearly with pump power and showed no roll-off. The average thermal load at full power was 30 W/m, calculated from the difference between absorbed pump power and generated output power. The output spectrum measured by an OSA at full power is plotted in Figure 8.5. It was centred at 1601 nm and had a 3-dB linewidth of 4.2 nm. The fraction of ASE was 0.2%, integrated from the recorded spectrum.

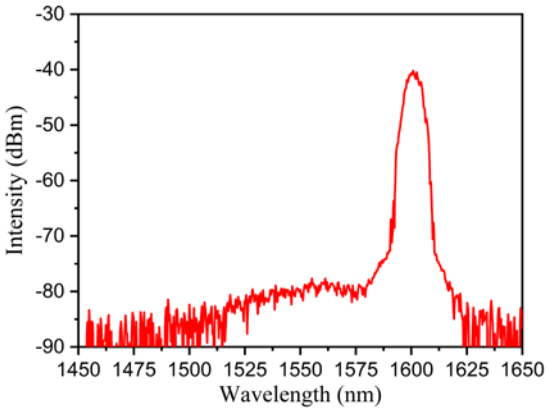


Figure 8.5: Optical spectrum at 656 W output power, resolution: 1 nm.

In initial experiments [15], pulsing caused the fibre ends to fail. The temporal-power characteristics were monitored using a 460-kHz photodetector (Thorlabs PDA100A-EC) and an oscilloscope, and showed a series of high-intensity pulses at irregular intervals. In erbium-doped fibre lasers, such behaviour can be caused by clustered erbium ions [16, 17]. Figure 8.6 (a) shows one transient with an oscillation frequency of ~50 kHz and a damping time of ~200 μs. Figure 8.6 (b) shows an individual pulse with a duration of 20 ns measured by a 12-GHz photodetector (EO Technics ET-3500) and a 20-GHz oscilloscope (Tektronix DSA 72004B). I believe that these pulses reached energies and peak powers high enough to damage the fibre-facet. Investigations of failed ends supported this view. However, with more careful polishing of the fibre end, I managed to largely suppress self-pulsation. Although occasional pulses were still observed, these did not damage the fibre ends even at maximum output power. Furthermore, uncontrolled pulsing is straightforward to avoid in an amplifier configuration.

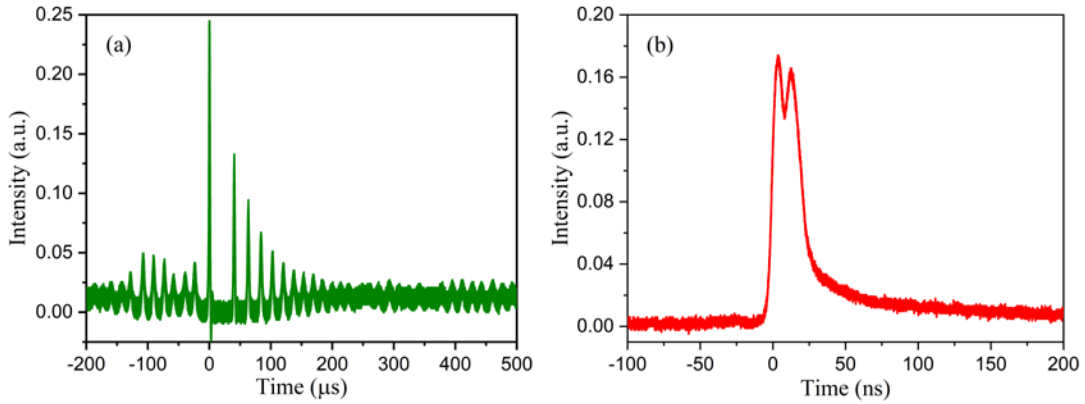


Figure 8.6: (a) Time-trace of potentially damaging self-pulsing and (b) sub-pulse.

The beam quality $M^2$-factor of the output signal was measured using a scanning-slit beam profiler (Thorlabs BP104-IR) and the result can be seen in Figure 8.7. At full output power, the $M^2$-factor became 10.45 and 10.53 in orthogonal directions, according to a hyperbolic fit to the measured beam width at the $1/e^2$ intensity-level. This agrees well with the beam quality

(~12.5) calculated from the refractive-index profile with an incoherent ray-approximation under the assumption of all core-guided modes being equally excited within the full NA. There was no significant power dependence of the beam quality. However, about 25% of the output power emerged from the inner cladding. This did not affect the $M^2$ calculation, since it was based on the beam width at the $1/e^2$-intensity-level.

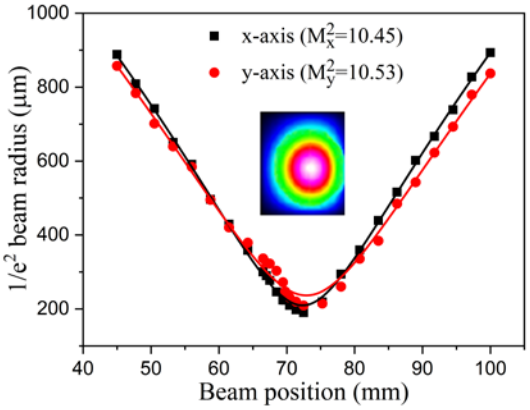


Figure 8.7: Beam radius of the output signal in orthogonal directions at maximum power measured with a scanning slit. Inset: output signal beam profile as reconstructed from two scans in orthogonal directions.

I next consider possible improvements in power and brightness, and the potential for CPA. State-of-the-art pump diodes can produce more than 140 W of power from 105 μm cores at 0.15 NA, which is bright enough for launching over 10 kW of pump power through each end of our EDF. However, our slope efficiency implies that ~60% of the pump power is converted into heat. Thermal loads averaging over 100 W/m are seldom used and may not be realistic, but 100 W/m still allows for 2 kW of output power.

Higher conversion efficiency is also possible and would mitigate thermal effects. I achieved 53% slope efficiency with respect to absorbed pump power when a 2-m-long piece of the fibre emitting at 1558 nm was core-pumped at 976 nm. The shortening of the fibre reduces the background loss, which increases the efficiency. In turn, at fixed output power, the higher efficiency reduces the thermal load by nearly half, relative to that with the 38.7% slope efficiency achieved in the 36-m cladding-pumped fibre.

The Er spectroscopy is marred with potential problems. When pumped at 0.98 μm, bottle-necking from the 0.98-μm pump level $^4I_{11/2}$, due to its lifetime of ~10 μs [18] in aluminosilicate, reduces the pump absorption at high pump rates. This is also a potential limitation. However, in our fibre, this is still negligible relative to our pumping rate of ~1250 $s^{-1}$ = (800 μs)$^{-1}$ on average at 656 W, and remains negligible also at 2 kW of output power.

A significant fraction of the signal power was in the cladding, which is not only undesirable but also unusual. There are several possible reasons for cladding-power. Our fibre has a small cladding/core area ratio, and this may lead to cladding-modes with significant overlap with the core and thus with high gain. To investigate this, I used the COMSOL Multiphysics software to analyse ~200 cladding modes (including polarisation degeneracy) whose mode effective index satisfy the condition of $n_{cladding} > n_{eff} > n_{coating}$ The simulation result is shown in Figure 8.8. Though the highest overlap ratio reaches 0.12, the fraction of such high-order cladding modes should be negligible. Furthermore, significant coupling amongst cladding modes is expected and indeed evidenced by the increase in absorption when the fibre was shaped to a figure-eight. Therefore, I discard the possibility of high gain for some cladding-modes.

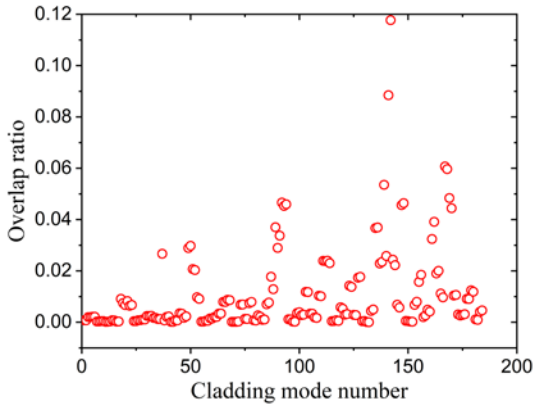


Figure 8.8: Overlaps between the ordered cladding modes and the core.

Another possible reason is that the HR-cavity mirror reflects a part of the light back into the cladding. To avoid this, the mirror should be placed one focal length from the lens in the equivalent of a so-called 4f configuration. At the same time, constraints imposed by our layout called for a mirror – lens distance of at least 150 mm. However, a lens that combines the large NA required for the pump launch with a focal length of at least 150 mm was not available. A multi-lens arrangement can then be used to improve the coupling back into the core, but was difficult because of layout constraints. Mirror butt-coupling is another possibility, but this was not attempted due to the high-power levels. A ray-based analysis under the assumption that all core-modes were equally excited was carried out. The result is depicted in Figure 8.9, which suggested that a ratio as large as ~33% (red dot on the blue line) would be coupled back into the cladding rather than the core due to the excessive mirror–lens distance in our configuration, even if perfectly aligned, although the higher gain for the core-guided light means that the ratio would improve in the output end of the fibre.

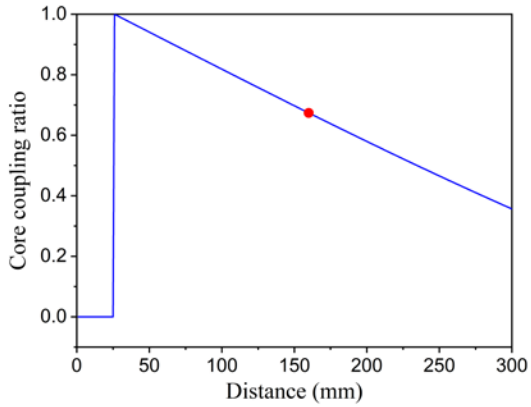


Figure 8.9: Ratio of reflected light coupled back into the core with respect to the excessive mirror – lens distance when a single lens of 30 mm focal length is used to collimate the output form the EDF. Red dot shows experimental distance.

To further investigate the effect of reflecting light into the cladding, I removed the external feedback mirror and instead had the fibre facets form the cavity. The core power ratio in the output beam *vs*. reflected back ratio into the core is simulated and is shown in Figure 8.10. Although the facets are not perfectly perpendicular to the fibre axis, this is expected to improve the core feedback ratio to over 90%. The cladding-power did decrease experimentally, but only from 25% to 15%, and part of this improvement can be attributed to the higher gain in this cavity, which increases the gain discrimination between core- and cladding-modes.

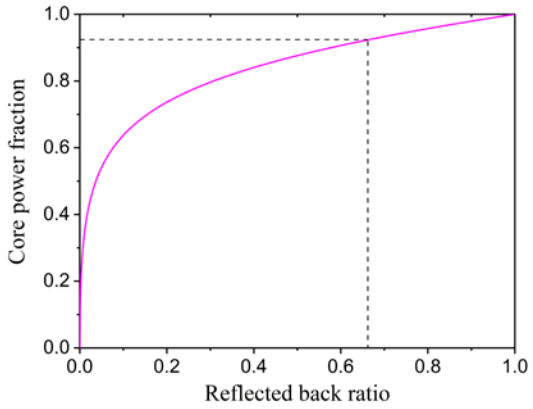


Figure 8.10: Power fraction in core with respect to the reflected back fraction.

Leakage of light propagating in the core into the cladding is another possibility. The large core supports many modes with similar propagation constants, which readily couple to each other. The coupling may well be enhanced by the fabrication process with the small preform-to-fibre diameter draw-down ratio, which is expected to result in relatively large longitudinally-varying inhomogeneities at high spatial frequencies. Note that the similarity between measured and calculated beam quality is an indication of significant mode-coupling. Coupling of power from the core to the cladding can thus be induced by micro-bending and other

inhomogeneities, even if the fibre is straight [19]. The large core, the low NA, and the small area ratio are likely to lead to a comparatively large fraction of core and cladding modes with similar propagation constants and significant overlap, which enhance such coupling. Bending the fibre can further increase the coupling, as a result of bend loss of high-order core-modes.

I therefore investigated to what extent light from a quasi-single-mode source at 1.05 μm launched into the core would couple into the cladding. I found that only ~40% of the power remained in the core after 36 m of the coiled fibre, compared to over 95% after a 30-cm straight length. Thus, I believe that there was significant leakage of power from the core to the cladding.

Looser coiling with less bending may improve the beam quality. Furthermore, the performance of passive large-core fibres suggests that leakage can be overcome even at 23-cm bend diameter, e.g., through more homogeneous fibre fabrication. On the other hand, a smaller core should also reduce coupling to cladding-modes as well as coupling between core-modes, and should then also allow for improved $M^2$-value or even single-mode operation as reported in [20]. There, the Er-doped fibre had a core diameter of 60 μm and an inner-cladding diameter of 240 μm, which allows for ~3.5 kW of pump power launched through each end. The peak pump rate becomes close to 100,000 $s^{-1}$ = $(10\ \mu s)^{-1}$, so bottle-necking would be significant. It is possible to decrease the lifetime of the pump level by phosphorus co-doping [21], but on the other hand, the bottle-necking helps to distribute the absorbed pump power and thus the thermal load along the fibre.

According to simulations (RP Fibre Power software) of an EDFL with a 60-μm diameter core, $50\times10^{25}$ ions/$m^2$ concentration-length product (similar to our fibre) and 20 dB inner-cladding small-signal pump absorption, the output power became 206 W and the pump absorption 17.5 dB for a pump power of 350 W, in the absence of excess loss mechanisms such as propagation loss, as shown in Figure 8.11 (a). Figure 8.11 (b) shows the 3.5 kW pump power case, the output power became 2.01 kW and the pump absorption decreased to 13.3 dB, due to an average pump-level population of 12%. Thus, even though the bottlenecking is significant with a 60-μm core, it was still possible to reach 2 kW of output power. At 2 kW, the thermal load would remain around 100 W/m, which may be manageable, although TMI may well preclude single-mode operation and would require investigation.

Normally, the ions dopant concentration in EDFs is an order of magnitude lower than that in YDFs mainly due to concentration quenching. Here we considered our EDF (A1028-L10552) and YDF (Clemson, DB01216) as representatives, though they have a similar concentration-length product, the EDF has a six-fold longer length. Combined with a larger quantum defect

(pumped at 0.98 μm), obviously, more nonlinearities are suffered when using such an EDF in CPA and CPSA systems. Compared to the YDF counterpart systems with same extracted energy, a more complex management of nonlinear phase distortions is necessary. Therefore, the potential of EDFs for CPA and CPSA largely depends on finding an effective solution to improving the erbium dopant concentration.

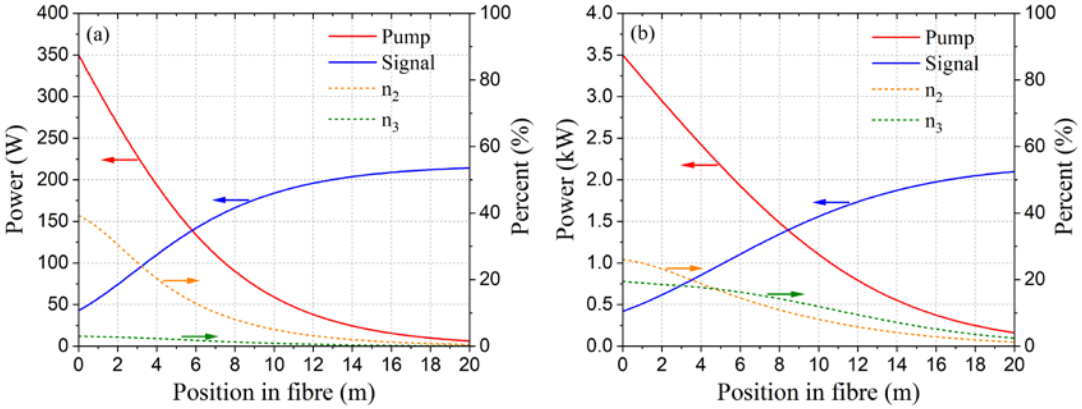


Figure 8.11: Fraction of excited ions ($n_2$: from metastable-level to ground-level) and ($n_3$: from pump-level to metastable-level), and power (pump and signal) *vs.* fibre position under an input pump power of (a) 350 W and (b) 3.5 kW.

## 8.3 High-efficiency Er-nanoparticle-doped Yb-free fibre laser

The presented experimental results and analysis show that a high erbium dopant concentration is key for successful power-scaling of Er-doped fibre sources, especially in the single-mode and short-pulse regime, where core size, refractive-index control, and nonlinearities are critical. Typically, fabrication of Er-doped optical fibres involves solution doping [22], which consists of the following steps. Firstly, salts of Er and Al (added to increase the solubility of Er ions and decrease the $Er^{3+}$ clustering) are dissolved in a solvent and then introduced into a previously deposited layer of porous silica "soot", typically inside a silica tube. Through further processing, the doped soot-layer is subsequently dried and consolidated to form the core material, and the tube is then collapsed into a preform with a solid core. However, the control of the atomic environment of the $Er^{3+}$ ions is relatively poor. This is due to the silica lattice of the fibre is unsuitable for achieving optimum $Er^{3+}$ properties. Even with the addition of Al, when the erbium concentration is increased, the distance to neighbouring $Er^{3+}$ ion decreases and the probability of ion-ion interaction increases. Furthermore, the $Er^{3+}$ ions would tend to cluster, which is particularly harmful due to unwanted excited state energy transfer processes, such as up-conversion and quenching. These processes would potentially generate a large amount of heat, shorten the fluorescence lifetime of the laser transition and greatly lower the laser efficiency [23]. To overcome the limitations defined by conventional

solution doping technique, a recent fabrication method called nanoparticle doping has been developed by Pastouret *et al*. [24].

### 8.3.1 Nanoparticle doping technique

Nanoparticle doping technique is possible to control the rare earth ions environment independently from the core composition. Specifically, the rare earth ions are encapsulated within the nanoparticle host and are thereby isolated from the influence of the silica lattice. Thus, it allows for higher dopant concentration by mitigating both Er up-conversion and quenching effects. A typical NP-fibre fabrication process through MCVD includes the steps of nanoparticle synthesis, solution-doping of a porous core layer, collapsing of preform tube, and drawing of fibre [24]. $Al_2O_3$/Er nanoparticles can be synthesized by the aqueous co-precipitation of Er and Al precursors in controlled temperature and pH conditions, followed by a ripening and a thermal processing. The up-conversion, quenching levels and amplification characteristics of these NP erbium doped fibres were also experimentally studied [25, 26]. Furthermore, Colin Baker *et al*. at NRL has experimentally investigated how to effective isolate the $Er^{3+}$ ions in the nanoparticle network [27]. With a proper selection of surfactant, synthesis temperature and pH, and Al/Er ratio, several Er-NP-doped samples have been fabricated and tested. As shown in Figure 8.12 (a), a smooth refractive index profile was achieved since the agglomeration is kept to a minimum. Figure 8.12 (b) shows the measurement results of fluorescence lifetime which can reach as long as 11.7 ms. In contrast to the conventional solution-doped fibre (~10.7 ms), an increased lifetime indicates that excited state energy transfer mechanisms have been reduced. High laser efficiency (~74% slope efficiency) can still be maintained at high dopant levels (a ratio of Al:Er precursor molarities of 50:1), as circled in Figure 8.12 (c). Meanwhile, a lower Al content reduces the core refractive index which is beneficial for high-power single-mode operation in a large mode area fibre while with a small core NA.

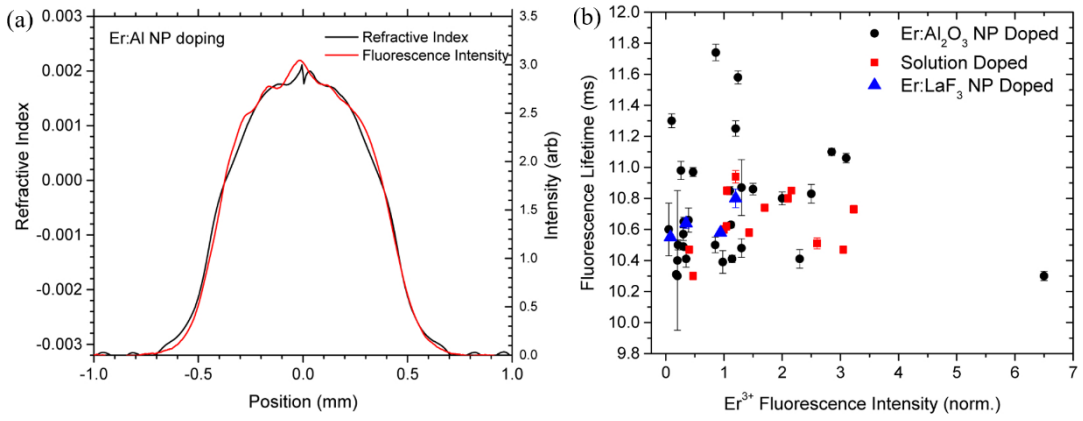

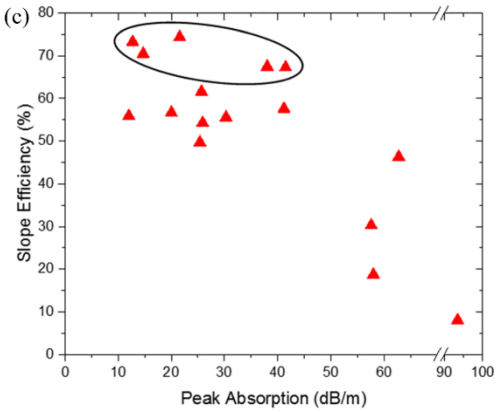


Figure 8.12: (a) Refractive index profile, (b) measured fluorescence lifetime, and (c) slope efficiency of Er-NP-doped fibre samples (reproduced from Ref. [27]).

### 8.3.2 Fibre characterization and experimental setup

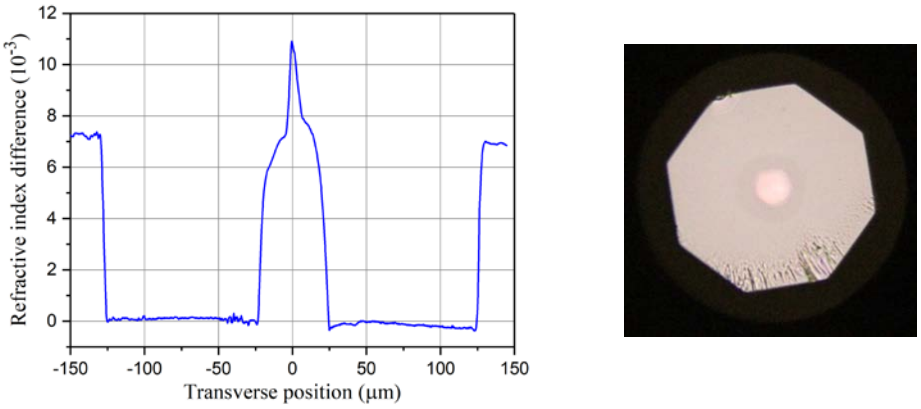


Figure 8.13: Refractive index profile of the fibre and the fibre facet image.

A fibre (NRL170525, provided by Colin Baker) was designed in which erbium ions were encaged in an aluminium NP host. The NP dispersion was synthesized by co-precipitation of salts of erbium and aluminium in the presence of a surfactant, followed by ripening, agglomerating and precipitating, and stable suspension. A 50:1 ratio of Al:Er precursor molarities was used in this fibre sample. The NP dispersion was then doped into the preform core in a manner similar to that for solution doping. Figure 8.13 shows the refractive index profile of its core, which has a spike located at the fibre core axis region. This uneven ion distribution can be confirmed from the 2D measured data, which might be related to imperfect control during the fabrication process. The fibre had an octagonal inner cladding with 264-μm corner-to-corner diameter. A low-refractive-index polymer coating provided a nominal inner-cladding NA of 0.48. The $Er^{3+}$-NP doped aluminosilicate core had a diameter of 45 μm and an NA of 0.18 (V=15.7 at the signal wavelength of 1605 nm). The fibre background loss at 1600 nm was about 0.1 dB/m. The small-signal absorption in the inner cladding was ~1.1 dB/m at the 979-nm peak, from which I estimate the $Er^{3+}$ concentration to $4\times10^{25}$ ions/$m^3$.

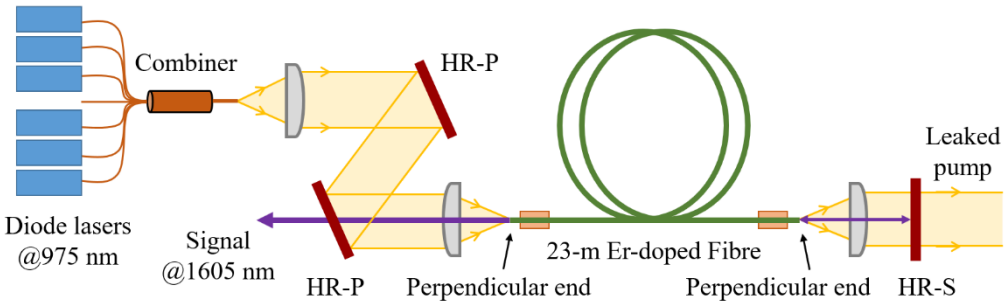


Figure 8.14: EDFL schematic. HR-P: high-reflectivity for pump, HR-S: high-reflectivity for signal.

The experimental laser configuration is shown in Figure 8.14. Six multimode diode lasers with wavelength centred at 975 nm were combined by a 7×1 fibre combiner, which provides 420 W of maximum pump power from a 125-μm diameter, 0.46-NA pigtail. The pump beam was free-space coupled into the Er-doped fibre with lenses, with a launch efficiency of ~85%. The 23-m long fibre yielded an operating pump absorption of 7 dB. The reduction from the small-signal absorption is at least in part caused by partial excitation of the Er-ions. A higher absorption would be preferable and I estimate it would improve to 8.2 dB by pumping at the 979-nm peak. Both ends were cleaved perpendicularly to the fibre axis, with the cleave in the pump launch end acting as output coupler with 4% Fresnel reflection. At the other end of the fibre laser cavity, a lens-coupled dichroic mirror provided high-reflectivity (>97%) feedback for the signal, while unabsorbed pump was transmitted. The laser output beam was separated from the pump beam by another dichroic mirror with characteristics opposite to those of the feedback mirror. Both fibre ends were held in temperature-controlled metallic V-grooves to prevent thermal damage to the fibre coating. For further heat-sinking, the fibre was coiled on a 12.5-cm diameter metal cylinder and air-cooled by fans.

### 8.3.3 Experimental results and discussions

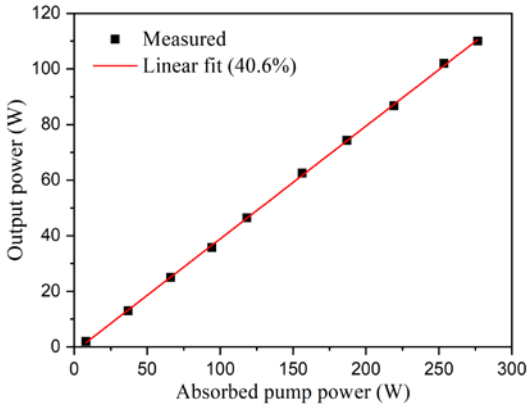


Figure 8.15: Laser output power *vs.* absorbed pump power.

The laser output power as a function of the absorbed pump power is shown in Figure 8.15. The laser threshold was 4.3 W and the maximum output power was 110 W, limited by available pump power. The laser output power increased linearly with the pump power and showed no evidence of roll-off even at the highest power. The slope efficiency was 40.6% with respect to absorbed pump power. Given the ~20% (68 W of leaked pump power) pump leakage, this dropped to 32.3% with respect to launched pump power. I expect that double-passing the pump would significantly improve this, as well as the output power.

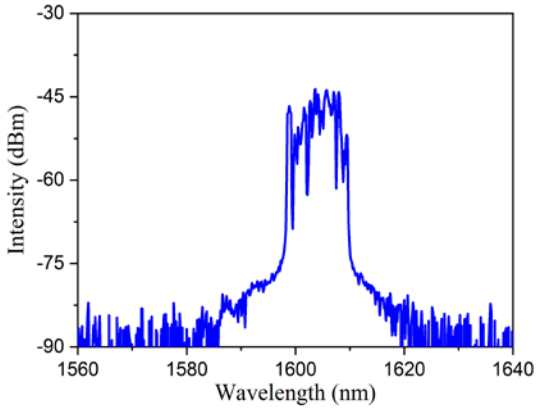


Figure 8.16: Laser output spectrum at 110 W output, Resolution: 0.5 nm.

The output spectrum measured at the maximum output power of the laser is plotted in Figure 8.16. The spectrum was centred at 1605 nm and had a 3-dB linewidth of 6 nm. The fraction of ASE was less than 0.1%. The average heat dissipation at full power was only ~7 W/m, and no thermal degradation of the coating was observed. Pulsing is also a potential failure mechanism. The temporal power characteristic was monitored with a 12-GHz photodetector (EO Technics ET-3500) and a 20-GHz oscilloscope (Tektronix DSA 72004B), as shown in Figure 8.17 at full power. The pulse duration of these random pulses was estimated to around 50 ns. The peak amplitude was ~8 times the average amplitude, from which the maximum pulse energy was estimated to 40 μJ. This is unlikely to damage the laser, and no damage was observed.

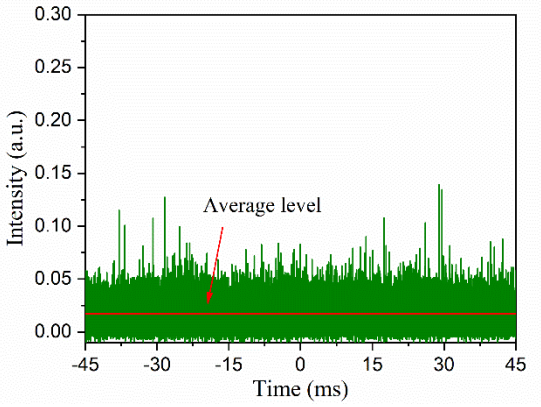

Figure 8.17: Temporal power characteristic.

The beam quality of the output signal was measured using a Photon Inc. Nanoscan scanning slit beam profiler. Figure 8.18 shows that, at full power, the $M^2$-factor was 6.8 and 7.1 in orthogonal directions, according to a hyperbolic fit to the measured beam width. This value is compatible with equal excitation of all modes of the core. I did not attempt to improve the beam quality, e.g., by using a mode-selective aperture or bendloss filtering. However, mode-coupling can be relatively weak at 1605 nm in a 45-μm core, so significant improvements may well be possible.

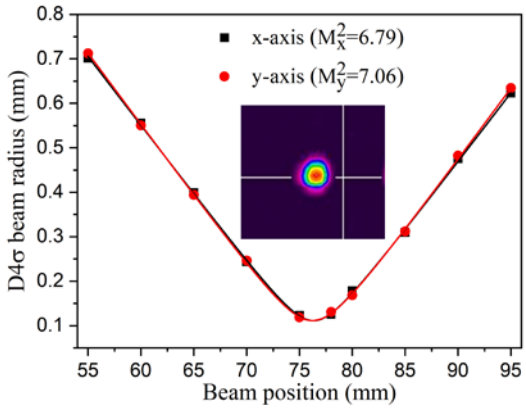


Figure 8.18: Measured beam radius of the output signal in the horizontal and vertical beam axes at maximum output power.

## 8.4 Conclusion

In conclusion, I have demonstrated a large-core Er-doped Yb-free fibre laser cladding-pumped by 0.98-μm diode lasers to overcome the current average power limitations in EDFLs. An output power of 656 W was achieved, though with a $M^2$-value of 10.5. The analysis suggests that Yb-free EDFLs with over 1 kW of power and high beam quality are possible with judicious fibre design and state-of-the-art pump diodes. Due to the low pump absorption, the high nonlinearity imposed by the long interaction length would reduce the efficient energy extraction and complex the systems when applying in CPA and CPSA. To overcome it, a fibre with an Er-concentration as high as $4\times10^{25}$ ions/$m^3$ without concentration quenching was fabricated through the high-concentration nanoparticle doping technique. Experimentally, a high-efficient (40.6%), high-power (110 W) Yb-free Er-nanoparticle high-concentration fibre laser directly pumped by diode lasers at 975 nm was demonstrated.

## References


[1]. K. Moutzouris, F. Sotier, F. Adler, and A. Leitenstorfer, “Highly efficient second, third and fourth harmonic generation from a two-branch femtosecond erbium fiber source”, Opt. Express **14**, 1905 (2006).

[2]. D. J. Richardson, J. Nilsson, and W. A. Clarkson, “High power fiber lasers: current status and future perspectives [Invited]”, J. Opt. Soc. Am. B **27**, B63 (2010).

[3]. A. Berk, L. S. Bernstein, and D. C. Robertson, “MODTRAN: A moderate resolution model for LOWTRAN 7”, Final report, GL-TR-0122, AFGL, Hanscomb AFB, MA, 1989, pp. 42.

[4]. E. Delevaque, T. Georges, M. Monerie, P. Lamouler, and J.-F. Bayon, “Modeling of Pair-Induced Quenching in erbium-doped silicate fibers”, IEEE Photon. Technol. Lett. **5**, 73 (1993).

[5]. Y. Jeong, S. Yoo, C. A. Codemard, J. Nilsson, J. K. Sahu, D. N. Payne, R. Horley, P. W. Turner, L. Hickey, A. Harker, M. Lovelady, and A. Piper, “Erbium:Ytterbium Codoped Large-Core Fiber Laser With 297-W Continuous-Wave Output Power”, IEEE J. Sel. Top. Quantum Electron. **13**, 573 (2007).

[6]. G. G. Vienne, J. E. Caplen, L. Dong, J. D. Minelly, J. Nilsson, and D. N. Payne, “Fabrication and Characterization of $Yb^{3+}$:$Er^{3+}$ Phosphosilicate Fibers for Lasers”, J. Lightwave Technol. **16**, 1990 (1998).

[7]. M. A. Jebali, J. N. Maran, and S. LaRochelle, “264 W output power at 1585 nm in Er-Yb codoped fiber laser using in-band pumping”, Opt. Lett. **39**, 3974 (2014).

[8]. J. D. Minelly, R. I. Laming, J. E. Townsend, W. L. Barnes, E. R. Taylor, K. P. Jedrzejewski, and D. N. Payne, “High gain fibre power amplifier tandem-pumped by a 3 W multi-stripe diode”, in Optical Fiber Communications Conference (Optical Society of America, 1992), pp. 32.

[9]. V. R. Supradeepa, J. W. Nicholson, and K. Feder, “Continuous wave Erbium-doped fiber laser with output power of >100 W at 1550 nm in-band core-pumped by a 1480 nm Raman fiber laser”, in Conference on Lasers and Electro-Optics (Optical Society of America, 2012), paper CM2N.8.

[10]. J. Zhang, V. Fromzel, and M. Dubinskii, “Resonantly cladding-pumped Yb-free Er-doped LMA fiber laser with record high power and efficiency”, Opt. Express **19**, 5574 (2011).

[11]. M. A. Jebali, J. Maran, S. LaRochelle, S. Chatigny, M. Lapointe, and E. Gagnon, “A 103 W High Efficiency In-Band Cladding-Pumped 1593 nm All-Fiber Erbium-Doped Fiber Laser”, in Conference on Lasers and Electro-Optics (Optical Society of America, 2012), paper JTh1I.

[12]. J. D. Minelly, Z. J. Chen, R. I. Laming, and J. E. Caplen, “Efficient Cladding Pumping of an Er3+ Fibre”, in 21st European Conference on Optical Communication 1995, paper 917.

[13]. L. V. Kotov, M. E. Likhachev, M. M. Bubnov, O. I. Medvedkov, M. V. Yashkov, A. N.

Guryanov, S. Fevrier, J. L'hermite, and E. Cormier, “Yb-free Er-doped all-fiber amplifier cladding-pumped at 976 nm with output power in excess of 100 W”, in Proceedings of SPIE 8961, Fiber Lasers XI: Technology, Systems, and Applications 2014, paper 89610X.

[14]. B. Steinhausser, A. Brignon, E. Lallier, J. P. Huignard, and P. Georges, “High energy, single-mode, narrow-linewidth fiber laser source using stimulated Brillouin scattering beam cleanup”, Opt. Express **15**, 6464 (2007).

[15]. H. Lin, Y. Feng, P. Barus, J. K. Sahu, and J. Nilsson, “405 W Erbium-Doped Large-Core Fiber Laser”, in Advanced Solid State Lasers (Optical Society of America, 2017), paper ATh4A.2.

[16]. P. Le Boudec, M. Le Flohic, P. L. Francois, F. Sanchez, and G. Stephan, “Influence of ion pairs on the dynamical behavior of Er3+-doped fibre lasers”, Opt. Quantum Electron. **25**, 501 (1993).

[17]. F. Sanchez, P. Le Boudec, P. L. Francois, and G. Stephan, “Effects of ion pairs on the dynamics of erbium-doped fiber lasers”, Phys. Rev. A **48**, 2220 (1993).

[18]. A. J. W. Ellison, J. E. Dickinson, D. E. Goforth, D. L. Harris, J. T. Kohli, J. D. Minelly, B. N. Samson, J. K. Trenteman, M. J. Yadlowsky, “Hybrid erbium silicate conventional-band fiber amplifier with ultra-low gain ripple”, in Proceeding of Opt. Amplifiers and Their Applications 1999, paper 51.

[19]. C. K. Nielsen, E. Riis, A. Petersson, and J. Broeng, “Investigations of the coupling between core modes and cladding modes in a double-clad Yb-doped photonic crystal fiber”, in Proceeding of SPIE 5335, Fiber Lasers: Technology, Systems, and Applications 2004, paper 180.

[20]. M. E. Fermann, “Single-mode excitation of multimode fibers with ultrashort pulses”, Opt. Lett. **23**, 52 (1998).

[21]. V. P. Gapontsev, S. M. Matisin, A. A. Isineev, and V. B. Kravchenko, “Erbium glass lasers and their applications”, Opt. Laser Technol. **14**, 189 (1982).

[22]. J. E. Townsend, S. B. Poole, and D. N. Payne, “Solution-Doping Technique for Fabrication of Rare-Earth-Doped Optical Fibers”, Electron. Lett. **23**, 329 (1987).

[23]. M. J. F. Digonnet (ed.), “Rare-earth-doped fiber lasers and amplifiers, revised and expanded”, CRC press, 2001.

[24]. A. Pastouret, C. Gonnet, C. Collet, O. Cavani, E. Burov, C. Chaneac, A. Carton, and J. P. Jolivet, “Nanoparticle doping process for improved fibre amplifiers and lasers”, in Proceeding of SPIE 7195, Fiber Lasers VI: Technology, Systems, and Applications 2009, paper 71951X.

[25]. D. Boivin, T. Föhn, E. Burov, A. Pastouret, C. Gonnet, O. Cavani, C. Collet, and S. Lempereur, “Quenching investigation on new erbium doped fibers using MCVD nanoparticle doping process”, in Proceeding of SPIE 7580, Fiber Lasers VII: Technology, Systems, and Applications 2010, paper 75802B.

[26]. D. Boivin, A. Pastouret, E. Burov, C. Gonnet, O. Cavani, S. Lempereur, and P. Sillard, “Performance characterization of new erbium-doped fibers using MCVD nanoparticle doping process”, in Proceeding of SPIE 7914, Fiber Lasers VIII: Technology, Systems, and Applications 2011, paper 791423.

[27]. C. C. Baker, E. J. Friebele, A. A. Burdett, D. L. Rhonehouse, J. Fontana, W. Kim, S. R. Bowman, L. B. Shaw, J. Sanghera, J. Zhang, R. Pattnaik, M. Dubinskii, J. Ballato, C. Kucera, A. Vargas, A. Hemming, N. Simakov, and J. Haub, “Nanoparticle doping for high power fiber lasers at eye-safer wavelengths”, Opt. Express **25**, 13903 (2017).

# Chapter 9
# Conclusions and future work

In this chapter, I will summary the work presented throughout this thesis and suggest possible improvements and future research directions.

## 9.1 Conclusions

The work presented in this thesis can be summaried as: develop pulsed fibre systems and new methods of phase characterization and optimization for coherent combination (in Chapter 3-6) as well as fibres (in Chapter 3, 6, 7 and 8).

In Chapter 3, I demonstrated a high-energy narrow-linewidth linearly-polarised pulse-burst Yb-doped fibre amplifier system. 100-kHz bursts of 50 1-ns pulses with 10-ns separation were produced via an EOM and an AOM from a single-frequency CW DFB diode laser. The bursts were pre-amplified by four YDFAs, which were co-pumped and fully fibreised with PM fibres. Then the bursts were amplified in a counter-pumped low-NA low-birefringence LMA Yb-doped fibre amplifier. Finally, a single-mode laser at 1064 nm with a 250-W average output power, a 2.5-mJ burst energy and a PER of 19 dB was achieved. This laser system is developed for the phase distortions investigations in Chapter 4 and 5.

In Chapter 4, I have demonstrated a single-shot high-speed interferometric phase measurement of spectrally narrow pulses. A maximum phase distortion of 21.2 rad was characterized in a burst of 35 1-ns Gaussian-like pulses at 1063 nm from a cascaded Yb-doped fibre amplifiers. In the highly nonlinear and saturated regime, the differences in phase profile between pulses within a burst were large enough to degrade the combining efficiency when temporally recombining pulses into a single pulse. Thus, the intra-pulse phase profile needs to be corrected. In addition, 6% amplitude fluctuation and 0.6 rad phase fluctuation between bursts were also diagnosed. These fluctuations cannot be corrected, but are not so large that they preclude efficient pulse stacking. Last and least, according to the measurement with different diode laser drivers, it is concluded that there are no additional amplitude noises contributed by the diode laser drivers.

In Chapter 5, I firstly theoretically studied the influence of amplitude difference, *B*-integral difference and input amplitude fluctuation between pulse-burst on the coherent combining efficiency. Based on the calculation results, an optimized phase profile was achieved by an inter-pulse amplitude compensation and intra-pulse instantaneous-phase equalization via fast

EOMs. Finally, a theoretical 90% coherent pulse stacking efficiency was demonstrated in a highly-nonlinear (>10 rad *B*-integral) and energy-saturated (1.15 mJ) narrow-linewidth linearly-polarised pulse-burst fibre laser system.

In Chapter 6, I have experimentally demonstrated passive coherent beam combination in an ultrafast parabolic-pulse twin-core Yb-doped fibre amplifier in the highly nonlinear regime. An 88.5% coherent combining efficiency was achieved though the amplifier has a *B*-integral of 29 rad. This successful achievement relies on a self-designed and in-house fabricated single-mode PM twin-core double-clad Yb-doped fibre and a Dammann grating which well matches the beam into two cores. The core proximity diminished the SPM-induce phase difference between two cores and finally guaranteed a high combining efficiency. The integrated multicore dopant fibre would benefit the coherent beam combination community with advantages on system compactness and efficiency.

Another separate work I have done is the investigation on a bendable non-circular core LMA Yb-doped fibre which is designed to mitigate bending distortions and mode degeneracy, described in Chapter 7. Firstly, the influence of bending on the FM effective area with different core ARs was theoretically studied. Parameters of core with 41 μm short axis and an AR of 4 was determined for the fabrication, which combines a conventional MCVD process with a confined doping and post-processing techniques. I demonstrated that the fabricated fibre exhibited efficient laser performance with 67% of slope efficiency and nearly 200 W output power, with beam quality factor of 1.3 and 3.1 respectively along short axis and long axis. The HOM excitation was attributed at least in part to the offset bending angle, which can be avoided with an optimised control in the fabrication process.

In Chapter 8, I investigated and demonstrated the single-fibre power scaling of erbium fibre lasers combined with fibre designs and fabrications. In the first work, I presented an Er-doped Yb-free fibre laser cladding-pumped by 0.98-μm diode lasers, with a 656-W record-breaking output power at 1601 nm with a 35.6% laser slope efficiency. For this, a tailored Er-doped fibre with 0.7-mm inner cladding was designed and fabricated to suit our pump source, a modest Er-concentration to avoid quenching, a large 146-μm-diameter core to improve the pump absorption, and a 36-m length to absorb the pump and distribute the thermal load. In another work, benefiting from a high-concentration NP doping technique, an Er-doped Yb-free fibre with as high as $4\times10^{25}$ ions/$m^3$ Er-concentration was fabricated. I experimentally demonstrated a 0.98-μm cladding-pumped Er-doped fibre laser with a ~41% laser slope efficiency, which means that the quenching effect is well suppressed in this fibre.

## 9.2 Future work

As mentioned before, it is of great interest to apply the single-shot interferometric temporal-phase measurement technique into CPA and chirped DPA systems for femtosecond pulses. Besides, an optimized technique for improving the measurable dynamic range of phase distortions can also be considered. Further, in terms of the amplitude and phase controls, an automatic measurement and phase locking feedback system can be built for practical application consideration.

In the current systems, the inter- and intra-phase distortions are mainly caused by SPM and gain-saturation. However, if a short length and highly-doped fibre is used, for example, thermal effects such as photodarkening heating may cause phase distortions. Thus, a theoretical study on the thermal effects (e.g. QD heating) and K-K effect induced phase distortions in fibre amplifiers can be performed. The effects of these phase distortions on the coherent combining efficiency can be numerically analysed. Through these theoretical and experimental studies, I hope that a constructive feedback can be acquired for the fibre and amplifier designs. Conversely, the fibre and amplifiers with optimized or minimized phase and thermal effects will be beneficial for ultrafast pulses and for coherent beam combination of ultrafast pulses. Besides, it would be of great practical value to design a compact and easily-realized coherent beam combination scheme for these pulse-bursts fibre laser systems.

Last but not least, more efforts can be dedicated to the fibre (including Yb and Er) design and fabrication. I believe, for example, the power potential exploitation of Er-doped fibre laser would attract attentions in new regimes, such as the pumping of Tm CPA system with low thermal load and TMI investigations.

# Appendix A List of publications

## A.1 Journal publications

1. **H. Lin**, Y. Feng, J. H. V. Price, and J. Nilsson, "Single-shot phase and amplitude fluctuations of narrow-line pulse bursts in divided-pulse amplifier", IEEE Photonics Technology Letter, **31**(20), 1662-1665, 2019.
2. Y. Feng, P. G. R. Hernández, S. Zhu, J. Wang, Y. Feng, **H. Lin**, O. Nilsson, J. Sun, and J. Nilsson, "Pump absorption, laser amplification, and effective length in double-clad ytterbium-doped fibers with small area ratio", Optics Express, **27**(19), 26821-26841 (2019).
3. **H. Lin**, Y. Feng, Y. Feng, P. Barua, J. Sahu, and J. Nilsson, "656W Er-doped Yb-free large-core fiber laser", Optics Letters, **43**(13), 3080-3083 (2018).
4. J. Ji, **H. Lin**, R. Sidharthan, D. Ho, Y. Zhou, J. Nilsson, and S. Yoo, "Bendable large-mode-area fiber with non-circular cores", Applied Optics, **57**(22), 6388-6395 (2018).

## A.2 Conference publications

1. **H. Lin**, Y. Feng, J. H. V. Price, T. W. Hawkins, L. Dong, and J. Nilsson, "Active Instantaneous-Phase Equalization and Amplitude Control in Pulse-Bursts in a Narrow-Linewidth Divided-Pulse Yb-Doped Fiber Amplification System", in OSA Laser Congress 2019: Advanced Solid State Lasers Conference, Vienna, Austria, paper ATh2A.2.
2. **H. Lin**, Y. Feng, T. W. Hawkins, Z. Huang, Y. Feng, J. H. V. Price, L. Dong, and J. Nilsson, "2.5 mJ narrow-linewidth, linearly-polarised pulse-burst high-power Yb-doped fiber amplifier system", in 2019 European Conference on Lasers and Electro-Optics and European Quantum Electronics Conference, Munich, Germany, paper CJ-P.20.
3. Y. Feng, C. A. Codemard, P. Barua, **H. Lin**, S. Zhu, Y. Feng, S. Pidishety, S. Hong, J. K. Sahu, and J. Nilsson, "Time Response Characteristics of Photodarkening-Induced Loss in Yb-Doped Fiber Amplifier", in 2019 European Conference on Lasers and Electro-Optics and European Quantum Electronics Conference, Munich, Germany, paper CJ-2.2.

4. Ł. Dziechciarczyk, Z. Huang, G. Demetriou, D. Cheng, S. Pidishety, Y. Feng, Y. Feng, G. Wang, **H. Lin**, S. Zhu, D. Lin, T. W Hawkins, L. Dong, A. Kemp, J. Nilsson, and V. Savitski, "9 W average power, 150 kHz repetition rate diamond Raman laser at 1519 nm, pumped by a Yb fibre amplifier", in 2019 European Conference on Lasers and Electro-Optics and European Quantum Electronics Conference, Munich, Germany, paper CA-11.2.

5. J. Ji, **H. Lin**, R. Sidharthan, D. Ho, Y. Zhou, N. Xia, J. Nilsson, and S. Yoo, "Large-Mode-Area Fiber with Non-Circular Cores", in 2018 23rd Opto-Electronics and Communications Conference, Jeju Island, South Korea, paper SC3.1020.

6. **H. Lin**, C. Baker, Z. Huang, S. Pidishety, Y. Feng, E. J. Friebele, A. Burdett, D. Rhonehouse, L. B. Shaw, J. Sanghera, and J. Nilsson, "110 W High-Efficiency Er-Nanoparticle-Doped Fiber Laser", in *2018* Conference on Lasers and Electro-Optics, San Jose, United States, paper SW4K.5.

7. Y. Feng, **H. Lin**, and J. Nilsson, "Single-shot phase measurement and fluctuation analysis of Yb-doped fiber amplifier for nanosecond pulses", in 2018 Conference on Lasers and Electro-Optics, San Jose, United States, paper SM2K.7.

8. Y. Feng, S. Zhu, S. Hong, **H. Lin**, P. Barua, J. Sahu, and J. Nilsson, "Spatially Gain-Tailored Fiber Raman Laser Cladding-Pumped by Multimode Disk Laser at 1030 nm", in 2018 Conference on Lasers and Electro-Optics, San Jose, United States, paper JTh2A.109.

9. **H. Lin**, Y. Feng, P. Barua, J. Sahu, and J. Nilsson, "405 W Erbium-doped large-core fiber laser", in OSA Laser Congress 2017: Advanced Solid State Lasers Conference, Nagoya, Japan, paper ATh4A.2.

## A.3 Manuscripts under preparation

1. **H. Lin**, Y. Feng, P. Barua, W. M. Kunkel, J. H. V. Price, J. Sahu, J. R. Leger, and J. Nilsson, "Passive coherent beam combination in an ultrafast pulse twin-core fiber amplifier in the highly nonlinear regime".
2. Y. Feng, **H. Lin**, J. H. V. Price, and J. Nilsson, "Inter pulse amplitude and intra pulse phase control of bursts of narrow-line pulses in a divided-pulse amplification system".